FACULTY OF SCIENCE
UNIVERSITY OF COPENHAGEN

Master's thesis in Physics

A novel laser-based technique for continuous measurements of methane concentrations from deep ice cores

Christopher Stowasser
Centre for Ice and Climate
Niels Bohr Institute
University of Copenhagen

Supervisor:
Prof. Dr. Thomas Blunier

April 2010

Master's Thesis

Title:	A novel laser-based technique for continuous measurements of methane concentrations from deep ice cores
ECTS-points:	60
Supervisor:	Thomas Blunier
Name of department:	Centre for Ice and Climate Niels Bohr Institute University of Copenhagen
Author:	Christopher Stowasser
Date:	1st of April, 2010

Abstract

The analysis of stable water isotopes, gas bubbles and impurities trapped in ice provides knowledge of earth's past climate. Deep ice cores from Greenland act as climate archives for more than the last 123,000 years covering the Holocene, the last glacial period and parts of the previous interglacial period called the Eemian.

This thesis presents preparation and first field tests of a novel laser-based method for measuring methane concentrations from deep ice cores with high precision and high temporal resolution. Measurements are carried out by a near-infrared cavity ring-down spectrometer which is connected to the field-deployable Continuous Flow Analysis system from the University of Bern. Here, air bubbles are continuously extracted from the melted ice core samples and are forwarded into the spectrometer for methane concentration measurements.

During the 2009 field season of the North Greenland Eemian Ice Drilling project (NEEM) methane concentrations were measured along 12.1 meters of ice core from the early Holocene period. These experiments showed that the method is suited for field measurements and yields an unprecedented temporal resolution. However, the precision of the method is not yet comparable to conventional discrete methods for measuring methane concentrations from ice cores and needs to be improved. Experiences from this first test season helped to locate the problem of precision and improvements are presented which will be implemented before the 2010 field season.

Preface

In this preface I like to provide an overview of the structure of this Master's thesis. The first part follows a traditional structure:

- **Chapter 1:** A brief introduction which includes the motivation for developing a novel method for measuring methane concentrations from ice cores and a comparison to established methods.
- **Chapter 2:** An overview of ice sheets, drilling sites and the most important climatic information that can be retrieved from an ice core. This chapter is recommended for readers that are unfamiliar with the field of ice core research.
- **Chapter 3:** The theory of absorption spectroscopy where it is explained how methane concentrations can be measured with the help of a near-infrared cavity ring-down spectrometer.
- **Chapter 4:** Specifications of the three instruments which are utilized during the experiments described in this thesis. This includes the near-infrared cavity ring-down spectrometer for measurements of methane concentration, an oxygen sensor and a thermal conductivity detector, both for measurements of total air content. For the two latter the theory of measurement is briefly described in this chapter.

The second part of this thesis is structured chronologically and follows the history of development of the system.

- **Chapter 5:** Preparative tests for the 2009 NEEM field season where the near-infrared cavity ring-down spectrometer is tested in combination with each of the two instruments for measurements of total air content.
- **Chapter 6:** Experiments and results from the 2009 NEEM field season. This includes the analysis and discussion of the measured methane concentrations from the NEEM ice core.
- **Chapter 7:** Conclusions and outlook, where the most important results of this thesis are summarized and future prospects for improvement of the method are introduced.

Since both the preparative tests and the field experiments are complex, it was decided to treat them almost independently. Therefore, Chapter 5 and Chapter 6 each tell a complete story of the corresponding experiment including an introduction, a method part, results and discussion.

Copenhagen, *Christopher Stowasser*
April 2010

Acknowledgments

I would like to thank my supervisor Thomas Blunier for his constant support and interesting discussions throughout my Master studies as well as for introducing me to the field of ice core research. The manufacturer Picarro, especially their applications engineer Aaron van Pelt, is thanked for outstanding and patient customer support.
The members of the gas group and of the isotope group from the Centre for Ice and Climate are thanked for fruitful discussions and valuable help inside and outside of the laboratory.
I thank the teams of the Continuous Flow Analysis in Bern and in Copenhagen as well as the NEEM drilling and ice core processing teams for providing excellent ice core samples as the foundation of our measurements.
Also, I thank Dorte Dahl-Jensen and the Centre for Ice and Climate for providing such an inspiring environment for Master students and giving me the opportunity to experience ice core field work.
Furthermore, I (and supposably the readers of this thesis) are grateful for constructive proof reading by David Balslev-Clausen, Christo Buizert, Susanne Lilja Buchardt, Vasileios Gkinis, Trevor James Popp and Sebastian Bjerregaard Simonsen.
Last but not least, I thank Sanne and the members of my family Anja, Kathi, Waltraud, Elisabeth and Horst for their love, trust and support. Without you my studies in Denmark would not have been possible.

Copenhagen, *Christopher Stowasser*
April 2010

Contents

Chapter 1

Introduction

Atmospheric methane (hereafter CH_4) is the second most important anthropogenic greenhouse gas as well as a sensitive indicator of climate change and millennial-scale temperature variability [1]. High resolution records of past atmospheric concentrations of CH_4 can be measured from deep ice cores since bubbles of atmospheric air are trapped in the ice [2]. Measurements from ice cores from Antarctica show that atmospheric CH_4 concentrations varied between ca. 350 and 800 parts per billion by volume (hereafter ppbv) over the past 800,000 years [3].

During the last 250 years atmospheric CH_4 concentrations have risen steadily as a consequence of human activities [4]. Present atmospheric concentrations of CH_4 are above 1750 ppbv.

This thesis presents the development and first field tests of a novel method for continuous measurements of CH_4 concentrations from ice cores with the use of a near-infrared cavity ring-down spectrometer. The focus of this work is on the development of a system that can be deployed on the ice sheet where it continuously measures CH_4 concentrations from ice cores which are melted in a field-deployable Continuous Flow Analysis system for chemical analysis (hereafter CFA).

The following two sections provide a brief overview of existing techniques for measuring CH_4 concentrations from ice cores. Then, in Sections 1.3 and 1.4 we outline our motivation for developing a novel method and compare it to the existing techniques. An overview of the different methods for measuring CH_4 concentrations from ice cores is shown in Table 1.1.

1.1 Discrete measurements of CH_4 concentration

Established methods for measuring atmospheric CH_4 concentrations from ice cores are based on gas chromatography. Here, CH_4 is separated from other gas species of the sample stream before its concentration is measured e.g. by a Thermal Conductivity Detector or a Flame Ionization Detector [5]. Separation is based on the different retention times of gas species in the column of the gas chromatograph (hereafter GC). These retention times depend on the affinity of the gas species for the coating material of the column [6]. Before

gases can be separated in the GC they need to be extracted from the ice core. Two principles of gas extraction have proven their value in numerous experiments:

- During a **wet extraction** the ice sample is melted under vacuum and then slowly refrozen from the bottom. This melt-refreezing method ensures that most of the dissolved air in the water is pushed out of the ice sample. The released air is flushed into a GC. The efficiency of this extraction method is about 99 % [7]. The wet extraction technique was used e.g. to obtain a CH_4 record from the GRIP ice core at Laboratoire de Glaciologie et Gèophysique de l'Environment in Grenoble with a precision of $\pm$37 ppbv (2σ) and sample sizes of approximately 40–50 g [8].

- The **dry extraction** method, on the other hand, extracts the gases with the use of a crusher or grater inside a vacuum-sealed stainless steel container where the ice sample is crushed or grated into powder. The released air is flushed into a GC. The crusher-based dry extraction technique was used e.g. at the University of Bern for measuring CH_4 concentrations from the GRIP ice core with a precision of $\pm$ 20 ppbv (2σ) and a sample size of 12–20 g [9].

Both laboratories later used an improved wet extraction technique to obtain high-resolution atmospheric CH_4 records from two Antarctic ice cores (D47 and Byrd) and to improve the GRIP record [10]. With the new extraction line the time of measurement decreases because it can handle seven glass containers (instead of one for the former extraction line) and has a smaller volume. The precision improved to $\pm$ 20 ppbv (2σ). The same extraction line was used for measurements on the EPICA Dome C ice core from Antarctica covering the last 800,000 years and yielded a CH_4 record with a precision of $\pm$ 10–15 ppbv [11].

Both extraction techniques allow only for discrete measurements where an individual piece of ice core is melted or crushed in order to extract the gases. The concentration of the gas in question is measured once from the extracted gases. These procedures offer a very high precision but require large sample sizes, which sets a limit to the temporal resolution (in average discrete measurements are conducted once every meter along the ice core). Furthermore, they require a lot of man power since the extraction process is not fully automated.

This brief summary does not include all discrete extraction methods and not all laboratories that use theses techniques have been named. Detailed summaries of discrete extraction methods can be found, e.g., in work by Sowers et al. [12] and a review by Iowe et al. [13].

1.2 Semi-continuous measurements of CH_4 concentration

A new method for high-resolution CH_4 concentration measurements was recently developed at the University of Bern [14]. This field-deployable method is connected to a CFA system where ice cores are continuously melted at a rate of ca. 3.5 cm/min.

The melt water stream is continuously separated into a water stream for chemical analysis and a gas stream for CH_4 concentration measurements. The gases are dried and forwarded to a liquid nitrogen (hereafter LN_2) trap. Here, sample gas accumulates for one minute and is then forwarded to a GC for concentration measurements. One measurement by the GC takes approximately three minutes, which corresponds to a depth resolution of 15–20 cm. Thus, the measurements are semi-continuous and yield a much higher temporal resolution than the discrete methods described above. The precision of the measurements is ±10–20 ppbv. Moreover, this technique does not require its own ice core samples, since it receives sample from the CFA system.

The semi-continuous method differs from the above described discrete methods only in its extraction technique. Discrete extraction techniques have been replaced with a continuous extraction process where gases are separated from the stream of melt water. The CH_4 concentration measurements are still carried out by a GC.

Besides the improved temporal resolution and the fact that the method does not require its own ice core sample the semi-continuous method has the advantage of almost fully-automated measurements which decreases the necessary amount of operating personal.

1.3 Advantages of using near-infrared spectroscopy

The novel method for measuring CH_4 concentrations presented in this thesis, is connected to the same gas extraction which is used by the semi-continuous GC-based method (cf. Section1.2). However, CH_4 concentration measurements are carried out by a near-infrared cavity ring-down spectrometer instead of a GC.

Advantages of the laser-based method are e.g. that it does not require a liquid nitrogen trap, it measures fully automated and is both robust and compact which makes it ideal for field deployment. Moreover, the measurements of the near-infrared spectrometer are very stable over time which simplifies the calibration procedure.

However, the most important advantage is the improved temporal resolution due to continuous measurements with a high repeatability (ca. 0.2 Hz). After accounting for dispersion of the sample in the system the temporal resolution is ca. 2 cm. The following section shows why high temporal resolution can be beneficial for paleoclimatic studies. The only drawback of the laser-based method is its precision of ca. ±25 ppbv.

1.4 The motivation for high-resolution records of CH_4

The temporal resolution of the laser-based method is estimated to be ca. 2 cm (cf. Appendix B). In the following it is explained why measurements of such high resolution can be beneficial for paleoclimatic studies.

The diffusion of gases in the firn column acts an an integrator over time which sets a limit for the optimal temporal resolution of gas concentration measurements. As a consequence of this diffusion, atmospheric air which is captured in bubbles at the pore close

Table 1.1: *An overview of the different techniques for measuring* CH_4 *from ice cores. The laser spectrometer is denoted with LS and extraction method with "extr".*

Method	extr.	detector	sampling	precision	resolution
GC-dry	dry	GC	discrete	± 20 ppbv	ca. 1m
GC-wet	wet	GC	discrete	± 10–15 ppbv	ca. 1m
GC-CFA	wet	GC	semi-continuous	± 10–20 ppbv	12–15 cm
Laser-CFA	wet	LS	continuous	± 25 ppbv	ca. 2 cm[a]

[a] In Appendix (B) we show how we estimate the resolution of our system.

off represents the composition of the atmosphere averaged over several years. The exact number of years depends on the gas species since the diffusion is gas specific and on the drilling site. In the case of CH_4 and the NEEM site this number is ca. 15 years (based on a firn diffusion model by Christo Buizert). In the ideal case, when measurements can resolve every annual layer along the ice core the temporal resolution of the CH_4 concentration measurement will be ca. 15 years.

At the upper part of the NEEM ice core annual layers are thicker than the temporal resolution of the laser-based method of 2 cm (average annual accumulation rate of 22.7 cm/year ice equivalent, Dorthe Dahl-Jensen). This implies that the method measures several times during an annual layer at this part of the core and no additional information can be gained from the high temporal resolution. However, the situation changes for the deeper part of the core, where annual layer thickness is less than 1 cm[1]. Here, a temporal resolution of 2 cm is useful to obtain detailed information about changes in atmospheric CH_4 concentration. High resolution measurements become even more important at sites with low annual accumulation, which is the case for many ice cores from Antarctica but also for some ice cores from Greenland, e.g. the GRIP core.

It can be concluded that the high temporal resolution of the laser-based method can reveal new information and improves the temporal resolution of records of atmospheric CH_4 concentration.

High-resolution records of atmospheric CH_4 concentration are often used to gain knowledge about the phase relationship (leads and lags) between the climate of the two hemispheres and between temperature and greenhouse gas records. However, existing records of atmospheric CH_4 concentration do usually not provide a temporal resolution which is high enough in order to understand these phase relationships. Discrete methods for measuring CH_4 concentrations are too time-demanding and labor-intensive in order to conduct the necessary amount of measurements along a deep ice core. Moreover, sample supply is limited. The high-resolution measurements of the laser-based method do not require extra ice

[1] An ice flow model by Susanne L. Buchardt [15] predicts that the annual layer thickness close to bedrock at NEEM is thinner than at NGRIP as a consequence of less basal melting at NEEM. For NGRIP the annual layer thickness close to bedrock is 1 cm [16]

samples and are fully automated which makes a high-resolution record along a complete ice core feasible.

In the following, two examples of paleoclimatic studies that used high-resolution records of atmospheric CH_4 concentration are presented.

- Blunier et al. [9] used high-resolution records of atmospheric CH_4 concentration to compare abrupt climate changes from Greenland and Antarctica and to understand the coupling between the climate of the two hemispheres. They concluded that warming in Antarctica preceded the onset of warming in Greenland for Dansgaard-Oeschger events 8 and 12 by ca. 1500 years.

  Records of atmospheric CH_4 concentration are well-suited for the synchronization of climate records between the northern and southern hemisphere. The reason being that long-lived atmospheric gases like CH_4 are well mixed in the atmosphere. Thus, they provide a global signal that can be used to correlate records from both hemispheres [17].

- Severinghaus et al. [18] investigated the abrupt climate change at the end of the Younger Dryas and found that atmospheric CH_4 concentrations slowly followed the abrupt change in temperature at the end of the Younger Dryas. In order to date the gas age they used the fractionation of nitrogen and argon isotopes which is in indicator for rapid temperature change. This comparison was possible since they had gas records of high temporal resolution during the end of the Younger Dryas.

Chapter 2

Ice cores as climate archives

2.1 Ice sheets and drilling sites

Ice sheets and glaciers that are well-suited for paleoclimatic studies only form under certain conditions. Ideally, they need year-round accumulation of snow and extremely low surface melt and sublimation even during summer [19]. These conditions are fulfilled in the central part of large ice sheets. Currently, only two major ice sheets exist: The Greenland ice sheet and the Antarctic ice sheet. Both are shown in Fig. 2.1 together with important drilling sites which are indicated with red rhombi.

Most of the drilling sites in Greenland are in the vicinity of the main ice divide which is indicated as a dashed gray line in Fig. 2.1. In Antarctica the situation is different where most drilling sites are located on domes (summits). The following paragraphs provide a brief and simple introduction of ice sheet dynamics which explains the distribution of ice core drilling sites. Detailed information on the dynamics of ice sheets and glaciers can be found e.g. in the book *"The Physics of Glaciers"* by Paterson [20].

An ice sheet gains mass from snow which falls on the surface of the ice sheet and looses mass at the margins. The mass balance of the ice sheet determines whether an ice sheet grows (positive mass balance) or retreats (negative mass balance). The ice sheet is said to be in steady-state when its total mass balance is zero. During steady-state the height of the ice sheet and the position of its margins are constant [20].

Even under steady-state conditions of an ice sheet, the ice itself is never static. On the contrary, ice constantly deforms and moves driven by the gravitational force. Fig. 2.2 shows a simple schematic of a cross section through the Greenland ice sheet. One can identify two major flow directions: An ice flow from the central part of the ice sheet towards the margins and a second flow direction from top to bottom [2]. The ice divide, indicated with a red vertical line, is located where the ice sheet is highest and separates opposing ice flow directions.

The ice flow at the ice divide is special. Here, the ice moves slowly and almost vertically towards bedrock. On their way down annual layers of ice are stretched and thinned due to the weight of overlaying snow and ice. This flow pattern is relatively simple compared to

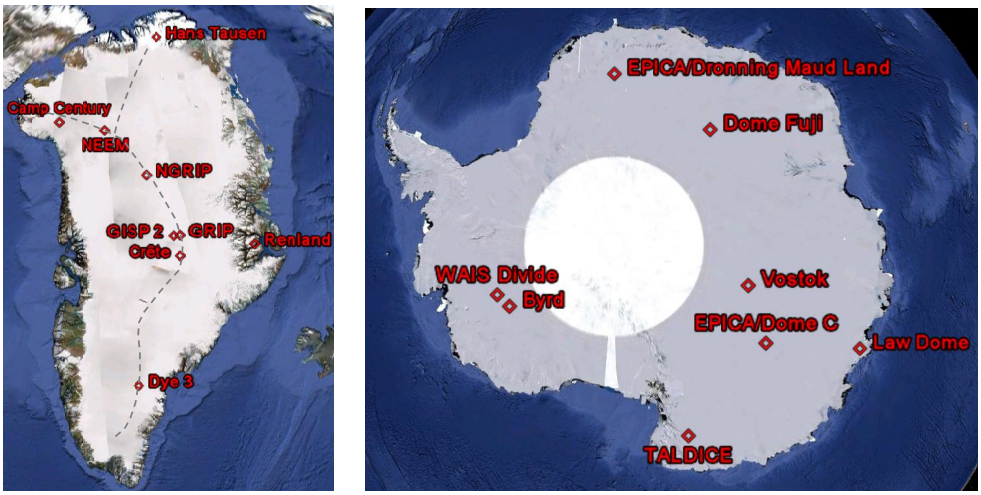

Figure 2.1: *Earth's two current major ice sheets are found in Greenland (left) and Antarctica (right). Red rhombi indicate important deep ice core drilling sites. The gray dashed line shows the approximate location of the main ice divide of the Greenlandic ice sheet. Both maps have been produced by Goggle Earth.*

locations off the ice divide and allows that the vertical annual layering is maintained along the core which simplifies the dating process since no upstream corrections are needed.

The relatively simple dating of ice cores drilled at the ice divide makes these ice cores well-suited for studies of paleoclimate. Furthermore, the ice is thickest at the ice divide and the oldest ice is often found here. These advantages apply also for ice cores that are drilled at domes on the Antarctic ice sheet where the pattern of ice flow is comparable to the one at the ice divide.

On the other hand, dating and interpretation of climatic data are more complicated at places off the ice divide. Here, one has to correct for upstream effects. Nevertheless, there are several reasons for drilling ice cores at locations off the ice divide or off domes. Among others, these ice cores yield information about regional climate or about past elevations changes of the ice sheet [21].

From the NEEM project scientists hope to retrieve the first ice core from Greenland that includes well-resolved ice from the complete previous interglacial period called the Eemian (approximately 131,000–114,000 years b2k[1]). So far, the oldest undisturbed ice found in Greenland dates back to 123,000 years b2k [16] and stems from the NGRIP site with an average annual accumulation rate of 19 cm/year [23]. Ice as old as 250,000 years has been found in the GRIP core but cannot be used for paleoclimatic studies since rough bedrock topology mixed the oldest part of the ice and dating is questionable [24]. Ice found in Antarctica can be much older, up to ca. 800,000 years [25], due to the low annual accumulation rate of only 3 cm in certain parts of Antarctica [26].

[1]The notation b2k was introduced together with a new timescale for the NGRIP, GRIP and DYE-3 ice cores which is called Greenland Ice Core Chronology 2005. B2k means years before A.D. 2000 [22].

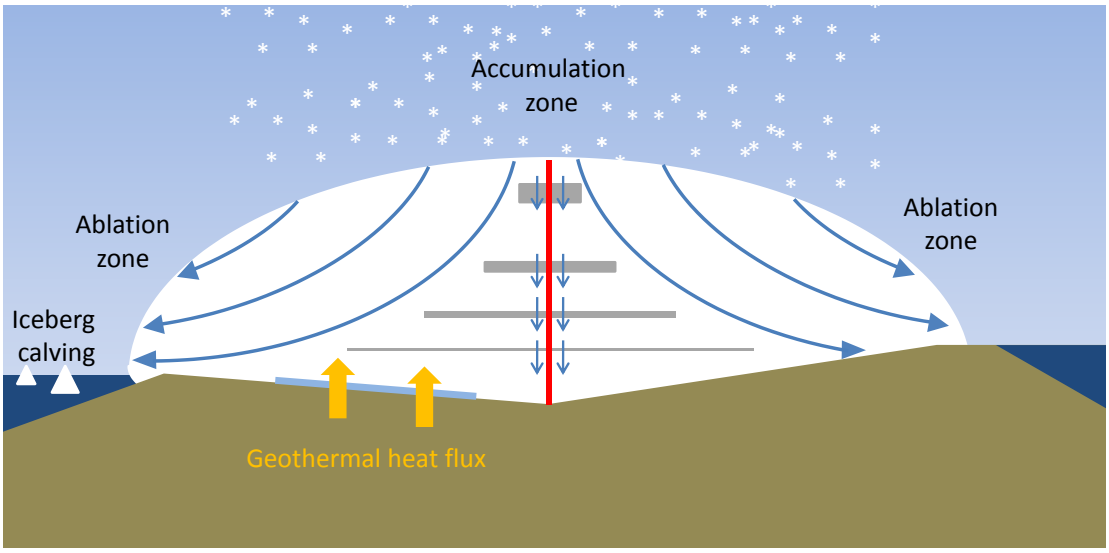

Figure 2.2: *Schematic drawing of the cross section of the Greenland ice sheet. Ice flows from high elevations, where precipitation exceeds snow melt, to low elevations where ablation (melting, calving) dominates. Close to the ice divide (red line) the flow is slow and mostly vertical, which makes drilling sites at or close to the ice divide convenient for paleoclimatic studies.*

2.2 Climatic information from ice cores

There are numerous climate signals which can be measured along an ice core. The following sections introduce some of the most important climate signals that can be found in ice cores.

2.2.1 Stable water isotopes

The ratio of stable isotopes of water in precipitation over Greenland shows a seasonal signal which is preserved in ice cores. The isotopic composition of water is usually denoted with δ values and is given in per mil as

$$\delta^{18}O = \frac{R^{18}_{\text{measured}} - R^{18}_{\text{standard}}}{R^{18}_{\text{standard}}} \cdot 1000‰ \quad \text{with} \quad R^{18} = \frac{^{18}O}{^{16}O}, \tag{2.1}$$

$$\delta D = \frac{R^{D}_{\text{measured}} - R^{D}_{\text{standard}}}{R^{D}_{\text{standard}}} \cdot 1000‰ \quad \text{with} \quad R^{D} = \frac{^{2}H}{^{1}H}. \tag{2.2}$$

Snow that is deposited at high elevations on the Greenland ice sheet originates mostly from water vapor sources in the suptropical part of the North Atlantic Ocean [27]. On the way from this low latitude source to the ice sheet the air masses are cooled down. This leads to precipitation and a preferential fallout of the heavy isotopes of water via a Rayleigh distillation process. Precipitation occurs more frequently during the cold winter months. This leads to a higher depletion of heavy water isotopes in winter precipitation over the ice sheet and causes the seasonal signal which can be used e.g. to date the upper part of the core [28, 29].

This points to a relation between the isotopic composition of precipitation over Greenland and condensation temperature. Based on measurements of isotopic compositions of present precipitation from different latitudes Willi Dansgaard [28] found a linear relation between the $^{18}\delta$ and the temperature for high latitudes. Based on this concept past temperatures have been reconstructed from measurements of the isotopic composition of water from ice cores.

However, the seasonal signal gets smoothed out by diffusion in the firn [30]. Thus, measurements of stable water isotopes from ice cores sometimes have to be corrected for firn diffusion before they can be used for dating or reconstructions of past temperatures [31, 30]. Fig. 2.3 shows measurements of stable water isotopes from three Greenland ice cores. The measurements from the NGRIP and GRIP ice cores had to be corrected for firn diffusion, whereas the measurements from the DYE-3 core could be used for dating without corrections. This dating procedure does not work for the deep parts of an ice core were annual layers are to thin to be resolved.

2.2.2 Impurities

Numerous impurities, soluble and insoluble, are stored in solid precipitation that is deposited on an ice sheet, among them e.g. sodium, calcium or sulfate. Impurities deposited on an ice sheet contain much climatic information, e.g. about volcanic or human activities. Cole-Dai et al. [32], for instance, used precisely dated measurements of sulfur isotopes to show that the very cold decade from 1810–1819 originated from strong volcanic activity in the tropics. Traces of these eruptions can be found not only in tropical glaciers but in Greenland and Antarctica as well.

A nice example of how human activities leave their fingerprint on ice sheets are lead measurements conducted by Hong at al. [33]. They found pronounced lead pollution of the Greenland ice sheet already in preindustrial times, e.g. during the time of the Roman and Greek empires (500 B.C. to 300 A.D.) as a consequence of enhanced silver mining and smelting activities.

Furthermore, impurity signals measured from ice cores often show a seasonal or annual pattern which makes them well-suited for dating purposes. Examples are sodium and chloride ions which are blown from the ocean onto the ice sheet predominately during storms in spring [22, 34]. For a more detailed overview over glaciochemistry see e.g. the review by Legrand and Mayewski [35].

To extract and analyze chemicals, the ice cores are either cut in small pieces and analyzed individually or continuously melted in a CFA system. Here several chemicals are measured simultaneously from the continuous melt water stream.

2.2.3 Conductivity

Electrical conductivity measurements (ECM) and dielectric profiling (DEP) are fast, inexpensive and non-destructive techniques that provide information about the ionic content of the ice [36, 37]. They are usually conducted in the field during ice core processing.

Low conductivities of ice are caused by alkaline dust particles which point to periods of cold climate. During cold periods dust particles are blown frequently from barren lands onto the ice sheets. Furthermore, volcanic eruptions leave traces in the ice in the form of acidic layers (sulfuric acid) detectable by ECM and DEP or sometimes even in the form of visible ash particles. Eruptions of volcanoes from the northern hemisphere can be detected in ice cores from Greenland [38], whereas severe eruptions from tropical volcanoes can be detected in both ice cores from Greenland and Antarctica [39].

Dust particles as well as ash layers help to provide a fast but rough time scale of an ice core. Annual spring storms blow dust and sand particles from Eurasia, eastern North America and western Europe onto the Greenland ice sheet [40] which show up as spikes of low conductivity in ECM and DEP measurements. Ash layers or tephra can be assigned to known volcanic eruptions [41] and act as reference horizons which can be used to synchronize time scales of different ice cores or to link ice cores with other climate archives. Synchronization of time scales of three Greenland ice cores with the help of a volcanic eruption detected in ECM measurements is shown in Fig. 2.3.

2.2.4 Atmospheric trace gases

Past concentrations of atmospheric trace gases can be measured from ice cores, including greenhouse gases such as CO_2, CH_4 and N_2O. Atmospheric air is trapped in the ice in form of bubbles as shown in Fig. 2.4.

Fig. 2.4 also shows the process of gas inclusion in the ice. Although the gradually compressed firn is denser than snow, gases can diffuse through firn and are in contact with the atmosphere. Eventually, at depths between 60 and 110 m, the pressure becomes high enough to transform firn into ice and open spaces are closed off (close-off zone). Here, air is trapped in bubbles which follow the flow of ice towards bedrock.

As a consequence of the gas diffusion in the firn, the age of gases which are trapped in the close-off zone is younger than the ice that surrounds them. The knowledge of this age difference, the Δ age, is essential in order to find a correct timescale for gas measurements from ice cores. The Δ age depends on temperature and accumulation rate and can be estimated e.g. from the empirical firn densification model by Herron and Langway [42].

When an ice core is retrieved, the trapped air can be extracted either by melting (wet extraction) or by crushing/crating/sublimation (dry extraction). More information about gas extraction and established techniques for measuring gas concentrations from ice cores can be found in Section 1.3.

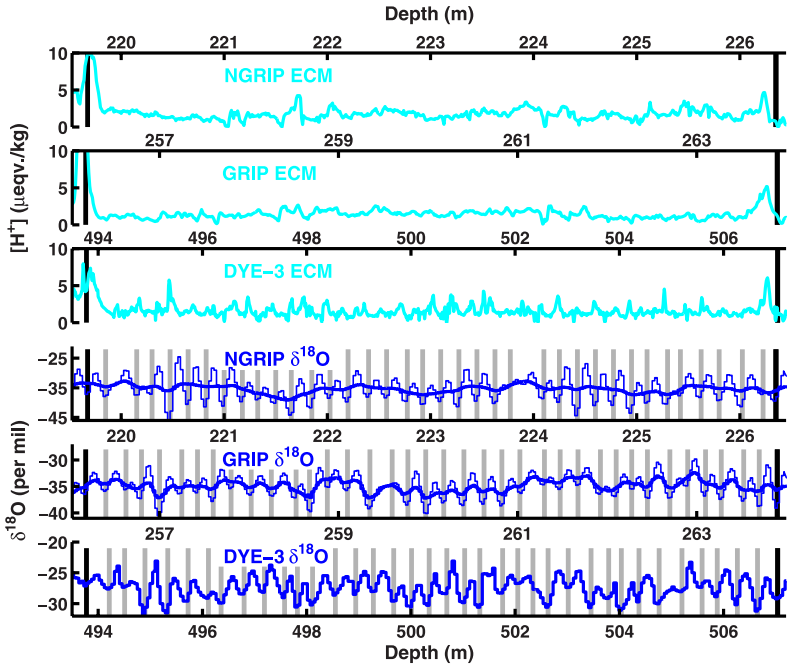

Figure 2.3: *Top three graphs: Matching of the DYE-3, GRIP, and NGRIP ECM records from A.D. 897 to A.D. 934. Reference horizons are indicated by black bars. Bottom three graphs: Detailed comparison of stable isotope records. Thick blue lines are measured data, while thin lines are deconvoluted data, corrected for firn diffusion. Light gray bars indicate single years (winters) identified in the records [30].*

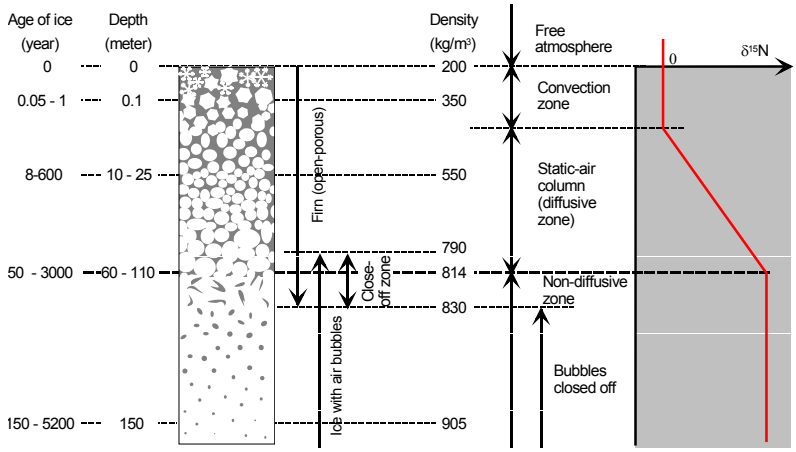

Figure 2.4: *The process of firn densification and the associated gas occlusion. The stable isotope ratio of nitrogen, $\delta^{15}N$, is used to identify the different gas processes in the firn column. In the convection zone the gases are in equilibrium with the atmospheric layer above the snow surface. Then, in the diffusive zone the gas exchange with the atmosphere is transmitted predominately by diffusion and the composition of air begins to deviate from the present atmospheric composition. After the close off zone gases are completely separated from the atmosphere.*

Chapter 3

Theory of measurement

This chapter describes the theory of measurement of the near-infrared cavity ring-down spectrometer (hereafter NIR-CRDS). Section 3.1 introduces the basic principles of absorption spectroscopy and how it can be used to measure molecular concentrations. Then, Section 3.2 takes a closer look specifically into the interaction of near-infrared radiation with CH_4 molecules. Finally, Section (3.3) describes how this interaction is used in the NIR-CRDS to determine molecular concentrations from ring-down time measurements.

3.1 Concentration measurements via absorption spectroscopy

When light of intensity I_0 passes through a volume that contains absorbing molecules, the light intensity is attenuated (how molecules absorb electromagnetic radiation is discussed in detail in Section 3.2). This attenuation is described by the Lambert-Beer law as

$$I = I_0 e^{-\alpha(\nu)l}, \tag{3.1}$$

with the transmitted intensity I in energy/m^2, the frequency-dependent absorption coefficient or "loss" $\alpha(\nu)$ in mol/cm and the length of the path of interaction l. The absorption coefficient is related to the molar concentration n by

$$\alpha(\nu) = \sigma(\nu)n, \tag{3.2}$$

where $\sigma(\nu)$ is the absorption cross section in cm^2 and n is the molar concentration in mol/cm^3. The relation between absorption cross section and light frequency ν is given by the temperature and pressure dependent line shape function f as

$$\sigma(\nu) = S(T) \cdot f(\nu - \nu_0, T, p), \tag{3.3}$$

with the temperature-dependent line strength $S(T)$ in cm/mol. The line shape function describes the shape of the absorption line and is centered around the frequency ν_0. It is

normalized such that

$$\int_{-\infty}^{\infty} f(\nu)d\nu = 1 \tag{3.4}$$

The line strength S is an intrinsic property of a molecule. It depends on the temperature-dependent distribution of population among the available internal energy levels of the molecules. In the case of a local thermodynamic equilibrium, this distribution of population is described by the Maxwell-Boltzmann distribution. Line strengths for many molecules and temperatures can be found in the HITRAN database [43]. The theory of line strength is described in detailed in work by Toth [44]. From Eqs. (3.2) and (3.3) it follows that

$$\alpha(\nu)l = S(T)f(\nu - \nu_0, T, p)nl, \tag{3.5}$$

which can be used to determine the molar concentration n of the absorbing molecular species. The absorption coefficient $\alpha(\nu)$ can be determined from measurements of incident and transmitted light intensity as shown in Eq. (3.1). The path length l is a known parameter depending on the experimental setup. The remaining unknown parameter in Eq. (3.5) is the line shape function f. In the following, several effects which influence the line shape and the different models that are used to approximate the line shape function are presented.

For the theoretical case of static and completely independent (non-interacting) molecules the line width is minimal and called natural line width. This natural width is set by Heisenberg's uncertainty principle that states that the uncertainty in energy ΔE of a certain transition is inversely proportional to the lifetime of the excited state:

$$\Delta E \Delta t \geq \hbar, \tag{3.6}$$

with the lifetime Δt and the reduced Planck constant $\hbar$. The shape of a natural broadened spectral line follows a Lorentzian profile. However, some effects tend to broaden the line width of any absorption line.

- **Doppler-broadening:** Thermal movement of molecules causes Doppler-broadening of the spectral lines. The distribution of velocities of the absorber molecules allow light of several frequencies to be absorbed. The resulting broadened spectral line has the shape of a Gauss profile and is given by the function f_G as [45]

$$f_G(\nu - \nu_0) = \frac{1}{\gamma_G}\sqrt{\frac{\ln 2}{\pi}} e^{-(\nu-\nu_0)^2 \frac{\ln 2}{\gamma_G^2}}. \tag{3.7}$$

  with γ_G the Half Width at Half Maximum (hereafter HWHM) which is given by

$$\gamma_G = \frac{\nu_0}{c}\sqrt{2 \ln 2 \frac{kT}{m}}, \tag{3.8}$$

  where c is the speed of light, T the temperature of the gas and m the mass of the absorber molecules. The slow flow of the sample through the cavity does not induce a recognizable Doppler effect.

- **Pressure-broadening:** Higher pressure in the sample gas results in a higher molecular density and, as a consequence, collisions and other interactions between molecules become both more frequent and stronger. Collisions and other interactions slightly change the energy that is necessary to excited some of the molecules. As a consequence, these molecules absorb light of different wavelengths and the line width becomes broader. A pressure broadened line has the shape of Lorentzian distribution and is described by the function f_L as [45]

$$f_L(\nu - \nu_0) = \frac{(\gamma_L/\pi)}{(\nu - \nu_0)^2 + \gamma_L^2}, \tag{3.9}$$

  where γ_L is the HWHM of the line which can be found for many molecules on the HITRAN database.

In most cases, including the experiments described in this thesis, the absorption lines are affected by both Doppler- and pressure-broadening. In such cases, the Voigt function $V(\nu - \nu_0)$ is often a good approximation to describe the profiles of absorption lines. It is a convolution of the Gaussian function with the Lorentzian function:

$$V(\nu - \nu_0) = f_L * f_G. \tag{3.10}$$

The convolution means that the Voigt profile approaches the Lorentzian profile for high pressures whereas it approaches the Gaussian profile for low pressures and/or high temperatures. Inserting Eqs. (3.7) and (3.9) in Eq. (3.10) yields ($\nu - \nu_0$ substituted with x)

$$V(x) = \frac{\gamma_L\sqrt{\ln 2}}{\gamma_G\pi^{3/2}} \int_{-\infty}^{\infty} \frac{e^{-\ln 2}(x'/\gamma_G)^2}{(x - x')^2 + \gamma_L^2} dx', \tag{3.11}$$

where the definition of convolution is used:

$$(f * g)(t) = \int_{-\infty}^{\infty} f(t - \tau)g(\tau)d\tau. \tag{3.12}$$

In some cases an extension of the Voigt profile is necessary in order to measure gas concentrations with higher precision . The reason for this being collisions between molecules which tend to change the velocities of the molecules, an effect known as Dicke narrowing of the Doppler profile [46]. Especially for pressures below 120 mbar, i.e. when the Voigt profile is dominated by the Doppler-broadening, taking Dicke narrowing into account improves the resemblance between the calculated line shape and observations. One distinguishes between two physical models that describe the narrowing effect on the absorption lines. Let the mass of the absorber molecule and the perturber be denoted with m_1 and m_2, respectively:

- Rautian model when $m_1 \ll m_2$.
- Galatry nodel when $m_1 \ll m_2$.

The narrowing effect is characterized by a single parameter β_0. Further information about the two models can be found e.g. in work by Lepère [47].

In practice one fits Voigt line shapes in combination with one of the two models to the measured absorption spectra. The fit parameters such as spectral line position, line intensities, the narrowing parameter β_0 and Gaussian and Lorentzian line widths are optimized by minimizing the residuals of the fit. The area under the fit is linearly proportional to the molar concentration of absorber molecules. Fig. 3.1 shows an absorption spectrum of CH_4 (red) as measured by the NIR-CRDS at a pressure of 222 mbar and a temperature of 45°C. The dashed black line is a pressure-broadened profile (Lorentzian) calculated from Eqs. (3.9) and (3.5) where the center frequency ν_0, the HWHM and the line strength $S(T)$ are extracted from the HITRAN database (David Balslev-Clausen, personal communication 2010).

The differences between the measured and calculated profile show that Doppler effects cannot be neglected. The calculated profile is narrower, which can be explained by the thermal movement of the molecules which the Lorentzian profile does not take into account. Furthermore, there is an offset between the losses of the two profiles. This is due to the empty cavity losses that add to the absorption losses in the case of the measured profile.

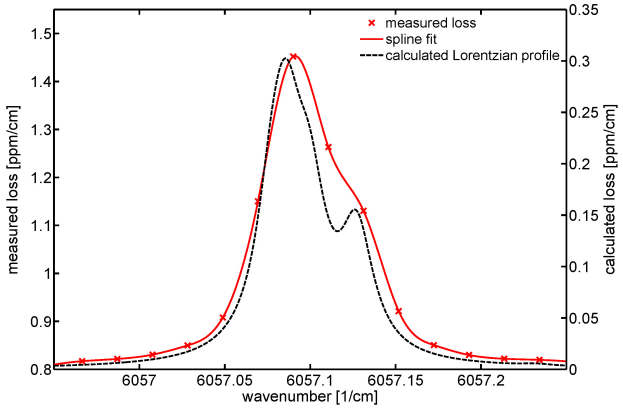

Figure 3.1: *The loss as measured by the NIR-CRDS (red) for dry air with a CH_4 concentration of 2650 ppbv at a cavity pressure of 222 mbar and a calculated Lorentzian profile (black). The parameters for the profile were extracted from the HITRAN database.*

The molar concentration n of the absorber molecules (which is determined from the area under the fit) can be transformed to the concentration of these molecules in the total sample as

$$C = \frac{n}{n_{\text{sample}}}, \tag{3.13}$$

where n_{sample} is the number density of all molecules in the sample cell which can be derived from the ideal gas law as

$$n_{\text{sample}} = \frac{N_{\text{sample}}}{V} = \frac{p}{k_B T}, \tag{3.14}$$

with the total number of molecules in the cavity N_{sample}, the Boltzmann constant k_b and the volume, pressure and temperature of the sample cell V, p and T, respectively. The concentration of CH_4 is usually denoted in ppbv, i.e. the number of CH_4 molecules found in one billion molecules in the cavity per unit volume.

3.2 CH_4 measurements via near-infrared spectroscopy

Molecules can absorb electromagnetic energy in different ways depending on the frequency. Visible or ultraviolet radiation is absorbed by exciting electrons and thereby inducing electronic transitions in the molecule.

Microwave radiation, on the other hand, induces changes in the rotational state of the molecule, i.e. the absorbed energy is used to rotate the molecule around one of its rotational axes.

Radiation from the infrared regime, as used by the NIR-CRDS, is absorbed by inducing changes in the vibrational state of the molecules. The absorbed radiant energy lets the molecule oscillate around its equilibrium position. Every non-linear molecule consisting of N atoms has 3N-6 fundamental vibrational degrees of freedom and, in the case of the CH_4 molecule, four of them can in principle be excited by infrared radiation. However, due to the highly symmetric shape of the CH_4 molecule only two vibrational modes can be excited by the absorbance of near-infrared radiation. These two, the ν_3 and ν_4 vibrational modes, are shown in Fig. 3.2. They absorb infrared radiation with a wavenumber (wavelength) of 3156.8 cm^{-1} (3.2 μm) and 1367.4 cm^{-1} (7.3 μm), respectively [48].

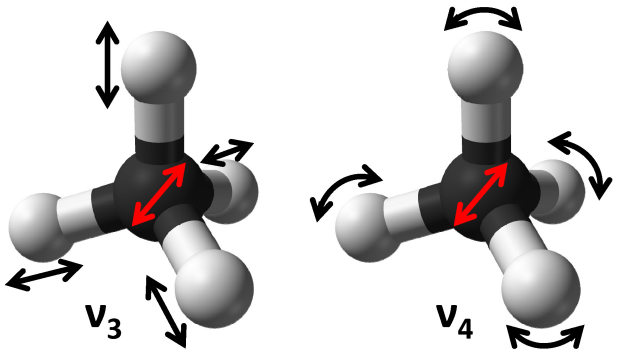

Figure 3.2: *The two vibrational modes of the* CH_4 *molecule that can be excited by the absorption of infrared radiation. The* ν_3 *and* ν_4 *vibrational modes absorb electromagnetic radiation with wavenumber 3156.8 and 1367.4* cm^{-1}*, respectively.*

The NIR-CRDS uses near-infrared radiation with a wavenumber (wavelength) of ca. 6057 cm^{-1} (1.7 μm). Thus, this radiation cannot excite any of the fundamental vibrational modes of CH_4 shown in Fig. 3.2. Instead, radiation of this wavenumber excites four overtones of the ν_3 vibrational mode. The line strengths of these overtones and their position in

the infrared spectrum are shown on the left plot of Fig. 3.3. The energies of the overtones are not exact multiples of the energy of the fundamental vibrational mode. They already occur at lower energies for reasons which are explained in the following paragraphs.

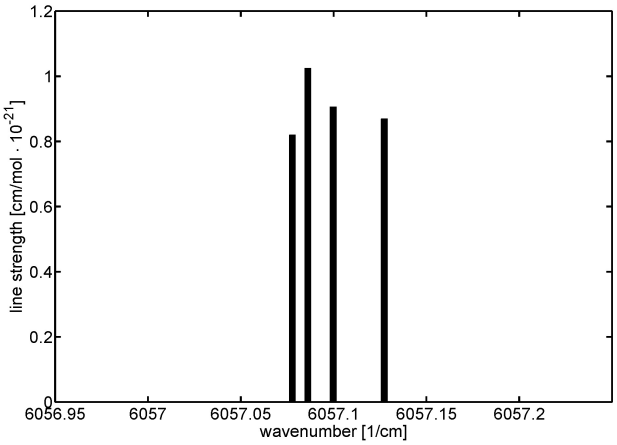

Figure 3.3: *The line strengths of the CH_4 absorption lines which are measured by the NIR-CRDS for $T = 45°C$ and $p = 222$ mbar (from the HITRAN database). Absorption of radiation at these wavenumbers excites overtones of the fundamental vibrational mode ν_3.*

The vibrational modes and their overtones can be approximated with the parabolic harmonic oscillator model [49]. Here, the molecule is treated as a particle in a parabolic potential with the potential energy $E_{pot} = \frac{1}{2}Dx^2$ and the pulling force $\mathbf{F} = -\mathbf{grad}E_{pot} = -Dx$. The Schrödinger equations becomes

$$-\frac{\hbar^2}{2m}\frac{d^2\psi}{dx^2} + \frac{1}{2}Dx^2\psi = E\psi, \tag{3.15}$$

with m the mass of the particle, D a spring constant, ψ the wave function and x the displacement from equilibrium position x_e. From the harmonic oscillator model one knows that the frequency of oscillations ν is given by [49]

$$\nu = \sqrt{D/m}, \tag{3.16}$$

and Eq. (3.15) becomes

$$-\frac{\hbar^2}{2m}\frac{d^2\psi}{dx^2} + \frac{1}{2}\nu^2 mx^2\psi = E\psi. \tag{3.17}$$

Solving Eq. (3.17) leads to a discrete energy spectrum with energies given by

$$E(n) = \left(n + \frac{1}{2}\right) \cdot \hbar\nu \;\text{ with }\; n = 0, 1, 2, \ldots, \tag{3.18}$$

with the quantum number for vibrational modes n. The allowed energy levels are equally spaced with distances of $\Delta E = \hbar\nu$. For energies close to the ground state ($n = 0$) the parabolic harmonic oscillator potential is a good approximation . With increasing energy

the approximation becomes worse and other potentials are necessary to calculate the vibrational energies E of the energy levels accurately. A very good approximation to the real molecular potential is the Morse potential which is given by

$$E_{pot}(x) = E_D \cdot \left(1 - e^{-a(x-x_e)}\right)^2, \tag{3.19}$$

with the Morse constant a and the dissociation energy E_D. The Morse potential converges towards the dissociation energy for $x \to \infty$ and has its minimum $E_{pot}(x_e) = 0$ at $x = x_e$. When using the Morse potential in the Schrödinger equation, one finds the energies of the allowed energy levels to be

$$E(n) = \left(n + \frac{1}{2}\right)\hbar\nu - \frac{\hbar^2\nu^2}{4E_D}\left(n + \frac{1}{2}\right)^2. \tag{3.20}$$

The energy levels are not equidistant as for the parabolic harmonic oscillator potential but decrease with increasing vibrational quantum number n as

$$\Delta E(n) = \left[1 - \frac{\hbar\nu}{2E_D}(n+1)\right]\hbar\nu. \tag{3.21}$$

The decreasing distance between the allowed energy levels explains the experimental observation that overtones are not excited by a multiple of the radiant frequency that excites the fundamental vibrational mode but already at smaller frequencies. This applies for the overtones of the ν_3 fundamental vibrational mode which are measured by the NIR-CRDS too. They occur at lower frequencies as twice the frequency of the fundamental mode as shown in Fig. 3.1. Fig. 3.4 shows a sketch of the parabolic potential and the Morse potential including their energy levels.

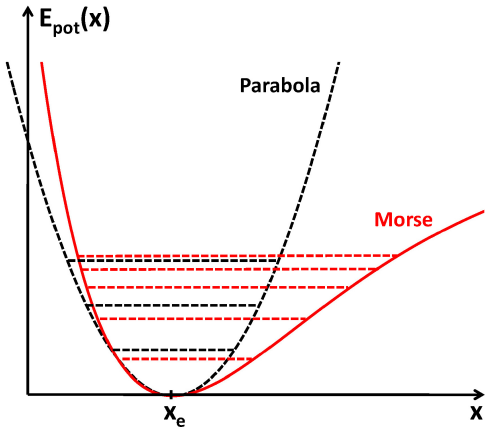

Figure 3.4: *Comparison of the parabolic harmonic oscillator potential and the Morse potential and the corresponding energy levels. For the Morse potential, which describes a real molecule very well, the energy levels are not equally spaced.*

3.3 Measurements of cavity ring-down time

In Section 3.1 it is shown how the concentration of molecules can be determined from the Lambert-Beer law by measuring the difference between the intensities of incident and transmitted light. However, the spectrometer utilized during the experiments which are described in this thesis uses measurements of cavity ring-down time (hereafter CRD time) instead of intensity measurements. In the following it is described how the concentration of absorber molecules can be determined from CRD time measurements.

In a continuous wave cavity ring-down spectrometer (hereafter cw-CRDS) laser light with a precisely known wavelength is seeded into a high-finesse cavity that contains the gaseous sample as illustrated in Fig. 3.5. Wavelength and path length are adjusted in order to achieve mode matching between the laser and the cavity mode (cf. Chapter 4). During mode matching intensity starts to build up. The laser is shut off after a certain threshold intensity, I_{th}, has been reached and the intensity in the cavity begins to decay exponentially as shown in Fig. 3.6. CRD time is then defined as the time it takes for I_{th} to decay to I_{th}/e.

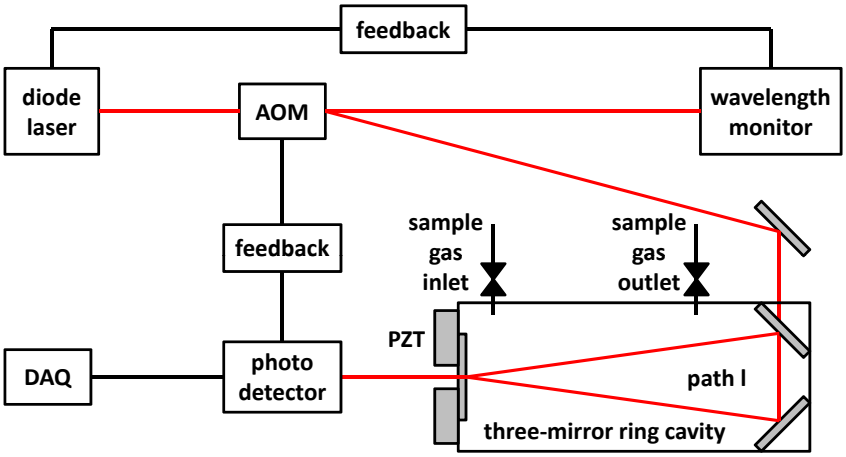

Figure 3.5: *Schematics of a typical continuous-wave diode laser CRDS on the basis of Mazurenka et al. [50]. Red lines indicate the laser beam. An acousto-optic modulator (AOM) splits the beam. One beam is used for wavelength measurements whereas the second is sent into the sample cavity. The gaseous sample is continuously flushed through the cavity where the laser light bounces between three high-reflecting mirrors with the path length of one round-trip l. The length of the cavity can be altered with the use of a piezoelectric transducer (PZT). A data acquisition system (DAQ) stores and displays the measurements.*

The blue curve in Fig. 3.6 shows CRD time for an empty cavity, where intensity is lost only through the mirrors and due to scattering on the walls (empty cavity looses). However, CRD time becomes shorter when absorber molecules are present (red curve), since they absorb radiant power on top of the empty cavity looses. Thus, CRD time is directly related to the concentration of these absorber molecules.

The following paragraphs present a mathematical treatment of CRD time. The calculations are valid for a three-mirror ring cavity and cw lasers as used by the NIR-CRDS. A summary of CRD time measurements for the more traditional case of a two-mirror cavity in combination with a pulsed laser can be found in the review of Mazurenka et al. [50].

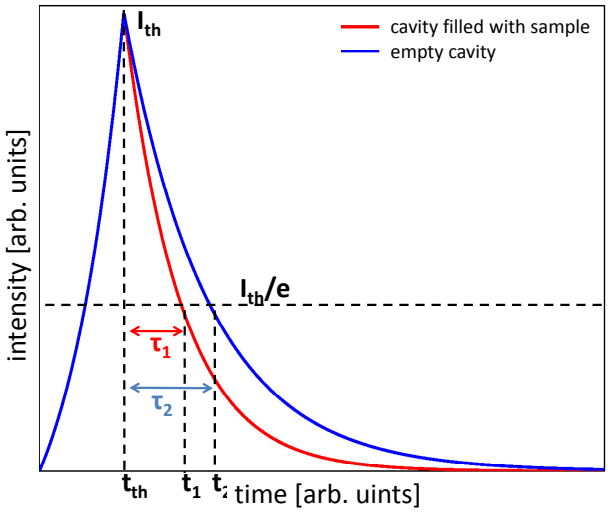

Figure 3.6: *Illustration of CRD time for an empty cavity (blue) and for a cavity filled with absorbing sample molecules (red), respectively. CRD time is defined as the time it takes for the threshold intensity I_{th} to decay to I_{th}/e. CRD time for a sample-filled cavity (τ_1) is shorter than for an empty cavity (τ_2). The reason being the absorbing sample molecules which decrease the intensity further, on top of the empty cavity losses.*

Measurements of CRD time start when the intensity in the cavity reaches the threshold intensity I_{th} and the laser beam is interrupted. During each subsequent round trip the beam is reflected at three mirrors with reflectivity R and passes a triangular path with distances l. The intensity after n round trips is given by

$$I(n) = (R^3 e^{-3\alpha l})^n I_{th} = I_{th} e^{-3n(-\ln R + \alpha l)}, \tag{3.22}$$

where α is the absorption coefficient of the absorber molecules. The discrete variable n can be replaced with a continuous time variable $t = nl/c$ (c: speed of light), which is the time the light spent in the cavity and traveled n round trips each of distance l, and Eq. (3.22) becomes

$$I(t) = I_{th} e^{-\frac{3ct}{l}(-\ln R + \alpha l)}. \tag{3.23}$$

CRD time τ is defined as the time it takes the initial threshold intensity I_{th} to decrease to I_{th}/e:

$$\tau = \frac{l}{3c(-\ln R + \alpha l)}. \tag{3.24}$$

When using modern mirrors with $R \geq 0.9999$ one can use the approximation

$$\ln R \approx -(1 - R) \tag{3.25}$$

for $R \to 1$ and Eq. (3.24) becomes

$$\tau = \frac{l}{3c((1-R)+\alpha l)}. \tag{3.26}$$

From Eq. (3.26) it becomes clear that CRD time does not depend on the intensity of the laser and, therefore, cannot be influenced by noisy fluctuations in the laser intensity. Furthermore, CRD time measurement is an absolute measurement with a high signal-to-noise ratio, unlike the difference in intensities which are measured when using the Lamber-Beer law.

As mentioned earlier, intensity decay is not only due to the absorption of light by absorber molecules. Even an empty cavity involves losses for which one has to account when determining concentrations from CRD time measurements. Furthermore, it is noteworthy that the CRD time of an empty cavity, τ_0, can be measured and used for a precise determination of mirror reflectivity R:

$$\tau_0 = \frac{l}{3c(1-R)}. \tag{3.27}$$

From τ and τ_0 the absorption coefficient α, can be calculated. Rewriting Eq. (3.26) yields

$$\frac{l}{3c\tau} - (1-R) = \alpha l, \tag{3.28}$$

where the term $(1-R)$ can be replaced with $l/3c\tau_0$ obtained from rewriting Eq. (3.27). Then, Eq.(3.28) becomes

$$\frac{l}{3c\tau} - \frac{l}{3c\tau_0} = \alpha l. \tag{3.29}$$

By rearranging Eq. (3.29) one finds an expression for the absorption coefficient as

$$\alpha = \frac{1}{3c}(\frac{1}{\tau} - \frac{1}{\tau_0}). \tag{3.30}$$

From the calculated absorption coefficient and the known absorption cross section σ one can determine the concentration C of the absorber molecules as

$$C(\nu) = \frac{\alpha(\nu)}{\sigma(\nu)}. \tag{3.31}$$

Note that both, absorption coefficient, absorption cross section and concentration depend on the wavenumber of the absorbed laser light. As explained in Section 3.1, a molecule does not absorb radiation of exactly one wavenumber. The absorption line is broad and one has to repeat the CRD time measurement for several wavenumbers in order to determine the complete line shape. Then, the concentration of absorber molecules is proportional to the area under the absorption line.

To be able to determine absorber concentrations with high precision it is necessary to measure such a complete absorption line rather than determining concentration from only

one CRD time measurement. The reasons for this are the pressure broadening and Doppler effects presented in Section 3.1. As a consequence of these effects tiny changes in the measuring conditions can lead to significant changes in the shape of the absorption feature, for instance peak shifts or broadening effects. By measuring the complete absorption feature one takes these effects into account. In Section 3.1 we explain how an absorption feature can be approximated from only a few CRD time measurements as illustrated in Fig. 3.1.

The limit of sensitivity of CRD time measurements is given by the minimal detectable change in CRD time, $\Delta\tau_{\min} = \tau_0 - \tau$. For $\tau \to \tau_0$ it follows that $\Delta\tau \to \Delta\tau_{\min}$ and Eqs. (3.30) and (3.31) become

$$\alpha(\nu)_{\min} = \frac{1}{3c}(\frac{\Delta\tau_{\min}}{\tau_0^2}), \tag{3.32}$$

$$C(\nu)_{min} = \frac{\alpha(\nu)_{\min}}{\sigma(\nu)}. \tag{3.33}$$

The NIR-CRDS achieves its high precision by scanning over a complete absorption feature of CH_4 which includes 4 overtones. For this purpose the spectrometer measures CRD times for 14 different wavelengths (ca. 30 CRD times per wavelength) as shown on the right of Fig. 3.1. The area under the absorption feature is determined by a fit to these 14 points in spectral space.

Chapter 4

Instrumentation

The purpose of this chapter is to provide the reader with the theory of measurement and the specifications of the instruments utilized in the different experiments. The NIR-CRDS is used for measurements of CH_4 concentration. The theory of measurement is described in more detail in Chapter 3. Specifications of the NIR-CRDS are presented below in Section 4.1. Two instruments for measurements of total air content are used during the experiments: An Oxygen Sensor and a Thermal Conductivity Detector which are presented in Sections 4.2 and 4.3, respectively.

4.1 Picarro $CH_4/CO_2/H_2O$ analyzer

This section presents the mode of operation of the NIR-CRDS ($CH_4/CO_2/H_2O$ analyzer, model G1301, Picarro Inc.) and points out the few but significant differences between this spectrometer and a typical cavity ring-down system as described in Chapter 3. Specifications of the NIR-CRDS are listed in Table 4.1. Most of the information found in this section was provided by the manufacturer Picarro via literature (e.g. [51]) or personal communication.

The NIR-CRDS consists of a Power Vacuum Unit (hereafter PVU) and a Data Acquisition System (hereafter DAS). The DAS itself consists of two temperature stabilized compartments: The "Warm Box" (45.5°C) contains the two lasers whereas the "Hot Box" (45°C) contains the sample cavity[1]. The complete system is shown in Fig. 4.2.

Two telecom-grade distributed feedback (DFB) lasers are located in the Warm Box and are tuned via current and temperature to emit near-infrared radiation which can be used to measure absorption lines of the gases in question. One laser emits radiation with wavelengths (wavenumber) around 1603 nm (6238 cm^{-1}) to measure an absorption feature[2]

[1]For some reason the "Warm Box" is warmer than the "Hot Box". So far we have not been able to disclose this secret of Picarro's mysterious terminology.

[2]The use of the word "absorption feature" instead of absorption line indicates that the measured absorption spectrum covers more than one line. For instance the CH_4 absorption feature measured by the NIR-CRDS, which covers four overtones of the ν_3 fundamental vibrational mode as explained in Chapter 3.

of CO_2, whereas the second laser uses wavelengths around 1651 nm (6057 cm^{-1}) to measure the absorption features of CH_4 and H_2O. The absorption fearures measured by the second laser are shown in Fig. 4.1.

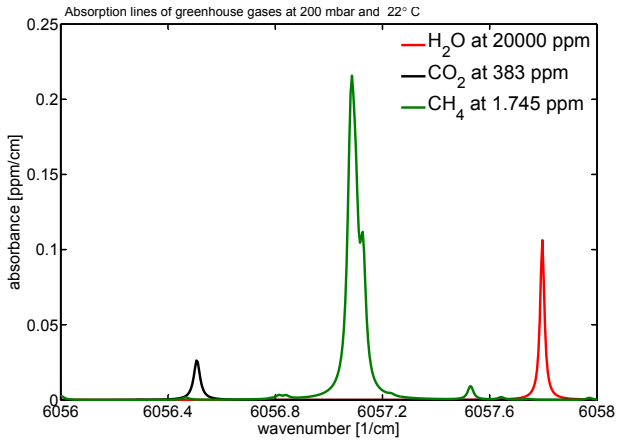

Figure 4.1: *Calculated Doppler profiles for the CH_4 and H_2O absorption lines which are measured by the spectrometer and a neighboring absorption line of CO_2 (not the one which is measured by the first laser). The profiles are calculated for a cavity pressure of 200 mbar and a temperature of 45° C. Data is extracted from the HITRAN database (David Balslev-Clausen, personal communication 2010).*

Polarization maintaining optical fibers are used to direct the laser light to different places in the spectrometer e.g. from the two lasers to an optical switch which alternately directs one of the the two laser beams to a wavelength monitor. Here, a small window angeled at 45° picks up a small amount of laser power for wavelength measurement[3], but lets most of the laser beam pass. Wavelengths (frequency) can be measured over a range of 100 nm (3 GHz) with a relative accuracy[4] of 0.3 MHz (in wavelength???) and a precision[5] of approximately 1 MHz (in wavelength???) (1σ).

Precision and accuracy are a few orders of magnitude smaller than a typical spectral line width of the absorption features (ca. 1 GHz). Thus, CRD time can be measured for several precisely known wavelengths within a single absorption feature (cf. Fig. 3.1). In that way, the spectrometer can determine the exact shape of the absorption feature and precise concentration measurements in the ppbv level are possible. From the wavelength monitor a feedback is sent to the laser control electronics for wavelength fine-tuning.

After the wavelength monitor the laser beam is directed into the three-mirror ring cavity where it bounces between the mirrors with an average path length of 10 km (empty CRD

[3]Wavelength measurements are crucial since calculation of the wavelength from the laser current is not possible with sufficient precision. This is a consequence of the unknown relationship between laser drive current and wavelength which varies from laser to laser and is, furthermore, subject to drift over time.

[4]Relative accuracy is defined as the repeatability of the difference of the wavelength measurement between two spectral points separated by ca. 1 GHz (the width of a typical absorption line at 222 mbar cavity pressure) during a spectral scan.

[5]Precision is defined as the repeatability of the wavelength measurement a single spectral point.

time of 40 μs). The length of the cavity is adjusted via a piezoelectric transducer (hereafter PZT) until mode matching[6] between laser frequency and cavity resonance frequency is reached. During mode matching, intensity builds up until a certain threshold intensity is reached. At that moment the laser beam is shut off. Absorption of radiation by sample molecules and empty cavity losses cause the intensity to decay exponentially as illustrated in Fig. 3.6. The exponential intensity decay is measured by a photo detector that receives the radiation that is transmitted through one of the mirrors.

In the data acquisition system of the spectrometer, CRD times are determined for several wavelengths (14 in case of CH_4) and are then used to determine the absorption line of the gas in question as exemplary shown in Fig. 3.1. For each of those 14 wavelengths 30–40 CRD times are measured in order to obtain enough statistics to determine a mean loss for each wavelength. Then, a fit to these mean values is used to calculate the area under the absorption line and, from that, the concentration of the gas species in the sample cavity. The results are stored and displayed in real-time on an internal PC.

A special feature of the spectrometer is the high temperature and pressure stability in the sample cavity. This is crucial since the shape of any absorption line depends on both temperature and pressure. In the following we describe briefly how the NIR-CRDS controls these quantities.

- **Pressure control:** Pressure measurements are carried out by a high-linearity pressure transducer. A feedback from the system computer communicates with two proportional-differential-controlled valves (hereafter PD, electronic proportional control valve, model EPCA28SSVXAA, Porter Instrument Company Inc.) which keep the pressure in the sample cavity constant by controlling the gas flow. One valve is located at the gas inlet and the other at the outlet of the cavity as shown in Fig. 4.2. Default pressure in the cavity is 222 mbar and maintained with a precision of 0.07 mbar (1σ). The volume of the cavity is 33 cm^3 whereas the effective volume is only 7 cm^3, due to the low cavity pressure.

- **Temperature control:** Passive temperature stabilization is achieved by layers of insulating material surrounding the two compartments which contain the sample cavity and the two lasers. Additionally, a combination of a thermal sensor and solid-state heating system controls the temperature actively. The precision of this temperature stabilization is $\pm$20 mK.

The cavity itself is protected against contamination by two filters (In-line Gas Filter, model WG2FT1SS2, Entegris Inc.) that are installed in the upstream gas tubing. Additionally, a check valve (Tubing check valve, model TVBSSTF.125SSNF, Check-All Valve Company) is installed downstream of the cavity and prevents backwards flow into the cavity. Furthermore, a pressure relief valve (SS Poppet Check Valve, model SS-4C-1,

[6]Mode matching is defined as "the precise spatial matching of the electric field distributions of laser beams and resonator modes" [52]. In other words: During mode matching the path length l of the laser beam inside the cavity is a multiple of the wavelengths of the laser light and, thus, the numerous beams that bounce between the mirrors interfere constructively and intensity builds up.

cracking pressure 70 mbar, Swagelok Company) opens when the cavity pressure exceeds ambient pressure by more than 70 mbar and protects the cavity from high pressures at which condensation of water vapor on the mirrors could disturb the measurements.

Table 4.1: *Specifications of the NIR-CRDS.*

Specification	$CH_4/CO_2/H_2O$ analyzer
Precision (5 sec/5 min, 1σ):	
CH_4	<1 ppbv/<0.7 ppbv
CO_2	<200 ppbv/<50 ppbv
H_2O	100 ppmv/50 ppmv
Drift (over 24 hours/1 month, peak-to-peak, 50 minute average):	
CH_4	1 ppbv/3ppbv
CO_2	150 ppbv/500 ppbv
Range:	
CH_4	0–20 ppmv (precision and drift guaranteed for 1–3 ppmv)
CO_2	0–1000 ppmv (precision and drift guaranteed for 300–500 ppmv)
H_2O	0–100% relative humidity
Measurement interval:	∼5 seconds
Sensitivity (noise-equivalent absorption[7]):	$1.6 \cdot 10^{-11}$ $cm^{-1}/Hz^{1/2}$

[7]In the field of laser-spectroscopy one usually characterizes the sensitivity of a spectrometer by the noise-equivalent absorption (NEA) [53, 54] given by

$$\mathrm{NEA} = \sqrt{\frac{2}{f_{\mathrm{RD}}}}\frac{\sigma_\tau}{c\bar{\tau}^2}, \tag{4.1}$$

with ring-down acquisition rate f_{RD}, standard deviation σ_τ and mean value $\bar{\tau}^2$. For the NIR-CRDS one finds $f_{\mathrm{RD}} = 100$ Hz, $\sigma_\tau = 5.43 \cdot 10^{-9}$ s and $\bar{\tau}^2 = 40$ μs. This yields a NEA of $1.6 \cdot 10^{-11}\mathrm{cm}^{-1}/\mathrm{Hz}^{1/2}$ which means that it is possible to distinguish an absorption coefficient of $1.6 \cdot 10^{-11}$ cm^{-1} from empty cavity losses during a one-second measurement interval with one sigma certainty.

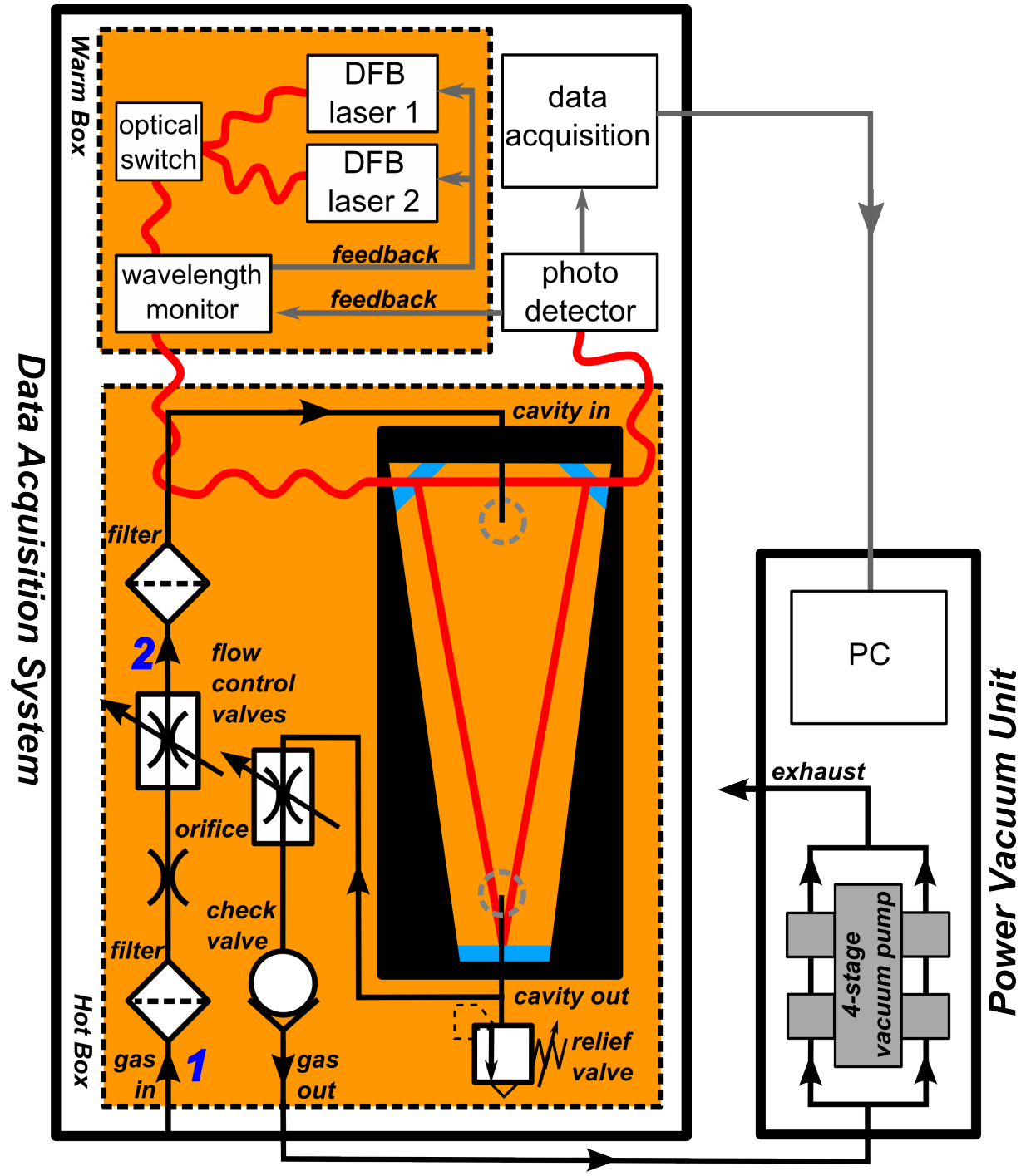

Figure 4.2: *The Picarro $CH_4/CO_2/H_2O$ analyzer. The way of the laser beam is marked by red lines which are wiggled whenever optical fibers are used. The gas stream is marked by solid black lines. Positions of installations of the oxygen sensor are indicated with 1 and 2, respectively.*

4.1.1 Calibration of the $CH_4/CO_2/H_2O$ analyzer

The CH_4 and CO_2 measurement of the NIR-CRDS is calibrated with the use of three full air standard gases (National Oceanic and Atmospheric Administration, USA). The composition of these gases is listed in Table 4.2. Calibration curves are shown in Fig. 4.3 and Fig. 4.4.

The data acquisition software of the spectrometer uses a configuration file at startup, which was updated with slopes and axis intercepts of the calibration curves. The calibration curves show the highly linear relation between the concentration calculated from cavity ring-down time measurements and the true concentration of CH_4 and CO_2, respectively.

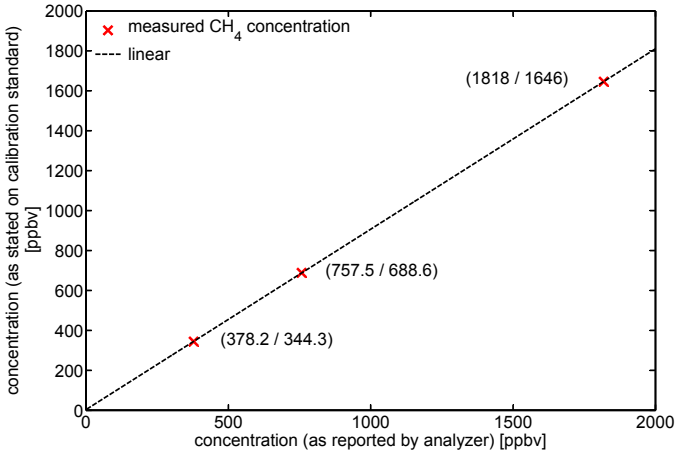

Figure 4.3: *Calibration curve for the CH_4 measurements of the NIR-CRDS. Each of the three standard gases has been measured for more than ten minutes.*

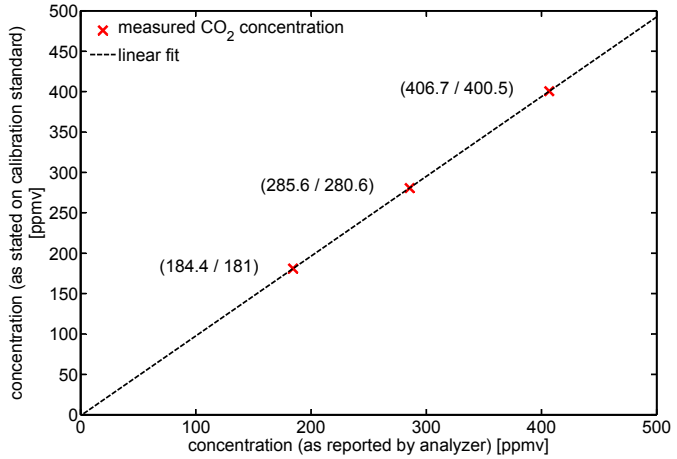

Figure 4.4: *Calibration curve for the CO_2 measurements of the NIR-CRDS. Each of the three standard gases has been measured for more than ten minutes.*

Table 4.2: *Full air standard gases from NOAA used for calibration.*

Name	Material	CH_4 conc.	CO_2 conc.
CA08274	Air	344.3 ppb	181.04 ppm
CA08280	Air	688.6 ppb	280.60 ppm
CA08292	Air	1646.2 ppb	400.53 ppm

4.2 Ocean Optics O_2 sensor

The oxygen sensor mainly consists of a probe (FOSPOR-R probe, Ocean Optics Inc.) and a spectrometer (Multi Frequency Phase Fluorometer, Ocean Optics Inc.). An optical fiber carries excitation light from a blue LED (wavelength of ca. 475 nm) towards the probe which can be placed at several places in our system due to its small dimensions (1.587 mm outer diameter, 152.4 mm length) as shown in Fig. 4.5.

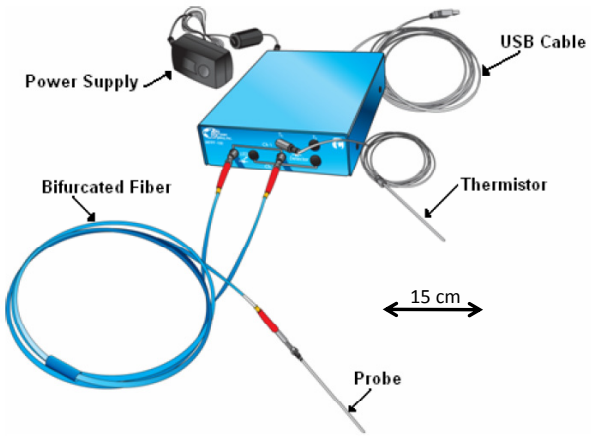

Figure 4.5: *The system for measurements of partial pressure of O_2: Excitation light is sent from the Multi Frequency Phase Fluorometer (blue box) via a bifurcated optical fiber towards the probe. Partial pressure of O_2 is measured at the tip of the probe which is coated with platinum-phorphyrin [55].*

The tip of the probe is coated with a fluorophore (platinum-porphyrin) which is embedded in a polymer network (sol-gel matrix). When the platinum-porphyrin gets excited by the light from the LED light it begins to fluoresce at a wavelength of ca. 600 nm. Fluorescence is collected by the probe and carried via an optical fiber to the spectrometer where the lifetime of fluorescence is measured [56]. More technical details of the OS sensor can be found in Table 4.3.

When O_2 molecules diffuse into the sol-gel matrix, they attenuate the fluorescence of the platinum-phorpyrin in a process called dynamical fluorescence quenching. Here, quencher molecules (O_2) collide with excited fluorophore molecules and excitation energy is transfered from the fluorophore to the quencher in a non-radiative process. The energy is finally transformed into heat and the quenching process is completely irreversible. The

degree of quenching is related to the partial pressure of quenchers (O_2 molecules) above the tip of the probe.

The calibration of the OS which relates the measured fluorescence lifetime to the partial pressure of O_2 in the gas stream is described in Section 4.2.1. For this purpose lifetimes of fluorescence are measured for a range of known partial pressures and are used to create a calibration curve.

Normally the OS is calibrated with known O_2 concentrations and the use of the Stern-Volmer equation (see below). This cannot be done since the necessary O_2 standard gases are not available in our laboratories.

Table 4.3: *Specifications of the FOSPOR–R sensor coating [56].*

Specification	FOSPOR–R probe
Accuracy (0–20% O_2, 0–50°C):	5% of reading
Response time of probe:	$\sim$ 1 second
Dynamic range of O_2 gas (at one atm):	0–100% (mole percent), 0–760 mm Hg partial pressure
Stability O_2 gas (at one atm):	Drift $\sim$ 0.0002% O_2 per hour at low O_2; Drift $\sim$ 0.015% O_2 per hour air
Resolution of O_2 gas (at one atm):	0.005% at room temperature
Lowest detectable limit of O_2 gas (at one atm):	0.005% (0.04 mm Hg)
Temperature range:	0–60°C

For the sake of completeness and understanding of the theory of measurement the Stern-Volmer equation for dynamical fluorescence quenching is derived in the following paragraphs. It relates the lifetime of fluorescence to the partial pressure of quencher molecules [57].

Let A and A^* denote the ground and excited state of the fluorophore, respectively. If no fluorescence quenchers are present at the tip of the probe, A^* can return to the ground state by fluorescence

$$A^* \xrightarrow{k_1} A + h\nu \tag{4.2}$$

and by non-radiative decay

$$A^* \xrightarrow{k_2} A, \tag{4.3}$$

with the rate constants of the two processes k_1 and k_2, respectively. Non-radiative processes in the absence of quenchers described by Eq. (4.3) are down-hill energy paths which

involve many intermediate energy states. The rate equation for the concentration of excited fluorophores $[A^*]$ is then given by

$$\frac{d[A^*]}{dt} = -k_1[A^*] - k_2[A^*] = -(k_1 + k_2)[A^*]. \tag{4.4}$$

With the boundary condition $[A^*](t = 0) = [A^*]_0$ and rearrangment of Eq. (4.4) one obtains

$$[A^*](t) = [A^*]_0 e^{-(k_1+k_2)t}, \tag{4.5}$$

which shows that the fluorescence decays exponentially in the absence of quencher molecules. The decay can be quantified by the fluorescence lifetime T_0 which is the time it takes for the fluorescence to decay to 1/e of its initial value:

$$T_0 = \frac{1}{k_1 + k_2}. \tag{4.6}$$

If fluorescence quenchers are present at the tip of the probe, A^* can decay to the ground state by a third process described as

$$A^* + Q \xrightarrow{k_q} A, \tag{4.7}$$

with the bimolecular quenching rate constant k_q. The rate Eq. (4.4) becomes

$$\frac{d[A^*]}{dt} = -(k_1 + k_2 + k_q[Q])[A^*]. \tag{4.8}$$

Here one assumes that the concentration of quenchers $[Q]$ is orders of magnitude larger than $[A^*]$, i.e. $[Q] \gg [A^*]$ which allows to treat $[Q]$ as a constant. Integration of Eq. (4.8) and use of the earlier described boundary condition yields

$$[A^*](t) = [A^*]_0 e^{-(k_1+k_2+k_q[Q])t}. \tag{4.9}$$

As a consequence of the presence of quencher molecules the decay is faster but still exponential. The fluorescence lifetime is given by

$$T = \frac{1}{k_1 + k_2 + k_q[Q]}. \tag{4.10}$$

In order to isolate the quenching effect one needs to measure fluorescence decay curves for a range of known quencher concentration including $[Q] = 0$. Then, the lifetime of fluorescence for each quencher concentration can be obtained by exponential fits through the measured decay curves. Combining Eqs. (4.6) and (4.10) yields the Stern-Volmer equation

$$\frac{T_0}{T} = 1 + k_q T_0[Q], \tag{4.11}$$

which shows us that a plot of T_0/T versus $[Q]$ should be linear. The slope can be measured to obtain the bimolecular quenching rate constant k_q.

4.2.1 Calibration of the O_2 sensor

To obtain valuable information from the OS one needs to know the exact relationship between the measured lifetime and the partial pressure of O_2. The OS cannot be calibrated with the use of the Stern-Volmer equation as described in Section 4.2.1. Instead, the calibration is realized by directly changing the pressure at the tip of the probe of the OS, thereby changing the partial pressure of O_2 as well.

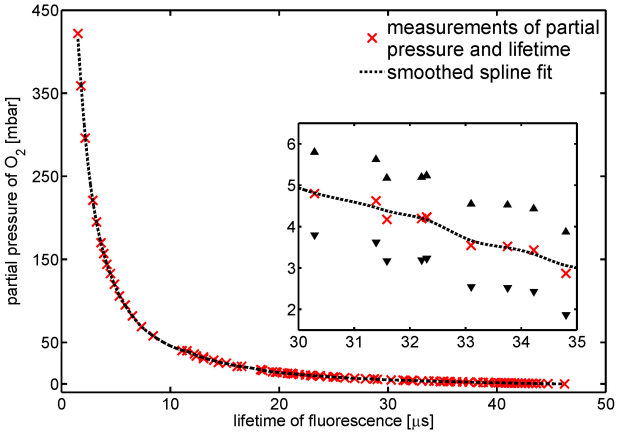

Figure 4.6: *Calibration curve which relates the measurements from the OS (lifetime of fluorescence at tip of probe) to partial pressure of O_2. The dashed black line shows a smoothed spline fit. Temperature at the tip of the probe is 45° C. The uncertainty of the pressure measurement is ±1 mbar shown as black triangles in the insert of the figure. The uncertainty of the lifetime measurements is 0.013 µs and to small to be shown (cf. Appendix C).*

To cover a wide range of partial pressures pure O_2 gas as well as ambient air (for which a constant O_2 concentration of 20.95% is assumed) are used for calibration. The OS is installed close to the cavity of the NIR-CRDS as sketched in Fig. 6.1, and by changing the cavity pressure of the NIR-CRDS the pressure at the OS is varied as well.

However, the pressure at the OS differs slightly from the pressure in the cavity due to the filter that is located between the two and acts as a flow restriction. To measure the correct pressure at the OS a pressure sensor (Piezoresistive Pressure Transmitter, Keller AG für Druckmesstechnik) is installed just upstream of the OS. Cavity pressure can easily be changed by adjusting the opening of the inlet and outlet valve of the cavity (see e.g. Fig. 4.2).

The results of the calibrations are shown in Fig. 4.6 (red crosses) together with a smoothed spline fit to the data points (black). This spline fit is necessary since exponential functions cannot be used to fit the measurements sufficiently over the complete range of partial pressures. The exponential behavior predicted from the theory cannot be confirmed by measurements.

The black triangles in the insert of Fig. 4.6 indicate the most pessimistic uncertainty estimate, i.e. here an uncertainty of ±1 mbar is assumed for the pressure measurement (the instrumental uncertainty of the pressure sensor). The uncertainty of the lifetime

measurement is 0.013 μs and to small to be shown (cf. Appendix C).

For further error propagation calculations as described in Appendix C the uncertainty for the partial pressure of O_2 is assumed to be ± 1 mbar. Thus, for the partial pressure of air, p_{AIR}, the uncertainty is ± 4.8 mbar (scaled by 1/0.2095).

4.3 Valco microvolume thermal conductivity detector

The Thermal Conductivity Detector consists of a detector cell and a controller unit (Valco Microvolume Thermal Conductivity Detector, Model TCD2, Valco Instruments Co. Inc.). The detector cell contains two columns of small volume for sample or reference gases. Each of these columns is heated by a Nickel–Iron filament and kept at constant temperature (± 0.02°C). Heat is lost continuously to the surroundings of the filament including the column and the gas stream. Schematics of the TCD and a list of specifications are shown in Fig. 4.7 and Table 4.4, respectively.

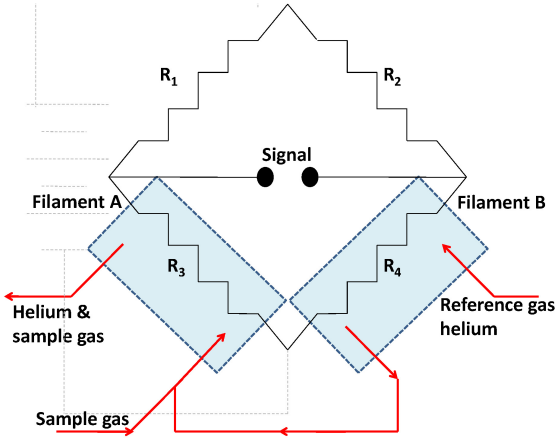

Figure 4.7: *The principle behind the Thermal Conductivity Detector. A Wheatstone-bridge senses the change in current necessary to keep the filaments at a constant temperature [58]. The gas flow through the reference and sample columns is indicated with red arrows.*

The TCD is usually connected downstream of a gas chromatograph where it measures different gas species when they elute from the column of the gas chromatograph. Then, the amperemeter in the controller measures the amount of current which is necessary to maintain a constant filament temperature while the eluted gases of varying thermal conductivity pass the column. The amount of current is directly proportional to the concentration of the gas in question.

The two columns of the TCD can be used independently or in reference mode. For the latter a reference gas is flushed through the reference column and mixed with the sample before it enters the sample column. In that way one minimizes effects like column bleed (background signal generated by the column stationary phase) and temperature

programming where the columns have to be baked to elute compounds that stick to the walls.

For our purposes the reference mode is the only option since we do not separate the compounds with a gas chromatograph beforehand. The mixture of extracted atmospheric air and helium which we receive from the CFA system is directly flushed together with the reference gas of the TCD through the sample column as indicated by the red lines in Fig. 4.7. The reference gas is chosen to be helium and, in that way, it is possible to measure the concentration of atmospheric air in this twice helium-diluted gas stream by comparing the signals from reference and sample column.

Table 4.4: *Specifications of the TCD [59].*

Specification	TCD
Ouput:	0–1 mV full scale attenuated and 0–10 V full scale unattenuated
Linear range:	1 ng to 3 μg n-butane
Minimum detectable quantity:	approximately 50 pg n-butane
Time constant:	$<$ 150 ms
Thermal stability:	$\pm$0.02°C
Maximum temperature:	300°C
Ambient temperature range for operation:	0–60°C
Flow range:	0.5–10 ml/min

Chapter 5

Preparations for the 2009 field season

This chapter present the preparative experiments for the 2009 NEEM field season. For practical reason all sections that deal with field season preparations are combined in this chapter.

During field experiments the CRDS system[1] is coupled to the University of Bern CFA system. Section 5.1 describes in detail how the CRDS system is connected to the CFA.

Sections 5.2 and 5.3 introduce the problem of sample dilution which is unavoidable during field measurements.

The sample dilution makes a measurement of total air content necessary. For this purpose, an oxygen sensor and a thermal conductivity detector are tested. Section 5.4 presents a full report of an experiment that directly compares the performances of TCD and OS. The results from this performance test lead to adjustments of the experimental setup of the OS. A performance test of the changed OS system alone is presented in Section 5.5. The results of both tests are summarized in section 5.6.

5.1 Connecting the CRDS system to the CFA

During field experiments the CRDS system for measuring CH_4 concentration from ice cores is connected to the University of Bern CFA system. This CFA system already includes a method for semi-continuous measurements of CH_4 concentrations which is based on gas chromatography [14] (cf. Section 1.3). Thus, the sample gas needs to be shared between the two systems. The following paragraphs describe the experimental setup of CFA during the 2009 field season and how the CRDS system is connected.

A sketch of the experimental setup is shown in Fig.5.1. During a CFA run an ice core stick (3 x 3 cm) is melted at a rate of approximately 3.5 cm/min. The melt water stream is pumped into a debubbler where the sample is separated into a water stream for chemical analysis and a water/gas stream for CH_4 concentration measurements. Gases are continuously extracted from the water/gas stream via a hydrophobic membrane. The

[1]Nomenclature: "CRDS system" refers to the complete system for measuring CH_4 concentrations from ice cores. It includes the NIR-CRDS, the TCD, the OS and the gas extraction line.

extracted gases are then forwarded to a 6-port valve that distributes the sample between the two systems for measuring CH_4 concentrations. A more detailed description of the experimental setup in the field can be found in Chapter 6 where measurements from the 2009 field season are presented.

Combining the CRDS system and the CFA gas chromatography-based system is possible because of the measurement routine of the latter. Here, the sample gas is accumulated over one minute, injected into the GC and finally measured for three minutes. During these three minutes of measurement the sample gas was supposed to leave the system unmeasured. With the CRDS system connected, this sample gas can be measured as well. The 6-port valve alternately sends sample to the gas chromatography-based system (for one minute) and to the CRDS system (for three minutes). When the CRDS system does not receive sample, a stream of helium is used to maintain flow through the cavity of the spectrometer.

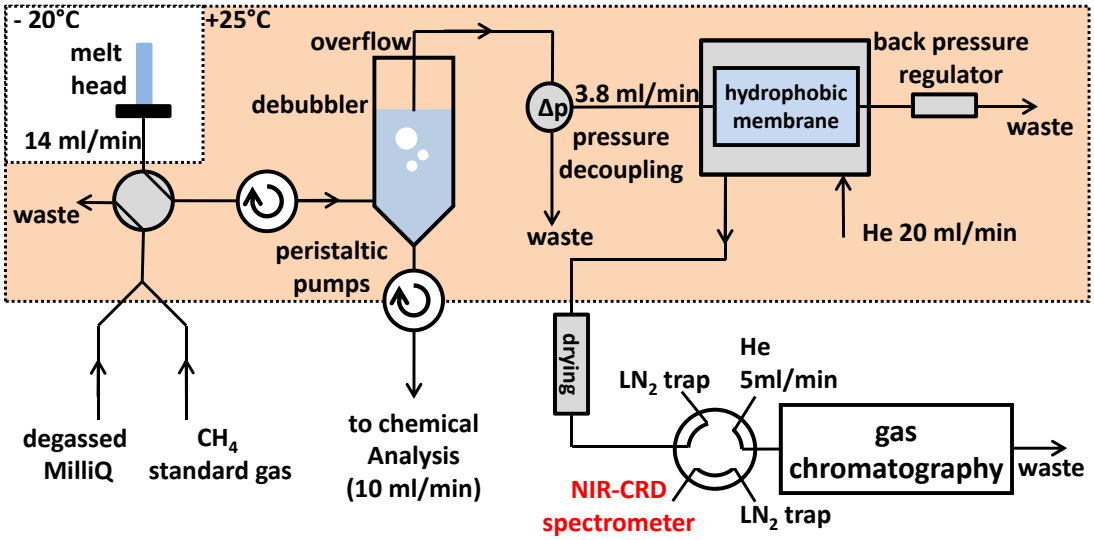

Figure 5.1: *The experimental setup for CH_4 concentration measurements coupled to the CFA system from the University of Bern (on the basis of [14]). Ice core samples are melted at a rate of 35 mm/min which results in a stream of melted sample water of ca. 14 ml/min. This stream enters the temperature-controlled gas decoupling unit where a debubbler divides the flow into a water stream (10 ml/min) for chemical analysis and an air/water stream (3.8 ml/min) for gas measurements. Gases are extracted from the air/water stream via a hydrophobic membrane. The gas is still humid but is dried with a Nafion dryer. A 6-port valve alternately sends gas to the CFA gas chromatography-based system and the CRDS system.*

5.2 The problem of sample dilution

The gas which is extracted from the melt water stream is composed solely of past atmospheric air but it is diluted two times with helium on its way through the system. First,

helium is used as a purge gas during the gas extraction process at the hydrophobic membrane and again at the 6-port valve to inject the sample into the gas chromatography system. The precise flow rates of these helium streams are unknown and cannot be measured with a precision that would allow for CH_4 concentration measurements with high precision in the ppb regime.

As a consequence, the degree of dilution of the sample/helium mixture is unknown and the information about the concentration of atmospheric air is lost. To retrieve this information it is necessary to measure the total air content in the sample/helium mixture directly or via a concentration measurement of an air component (with known atmospheric concentration). If measuring an air component, it is convenient to choose a component whose atmospheric concentration has been constant over time. This makes it possible to use the component for total air content determination along the complete core which covers more than the last 120,000 years b2k. The two main components of air, N_2 and O_2, and noble gases like krypton are well suited for this purpose.

It was decided to test two instruments that can be used to determine the total air content in the sample/helium mixture. These are a TCD which measures the concentration of air directly and an OS which measures the partial pressure of O_2. More details regarding the theory of measurement and instrument specifications of TCD and OS can be found in Sections 4.3 and 4.2, respectively. The tests of both instruments in combination with the NIR-CRDS are described later in this chapter in Sections 5.4 and 5.5, respectively.

NIR-CRDS, TCD and OS all measure different quantities. The NIR-CRDS measures the concentration of CH_4 in parts per million by unit volume (hereafter ppmv), the OS measures the lifetime of an induced fluorescence at the tip of its probe in μs and the TCD measures the difference in thermal conductivity between sample and a reference in volt. To determine the atmospheric concentration of CH_4 from two of these measurements, it is necessary to convert them to the same quantity. In the following, it is shown how to convert all measurement to partial pressure. The principle of CH_4 concentration determination is summarized in three steps and is also illustrated in Fig. 5.2.

1. The total air content of the sample/helium mixture can be measured either with the OS or the TCD. The OS measures the lifetime of the fluorescence of an excited fluorophore. Fluorescence is quenched by O_2 molecules that collide with the fluorophore. The lifetime of fluorescence is inversely proportional to partial pressure of O_2 above the probe (calibration of the OS is presented in Section 4.2.1). Since the atmospheric concentration of O_2 is assumed to be 20.95% constantly over time, one can relate the partial pressure of O_2 to the partial pressure of air by

$$p_{air} = \frac{p_{O_2}}{0.2095}, \tag{5.1}$$

   where p_{air} and p_{O_2} are the partial pressures of air and O_2, respectively.

   The TCD, on the other hand, measures the difference in current that is necessary to keep the temperature of the sample column constant compared to a helium-filled reference column. This current is linearly related to the concentration of air in

the sample/helium mixture. The TCD can be situationally calibrated with known concentrations of air or with known partial pressures of air (not shown in this thesis).

2. The NIR-CRDS uses measurements of the number of CH_4 molecules per unit volume as well as of cavity pressure and temperature in order to calculate the CH_4 concentration in the cavity in ppmv (cf. Section 3.1). With known cavity pressure, concentration can be converted to partial pressure by

$$p_{CH_4} = \frac{[CH_4]_{ppmv}}{1 \cdot 10^{-6}} \cdot p, \tag{5.2}$$

where $[CH_4]_{ppmv}$ is the concentration of CH_4 molecules in the cavity given in ppmv, p the cavity pressure and p_{CH_4} the partial pressure of CH_4.

3. With the partial pressures of air and CH_4 in the sample/helium mixture known, one can determine the concentration of CH_4 in the sample part of the sample/helium mixture using

$$[CH_4] = \frac{p_{CH_4}}{p_{air}} \cdot 10^9, \tag{5.3}$$

with the concentration of CH_4, $[CH_4]$, given in ppbv (the common unit for atmospheric CH_4 concentrations). Some corrections have to be applied to $[CH_4]$ in order to obtain the true atmospheric CH_4 concentration. The reason being processes that can occur during the gas extraction and influence the CH_4 concentration of the extracted gas stream. Examples are dissolving of CH_4 molecules in the melted ice water or incomplete gas extraction. Section 6.3 describes the calibration that is used to correct for these effects.

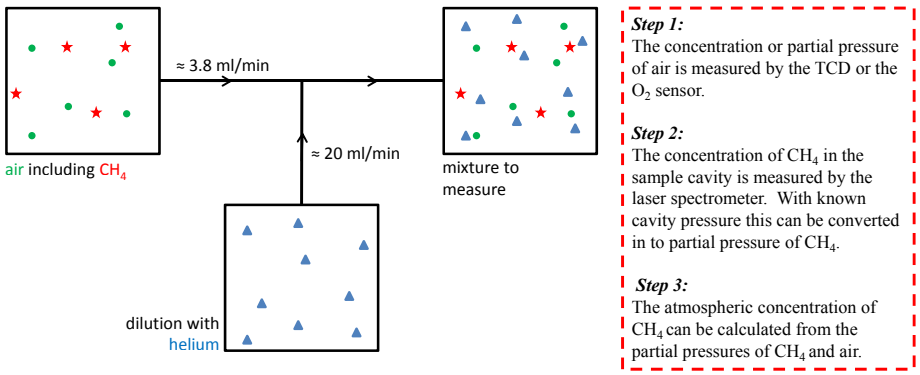

Figure 5.2: *The principle of CH_4 concentration measurement from a helium-diluted atmospheric air sample. After dilution with helium the total air content in the sample/helium mixture is unknown. It is then necessary to measure the concentration of air or the partial pressure of air in order to determine the CH_4 concentration in air.*

5.3 The order of TCD, OS and NIR-CRDS

The position of the TCD and the OS in the CRDS system with respect to the cavity of the spectrometer has a significant influence on the measurements of total air content. This section describes which position is chosen and how this effects the measurements.

Ideally, the two measurements should be as close to each other in the CRDS system as possible. Therefore, a well-suited place for the total air content measurements would be in or at least very close to the cavity of the spectrometer. In the former case the two measurements would be exactly in the same volume, at exactly the same time and under the same pressure and temperature conditions.

For the TCD this experimental setup is not possible since the sample stream has to pass the sample column of the TCD in order to be measured and the TCD itself is to large to be installed in the cavity. The small OS, on the other hand, could in theory be installed in the cavity of the spectrometer. Measurements take place at the tip of the OS's probe, a small area of approximately 4 mm^2. However, opening the cavity and installing a sensor goes along with a high risk of damaging or polluting the mirrors. Also, empty cavity losses could change in an unknown way (cf. Section 3.3).

Due to these risks and the approaching start of the field season, it was decided to take a quick and safe approach where the TCD and the OS are not installed in the cavity. Instead, the two instruments were installed upstream of spectrometer. It was already known at this point, that this choice goes along with certain disadvantages. These disadvantages are described below, together with suggestions for alternative installations.

1. **Pressure differences:** In the chosen setup where the TCD and the OS are installed upstream of the cavity, the pressure at TCD and OS is easily influenced by pressure fluctuations in the gas stream. Possible sources of pressure fluctuations are variations in the delivery rate of the pump of the spectrometer, changes in the flow rates of sample and/or helium, as well as ambient temperature fluctuations.

   The cavity of the NIR-CRDS, on the other hand, is pressure controlled and the pressure is kept at constant 222 mbar which makes this position ideal for the TCD and the OS. A third alternative, an installation of TCD and OS downstream of the NIR-CRDS, is not advisable since the pressure fluctuations created by the vacuum pump are too large. These fluctuations are buffered by the valves of the cavity and can not be measured in the cavity or upstream of it.

2. **Temperature differences:** The measurement of partial pressure of O_2 by the OS is temperature dependent and, thus, it is convenient to maintain a constant temperature at the probe of the OS. However, with the chosen installation upstream of the spectrometer, the OS is subject to ambient temperature fluctuations. In this regard, the cavity of the spectrometer and surrounding tubing are ideal places for installing the OS because the temperature is actively controlled and kept constantly at 45°C.

3. **Signal smoothing:** In principle, there are only three factors that can alter the CH_4 concentration and total air content in the sample/helium mixture. These are

fluctuations in the amount of air coming from the ice core, fluctuations in the amount of helium used for dilution and actual changes in CH_4 concentration in the sample. The latter is caused by CH_4 concentration changes in the past atmosphere and is the signal we would like to measure in the end. All these fluctuations are smoothed out on their way through the system. The reason for smoothing is dispersion along the sample transfer lines and especially in the large volumes of the system such as the debubbler or the cavity.

In the chosen setup, the TCD and the OS measure a gas stream that has been subject to less smoothing than the gas stream measured by the NIR-CRDS. The large volume of the cavity introduces additional smoothing that affects only the CH_4 concentration measurements since the TCD and the OS are installed upstream of the spectrometer. As a consequence, the calculation of the atmospheric CH_4 concentration becomes imprecise since it is based on both the less-smoothed TCD/OS and the smoothed NIR-CRDS signal (cf. Eq. 5.3). One possible solution to this problem is to simulate smoothing for the TCD and OS measurements. This trick is applied during data analyses in Sections 5.4.2 and 5.5.2. A thorough description of the simulation of smoothing effects is presented in Appendix A.

5.4 Performance test of TCD, OS & NIR-CRDS

This section presents an experiment where both the OS and the TCD are connected to the NIR-CRDS, which makes it possible to compare the performances of the OS and the TCD directly.

Both instruments have their advantages and disadvantages which need to be evaluated before deployment to the field. The OS is better suited for field deployment than the TCD due to its small size and the fact that it needs no reference gas. However, the performance of the OS under the given experimental conditions is unknown whereas the TCD is an established instrument that has been tested extensively in comparable systems in our laboratories. Disadvantages of the TCD are its relatively large size and its need for a reference gas. Thus, a direct comparison of the performance of the two instruments helps to decide which of the two instruments should be deployed to the field.

The following Section 5.4.1 describes the experimental setup of the performance test. Data analysis and results are presented and discussed in Section 5.4.2.

5.4.1 Experimental setup

A sketch of the experimental setup is shown in Fig. 5.3. Compressed technical grade dry air (Air Liquide Denmark A/S; 79 % N_2, 21 % O_2 and 2250 ppbv CH_4) is used as a sample gas which is diluted with helium in order to simulate field conditions (cf. Section 5.1). For this purpose, the sample flow (ca. 5 ml/min) is mixed with the reference gas stream of the TCD (ca. 20 ml/min). The sample flow rate can be changed by using a pressure regulator in combination with a glass capillary with an inner diameter (hereafter ID) of 250 μm. By

changing the sample flow rate, the degree of dilution can be changed and the instruments can be tested over a wide range of CH_4 concentrations.

The gas stream is measured by the three instruments in the following order: TCD, OS and finally NIR-CRDS. An open split is installed between TCD and NIR-CRDS to ensure that the spectrometer can adjust the sample flow through the cavity independent of pressure fluctuations in the sample gas stream. A small overflow of ca. 5 ml/min at the open split prevents ambient air from entering the system. A flow restriction in form of a glass capillary (250 μm ID, 30 cm long) is installed after the open split in order to reduce the flow rate through the cavity to ca. 20 ml/min as expected for field measurements. During the experiment the sample to helium ratio is changed stepwise by changing the sample flow rate.

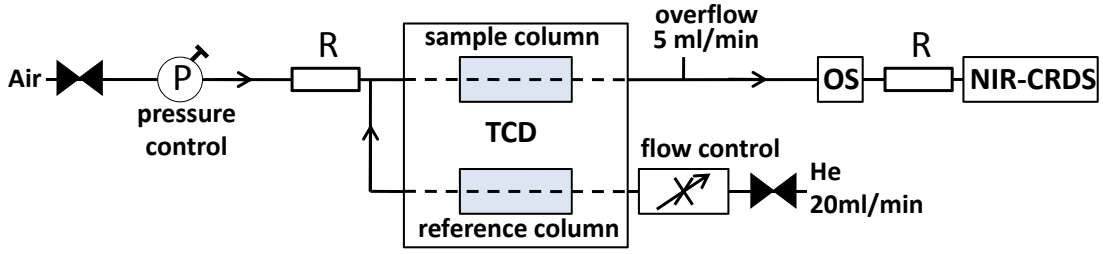

Figure 5.3: *Experimental setup for the performance test of TCD, OS and NIR-CRDS. Resistances in the figure represent glass capillaries that were used in order to reduce the flow rate through the cavity. Both capillaries have an inner diameter of 250 µm and are approximately 30 cm long. The sample flow rate was adjusted via a pressure regulator.*

5.4.2 Data analysis and results

The unmodified measurements of TCD, OS and NIR-CRDS are shown in Fig. 5.4. The left plot in the figure shows the signals of the TCD (black) and the NIR-CRDS (red). The right plot shows the signal of the OS (blue) and the NIR-CRDS (red).

Some adjustments of the signals are necessary in order to determine the CH_4 concentration of the sample with high precision. The major steps are listed below and the MATLAB source code used for data analysis can be found in Appendix E.

1. **Interpolation:** The NIR-CRDS measures CH_4 concentration in irregular time intervals (ca. every 4–5 s), whereas OS and TCD have regular measuring frequencies of 1 Hz. To make data analysis more convenient we interpolate the OS and NIR-CRDS measurements on the time scale of the TCD measurement. After interpolation each signal consists of the same number of data points and point-by-point comparison of the measurements is possible. At this point it should be emphasized that this interpolation does not improve the resolution of our measurement. The highest possible resolution is set by the measurement frequency of the spectrometer.

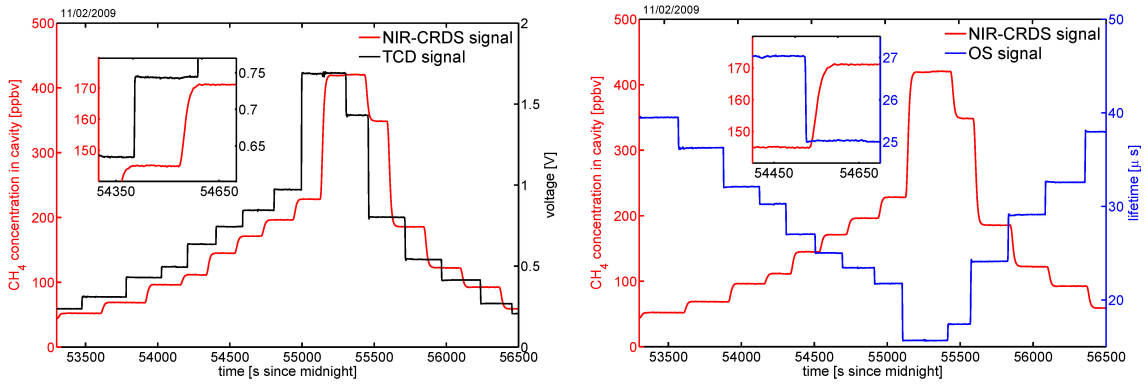

Figure 5.4: *Comparison of TCD to NIR-CRDS signal (left) and of OS to NIR-CRDS signal (right), respectively. The NIR-CRDS signal is smoothed mainly due to dispersion in the cavity. TCD and OS are installed upstream of the cavity and their signals are less smoothed. The measurements from the different instruments are out of phase. The signal from the OS (NIR-CRDS) lags ca. 131 s (143 s) behind the TCD signal. The inserts show magnifications of the responses of the instruments to a step-wise change in sample concentration.*

2. **Synchronization of the signals:** All instruments are located at different parts of the system and their signals are out of phase. Low flow rates and long distances between the instruments cause the signals from OS and NIR-CRDS to lag approximately 131 s and 143 s behind the TCD signal, respectively. OS and NIR-CRDS are installed close to each other and the phase shift between their signals is only 12 s. The signals are synchronized by visual matching.

3. **Smoothing of the signals:** TCD and OS are installed upstream of the NIR-CRDS where the signal has not been subject to dispersion in the cavity of the spectrometer. The differences between measurements from the TCD, OS and NIR-CRDS can be seen in Fig. 5.4. The TCD and the OS signals show sharp responses to step-wise changes in sample-to-helium ratio whereas responses from the NIR-CRDS are smoothed. This smoothing is a consequence of the dispersion in the cavity of the spectrometer due to a combination of large volume and low flow rate. This infers residence time in the cavity during which the gases are mixed.

   As explained in Section 5.3, a determination of the CH_4 concentration of the sample with high precision is only possible if the signals which are used for determination show the same degree of smoothing. For this purpose a discrete smoothing function $s(t)$ is convoluted with the TCD and OS signal:

$$s(t) = a \cdot e^{-\frac{t}{\tau_s}} \quad \text{with} \quad a = \left[\sum_{t=t_1}^{t_2} e^{-\frac{t}{\tau_s}} \right]^{-1}, \tag{5.4}$$

   with time t, smoothing constant τ_s and a which normalizes the smoothing function $s(t)$. The effect of this convolution on the TCD and the OS signal can be varied

by changing the smoothing constant τ_s and the length (the range of the integral) of the smoothing function. In practice, $s(t)$ is optimized by finding the two parameters which yield the highest correlation between the NIR-CRDS signal and the smoothed TCD and OS signal, respectively. A detailed description of the smoothing function can be found in Appendix A.

The resulting convoluted TCD and OS signals are shown in Fig. 5.5. The parameters of the optimized smoothing functions and the correlation between the signals are shown in Table 5.1 and are different for the TCD and the OS since the responses from these instruments are slightly different. When taking a closer look on the responses of the instruments to a step-wise change in concentration it can be seen that the OS in general reacts slower than the TCD. Therefore, the steps in the OS signal are slightly less steep than the ones in the TCD signal.

	TCD & NIR CRDS	OS & NIR-CRDS
correlation coefficient	0.999348	-0.931325
smoothing constant [s]	693	636
length of smoothing function [s]	35	17

Table 5.1: *Optimal smoothing function parameters and correlation: By optimizing the length and the smoothing constant τ_s of the smoothing function one finds the optimal correlation between NIR-CRDS signal and the convoluted signal of OS and TCD, respectively. The correlation between NIR-CRDS and OS signals is negative since the signal of the OS is inversely proportional to the partial pressure of O_2.*

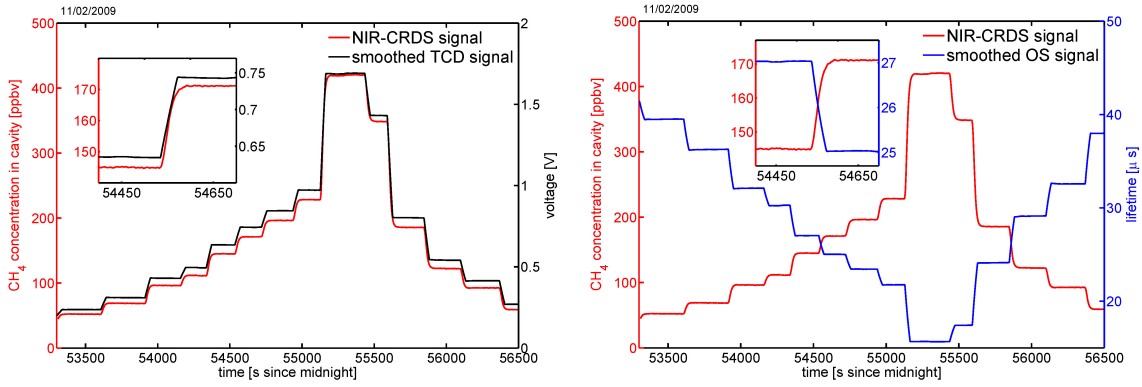

Figure 5.5: *The synchronized and convoluted signals of TCD (left) and OS (right) compared to the NIR-CRDS signal. The inserts show magnifications of the convoluted and NIR-CRDS responses to a step-wise change in sample concentration.*

4. **Conversion to partial pressure and determination of the CH_4 concentration:** All instruments measure different quantities. In order to determine the concentration of CH_4 in the sample from two of those measurements it was decided to

convert all measurements to partial pressures. A detailed description of this conversion and how to determine the CH_4 concentration of the sample can be found in Section 5.2.

At the time of the performance test, calibrations of the instruments were still overdue. Thus, a different approach has to be used in order to test the performance of the TCD and the OS. Instead of converting the TCD and OS measurements to the partial pressure of air, these measurements are related to the CH_4 concentration measurement of the NIR-CRDS. For this purpose, every data point of the TCD and OS measurement is assigned to a certain CH_4 measurement by the NIR-CRDS. Then, the relation between the signals is described by a polynomial fit of third order with the constants a, b, c and d:

$$[CH_4]_{fit} = a \cdot x^3 + b \cdot x^2 + c \cdot x + d, \tag{5.5}$$

where x represents the conductivity measurement of the TCD or the lifetime measurement of the OS, respectively. The fits to the relations are shown in Fig. 5.6 where the blue crosses show the NIR-CRDS measurements plotted against the measurements of the TCD (left) and OS (right), respectively. Then, the polynomial fits $[CH_4]_{\text{fit}}$ are used in combination with the measured CH_4 concentrations to determine the CH_4 concentration of the sample gas by

$$[CH_4] = \frac{[CH_4]_{\text{measured}}}{[CH_4]_{\text{fit}}} \cdot [CH_4]_{\text{bottle}}, \tag{5.6}$$

where $[CH_4]_{\text{measured}}$ is the measured CH_4 concentration and $[CH_4]_{\text{bottle}}$ is the true CH_4 concentration of the sample air.

The fraction in Eq. 5.6 is multiplied with the known CH_4 concentration of the dry air $[CH_4]_{\text{bottle}}$. In this way, the calculated CH_4 concentration is scaled to the true concentration and the calculation becomes a measure of the precision of the method. When the fitted CH_4 concentration matches the measured one, the fraction of the two becomes one and the calculated CH_4 concentration equals the true value. However, when the fitted CH_4 concentration differs from the measured one, the calculated CH_4 concentration differs from the true value.

The measurements of the NIR-CRDS are known to be very precise ($\pm$0.5 ppbv). Thus, discrepancies between fitted and measured values stem from (1) uncertainties in the measurements by the TCD or the OS or (2) from insufficient smoothing of the OS and TCD signal, respectively.

A major drawback of this approach is that no information about the accuracy of the method can be obtained since the instruments have not been calibrated for these preparative tests and the results are simply scaled to the right value. However, the the precision of the results of calculated CH_4 concentrations can be compared to evaluate the performance of TCD and OS. Fig. 5.7 shows the calculated CH_4 concentrations based on TCD (left)

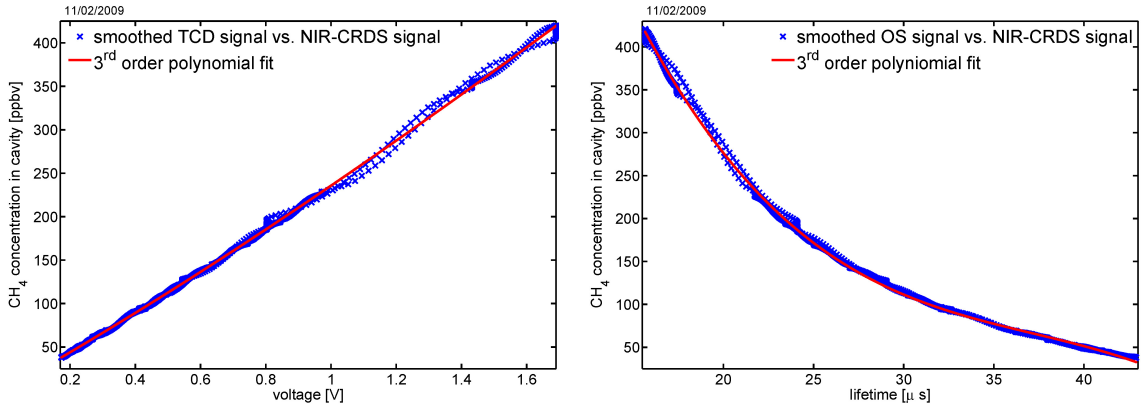

Figure 5.6: *Blue crosses show the relation between the signal of the NIR-CRDS and the smoothed signals of the TCD (left) and the OS (right), respectively. The relation is fitted by a 3rd order polynomial (solid red line).*

and on OS (right). Spikes in the results are a consequence of the step-wise changes in concentration. During these steep changes, small discrepancies between the two signals become significant. Even with the use of the smoothing function it is not possible to correlate the two signals well enough to correct for these discrepancies. Fortunately, such rapid concentration changes are not expected to occur during measurements of ice cores since past atmospheric CH_4 concentrations did not change that fast.

The insert in the left plot of Fig. 5.7 magnifies a part of the results based on TCD measurements to show the high precision of the method during stable parts of the measurement. The precision is better than ± 10 ppbv for the complete range of measured concentrations. For CH_4 concentrations higher than 200 ppbv, the precision is even better than ± 5 ppbv.

The right plot of Fig. 5.7 shows the result which is based on the measurements from the OS. At first sight this result looks much worse than the one obtained from the TCD's measurement. Calculated values differ significantly from the true CH_4 concentration. These deviations are attributed to an insufficient temperature and pressure stabilization of the OS. One can distinguish between two different influences:

1. The results jump between different steps in concentration but seem to be stable as long as the concentration is not changed. The reason for these jumps are most likely pressure changes in the gas stream. Each time the flow rate of the sample gas is adjusted via the pressure regulator, the pressure in the sample stream is changed too. As a consequence, the inlet valve of the spectrometer reacts and changes its resistance in order to keep the cavity pressure at constantly at 222 mbar. A change in resistance at the inlet valve also affects the pressure at the pressure-sensitive OS which sits upstream from the valve. It seems that the open split cannot buffer these pressure changes sufficiently.

2. On top of the jumps between steps, there is a long-term drift in the results which

is most likely caused by a combination of ambient temperature and pressure fluctuations. The probe of the OS is influenced by ambient temperature since we do not control the temperature actively during this performance test. Ambient pressure changes affect the measurements since the system is open to atmosphere at the open split.

Two important conclusions can be drawn from this result.

1. Temperature and pressure stabilization or at least precise measurement of these quantities is mandatory when using the OS for calculations of the CH_4 concentration of the sample.

2. The precision of the method is promising for both the TCD and the OS approach. If one neglects the jumps and long-term fluctuations in the OS-based calculation, the precision of the calculation is still as good as the one based on the TCD as the insert in the right plot of Fig. 5.7 shows.

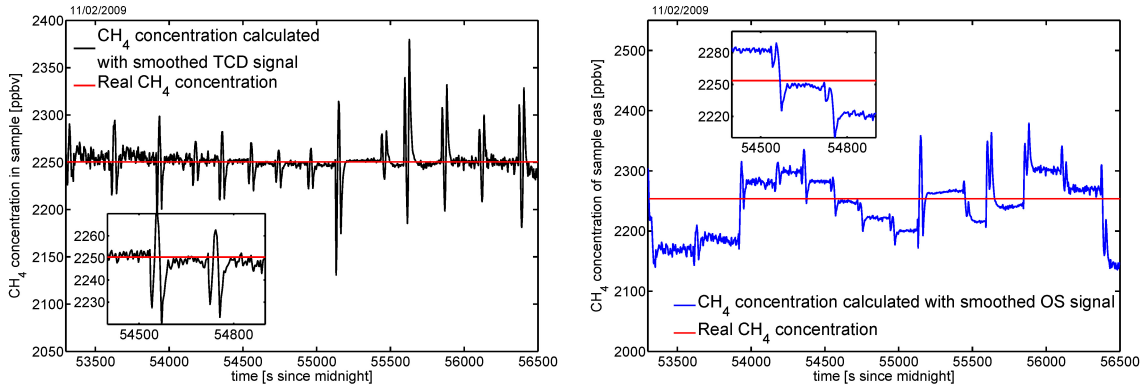

Figure 5.7: *The calculated CH_4 concentration of the sample gas. The spikes are a consequence of rapid changes in CH_4 concentration which do not occur during measurements of air extracted from ice cores. Left: Calculation based on TCD measurements. When neglecting the spikes the precision of the method is better than ± 10 ppbv. Right: Calculation based on OS measurements. The calculated values differ significantly from the true CH_4 concentration of the sample gas due to pressure and temperature fluctuations at the probe of the OS. When neglecting spikes and focusing on stable parts of the calculation the precision of the measurement is comparable to the TCD experiment. The inserts show magnifications of parts of the results.*

5.5 Performance test of OS & NIR-CRDS

The results from the performance test of the OS and the TCD described in Section 5.4 look promising. However, the sensitivity of the OS to temperature and pressure fluctuations introduces large uncertainties in the determination of the sample CH_4 concentration (right plot in Fig. 5.7). This section describes an experiment which tests the OS thoroughly under more stable conditions and without the TCD. The experimental setup is described in Section 5.5.1 and both data analysis and results are presented in Section 5.5.2.

5.5.1 Experimental setup

In order to avoid temperature fluctuations at the probe of the OS, the probe is installed in the temperature stabilized compartment of the NIR-CRDS. This compartment includes the cavity but also parts of the tubing that lead the gas stream into and out of the cavity. It was decided to install the OS in the temperature stabilized tubing upstream from the cavity where two ultrahigh-purity gas filters protect the cavity mirrors from pollution. Hereby, the risk of polluting the mirrors during installation of the OS is avoided. For this purpose, the probe of the OS (outer diameter of 1.6 mm) is slid through a 1/8 in. tee piece and through the gas inlet of the spectrometer with the tip of the probe resting upstream from the first filter. A detailed sketch of the OS installation is shown in Fig. 5.8. For comparison the position of the installation is indicated in a sketch of the complete spectrometer shown in Fig. 4.2.

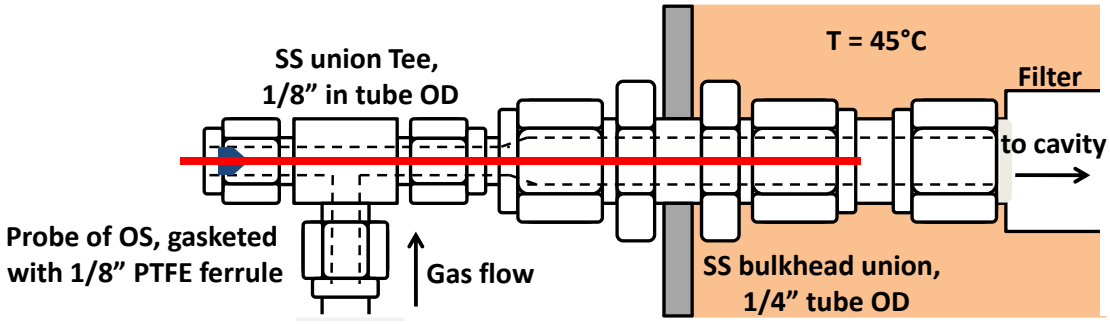

Figure 5.8: *Installation of OS: The probe of the OS (red) is slid through a 1/8 in. tee piece and a 1/4 in. bulkhead union into the temperature stabilized compartment of the spectrometer. Here, the tip of the probe rests upstream from a filter that protects the cavity mirrors from pollution. The connection of probe and tee is sealed with a PTFE 1/8 in. ferrule (blue).*

Achieving stable pressure at the probe of the OS is more complicated. The composition of the sample/helium mixture is altered with a pressure regulator and each adjustment goes along with a change in pressure in the gas stream. The cavity of the spectrometer is separated from these pressure fluctuations by two electronically controlled PD-valves as shown in Fig. 4.2. An installation of the OS so close to the cavity will guarantee stable pressure but carries the risk of mirror pollution. At this point it was decided not to install the OS so close to the cavity for the following reasons:

- High pressure fluctuations in the gas stream are not expected during measurements in the field. Variations in the amount of extracted gas coming from the melt head are expected to be small and to be compensated by an open split after the debubbler that decouples the pressure in the gas extraction unit from the pressure in the systems for chemical analysis as shown in Fig. 5.1.

- The approaching field experiments should not be jeopardized by taking the risk of mirror pollution. This risk is high during an installation of the OS in the pressure stabilized parts of the tubing of the spectrometer where the cavity is not protected by a filter.

The experimental setup for the performance test of the OS is shown in Fig. 5.9. This setup does not differ much from the one used for the TCD/OS performance test described earlier and shown in Fig. 5.3. The TCD was removed and the OS was installed in the inlet of the spectrometer as described above. Furthermore, the air concentration in the air/helium mixture is changed in smaller steps thereby reducing the disturbing pressure fluctuations in the gas stream.

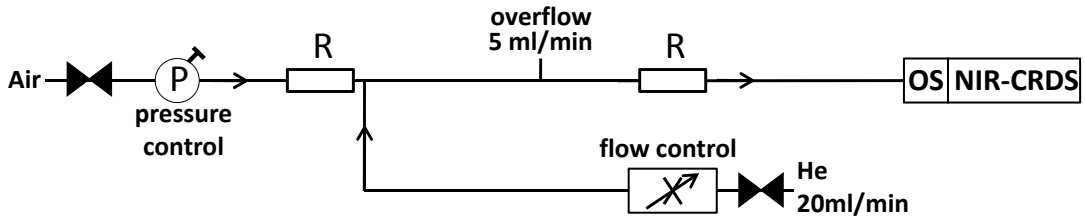

Figure 5.9: *Oxygen sensor and NIR-CRD spectrometer. Resistances in the figure represent glass capillaries that were used in order to reduce the flow rate through the cavity. Both capillaries have an inner diameter of 250 µm and are approximately 30 cm long. The sample flow rate was adjusted via a pressure regulator. The OS is installed in the temperature stabilized tubing of the spectrometer.*

5.5.2 Data analysis and results

This section presents the results from the performance test of the OS. The detailed data analyzing procedure is not presented here since it follows the same steps as the one for the TCD and OS performance test which is described in Section 5.4. Instead, the MATLAB source code for data analysis can be found in Appendix D.

The unmodified signals of the OS and the NIR-CRDS are shown in the left plot of Fig. 5.10. The OS signal precedes the NIR-CRDS signal by 10 seconds. The right plot shows the synchronized signals of the OS and the NIR-CRDS where the OS signal is smoothed using the smoothing function m (cf. Eq. 5.4). The smoothing constant and length of the smoothing function are 33 s and 29.8 s, respectively. The correlation of these

signals and a 3rd order polynomial fit are shown in the left plot of Fig. 5.11. The result of the calculation of the CH_4 concentration is shown in the right plot.

This result is much closer to the true CH_4 concentration of the sample gas than the one from the TCD and OS performance test shown on the right plot of Fig. 5.7. Again, the spikes in the result stem from step-wise changes in sample-to-helium ratio which do not occur under ice core experiments. When the spikes are neglected, the precision of the calculated CH_4 concentration is better than ± 20 ppbv.

The improvement compared to the TCD/OS performance test is attributed to the better temperature and pressure stabilization at the probe of the OS. During field experiments pressure fluctuations are expected to be smaller (no step-wise change in flow rate) and the results should improve further.

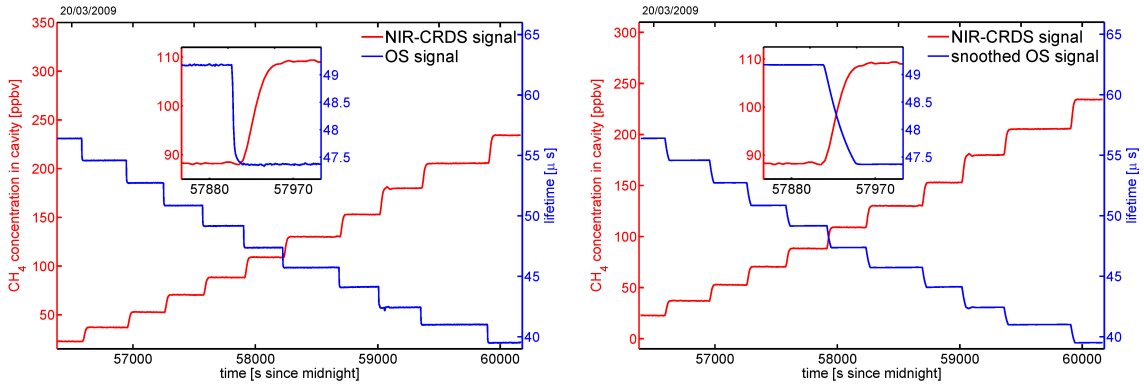

Figure 5.10: *Performance test of the OS. Left: The raw signals of the OS and the NIR-CRDS. Right: The synchronized signals of the OS and the NIR-CRDS. The signal of the OS has been convoluted with a smoothing function. The inserts show magnifications of the responses of the instruments to step-wise changes in sample concentration.*

5.6 Summary of the TCD and OS performance tests

To solve the problem of dilution by the helium carrier gas, an OS and a TCD are tested for measurements of total air content. In Section 5.4 the performances of the TCD and the OS are directly compared. The results from the TCD are excellent and the precision of the calculated CH_4 concentration is better than ± 10 ppbv. The results from the OS are promising but need improvement. The uncertainties in the calculated CH_4 concentration are attributed to an insufficient stabilization of the temperature and pressure at the OS.

Section 5.5 describes a more thorough test of the OS. For this purpose, the position of the OS is changed which improves temperature stabilization at the probe. Pressure fluctuations are reduced (but cannot be avoided completely) by adjusting the ratio of the sample-to-helium mixture more gently. As a consequence of these changes in the experimental setup, the results from this second OS performance test improve significantly. Precision of the calculated CH_4 concentration is better than ± 20 ppbv.

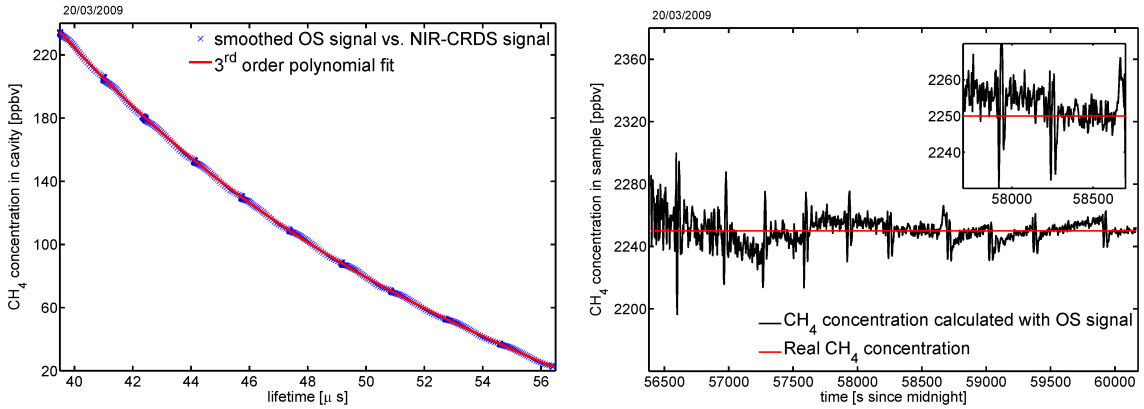

Figure 5.11: *Performance test of the OS. Left: Blue crosses show the relation between the convoluted signal of the OS and the signal of the NIR-CRDS. The relation is fitted by a 3rd order polynomial. Right: The calculated CH_4 concentration of the sample gas. The spikes are a consequence of rapid changes in CH_4 concentration which do not occur during measurements of air extracted from ice cores. Pressure fluctuations at the probe cause drifts in the result. When neglecting spikes the precision of the measurement is better than ± 20 ppbv. The insert shows as magnification of a part of the result.*

It is decided to deploy the OS to the field because of its practical advantages such as its small size and the fact that it does not require a helium reference stream. The slightly worse precision of the calculated CH_4 concentration based on the OS compared to the TCD is expected to improve during field experiments as a consequence of more stable pressure at the probe of the OS.

Chapter 6

The 2009 field season

This chapter presents the experiments from the 2009 NEEM field season. Section 6.1 includes a brief summary of the results from the preparative laboratory tests and shows how experiences from these test are used to prepare a field deployable system for on-line high resolution CH_4 concentration measurements. The experimental setup for field experiments is described in Section 6.2 where the focus is on the implementation of the NIR-CRDS system into the University of Bern CFA system. In Section 6.3 data analysis of one typical CFA run is described in detail. Finally, the complete data set from 2009 field measurements is presented and discussed in Section (6.4.

6.1 Preparing the system for field deployment

Based on results from preparative tests (cf. chapter 5) it was decided to use an oxygen sensor for total air content measurements in the field. The performance of the OS looks promising as long as pressure and temperature fluctuations can be kept low. The precision of the method when using the OS for total air content measurements is better than ± 20 ppbv over a wide range of concentrations and is expected to improve under more stable pressure and temperature conditions.

To improve temperature and pressure stability at the probe of the OS even further the position of the OS in the experimental setup is changed before the system is deployed to the field.

The NIR-CRDS itself needs stable pressure and temperature in its cavity to operate properly. Therefore, the part of the NIR-CRDS that contains the cavity is actively pressure and temperature controlled (cf. Chapter 4). In order to take advantage of this compartment, the OS is installed in the gas stream just upstream of the cavity of the spectrometer as illustrated in Fig. 6.1. For comparison, the position of installation is also indicated in the sketch of the complete spectrometer shown in Fig. 4.2. With this new installation only a gas filter lies between the OS and the cavity. This arrangement offers not only improved pressure and temperature stabilization at the tip of the probe of the OS but also makes measurements of CH_4 and O_2 partial pressure at almost the same place in the gas

stream possible. Furthermore, the system becomes very compact since both instruments are located in the box of the spectrometer.

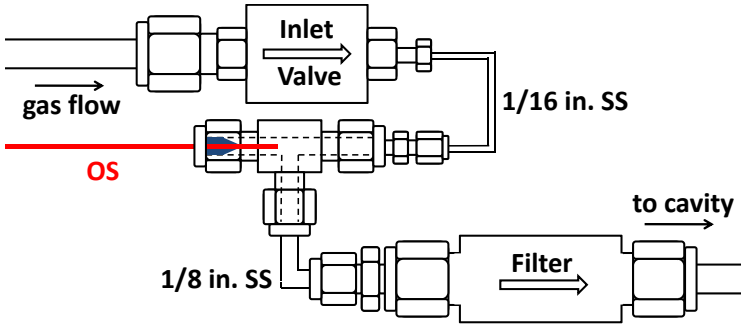

Figure 6.1: *Installation of the OS which improves both pressure and temperature stability: A 1/8 in. stainless steel (hereafter SS) tee piece is installed between inlet valve and filter. The probe of the OS (outer diameter of 1.6 mm) is slid into the tee piece and sealed with a 1/8 in. PFTE ferrule. Measurements of partial pressure of O_2 take place at the tip of the probe which is now located in the temperature and pressure stabilized compartment of the spectrometer. At this position the pressure of the gas stream is controlled and stabilized by the two valves surrounding the cavity of the spectrometer (only the inlet valve is shown here).*

6.2 The system in combination with the CFA

In the field, the CRDS system receives sample gas from the University of Bern CFA system which is installed in a warm laboratory in the underground science trench of the NEEM camp. As a consequence of a shortage of space inside the CFA laboratory, the NIR-CRDS is installed on the roof of the laboratory and is connected to the CFA via a 1/16 in. SS tube of approximately 3 m length. The CRDS system is installed in a wooden box in order to provide some protection against the cold air of the science trench (-18°C). Waste heat of the instrument is sufficient to keep a roughly constant temperature of +15°C in the wooden box.

The CFA system already has an established system for measurements of CH_4 concentration which was introduced in Section 1.3. This system consists mainly of a GC and a LN_2 trap. It has been tested successfully with ice from Talos Dome and is expected to yield a full CH_4 record of the NEEM core [14]. Thus, the CRDS system has to be connected to the CFA in a way that does not disturb the measurements of the GC system. In the following it is described how such a setup is realized in the field and how it affects the results from the CRDS system.

The experimental setup for combined CH_4 concentration measurements from the GC and the CRDS-system is shown in Fig. 5.1. In the debubbler the stream of melted sample water is separated in a water stream for chemical analysis and a gas/water stream for gas measurements. The gas/water stream (3.8 ml/min) enters the gas extraction unit where a hydrophobic polypropylene membrane (Accurel membrane, model PP Q3/2, Membrana

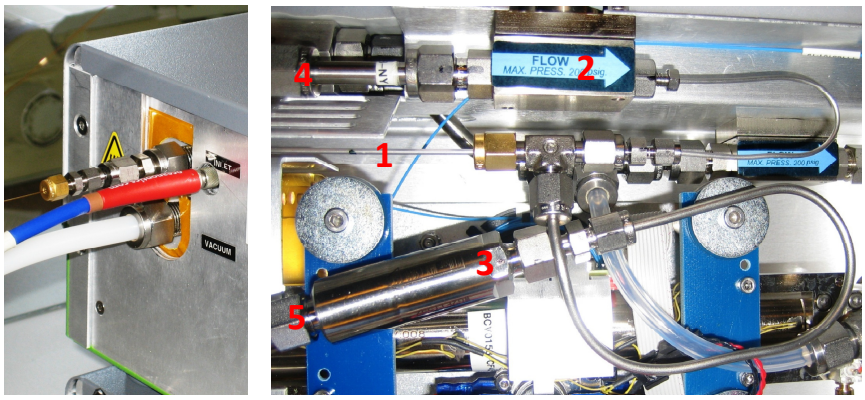

Figure 6.2: *Installation of the OS which improves both pressure and temperature stability. Left: View on the gas inlet of the NIR-CRDS. A glass capillary before the inlet reduces the flow through the analyzer. The optical fiber (blue) that carries excitation light to the probe of the OS enters the NIR-CRDS next to the gas inlet. Right: View on the installation of the OS inside the spectrometer including the OS (1), the inlet valve (2), the filter (3), the gas inlet (4) and the way towards the cavity (5).*

GmbH, Germany) is used to separate the gases from the remaining water. Helium is used as a purge gas and is swept around the hydrophobic membrane to keep the partial pressure of all air components outside the membrane low. In that way gas diffuses out of the gas/water stream through the hydrophobic membrane and into the purge flow.

Length and diameter of the membrane and pressure inside the melt water stream are adjusted in a way such that all undissolved air can leave the water stream while passing the membrane. More information can be found in Schüpbach et al. [14] where the CH_4 measurements of the GC system are described in detail. A temperature and pressure dependent fraction of CH_4 molecules is dissolved in the water stream and cannot be completely extracted at the hydrophobic membrane. This fraction of dissolved CH_4 molecules is temperature and pressure dependent. By actively keeping temperature and pressure constant in the complete gas extraction line this fraction can be kept constant too, which makes it easier to correct for it.

This correction is realized with a special calibration technique developed by Schüpbach et al. [14]. For calibration, a mixture of degassed purified water and CH_4 standard gas is used as an artificial melt water stream. The ratio of gas to water is 1:10 as found in ice cores. The mixture is injected close to the melt head, flows through the complete system and is finally measured by both the GC and the NIR-CRDS. By treating the standard gas and gas from ice cores the same, one takes into account systematic effects, such as dissolution of CH_4 molecules in water, incomplete gas extraction or small leaks. The result of such a calibration and how the calibration is applied on measurements is described in Section 6.3.

After the sample air has been extracted at the hydrophobic membrane, the gas is directed through a Nafion dryer [60] where residual water vapor is removed from the helium/sample mixture. The next part of the setup is a 6-port valve (Valco Instruments

Co. Inc.) which is controlled by an automated three-stage routine which distributes the sample between a LN_2 trap, the GC and the CRDS system. The three stages of the measurement routine of the GC are as follows:

1. The sample/helium mixture is directed towards the LN_2-cooled trap where CH_4 and other air components are retained. The helium that has been used as a purge gas during gas extraction does not accumulate in the trap. At the same time, the other ports of the valve are used to send a stream of helium through the GC. At this valve position the NIR-CRDS is connected with the trap and measures everything that cannot be retained in the trap (usually only helium). This valve position is maintained for one minute.

2. The valve switches position and the helium stream that was used to flush the GC is sent through the LN_2 trap. The trap has now been heated in order to release the sample which is injected into the GC. Meanwhile, the sample/helium mixture is directed towards the NIR-CRDS for CH_4 concentration measurements. This valve position is maintained for one minute.

3. The valve switches back to the initial position but measurements of the GC are still in progress. Therefore, the sample is sent through the warm trap into the NIR-CRDS. After two minutes the algorithm starts anew, i.e. the trap is cooled down and sample is retained.

In summary, the CRDS system receives sample three out of four minutes. Between these three minute intervals the spectrometer measures pure helium. The CRDS system does not interfere with the GC's measurement routine. The sample which is measured by the CRDS system during these three minutes would otherwise escape as waste.

However, during field experiments it turned out that the one minute long interruptions of the sample stream through the CFA GC-based system (valve position one) cause severe difficulties for the measurements of the spectrometer. Fig. 6.3 shows measurements of CH_4 concentration and cavity pressure from a typical CFA run. During such a 30 minutes long CFA run two 55 cm long ice core rods are melted and gases are extracted and measured continuously.

The measurement routine of the GC, during which sample is trapped, heated and finally injected into the GC for two minutes of measurement, is repeated four times during the first two-thirds of each CFA run. When sample is collected in the trap, the spectrometer receives only helium and the CH_4 concentration in the cavity decays towards zero. These four interruptions can clearly be seen in the CH_4 concentration measurements in Fig. 6.3.

The interruptions are problematic for two reasons. First of all, there is a dispersive effect in the cavity of the spectrometer which is caused by a combination of large cavity volume and small sample flow (more details in Appendix A). As a consequence of this dispersive effect, it takes ca. 100 s for the spectrometer to "recover" from an interruption, i.e. it takes ca. 100 s until all the helium is flushed out of the cavity. This leaves ca. 110 s for reliable CH_4 concentration measurements until the next interruption takes place.

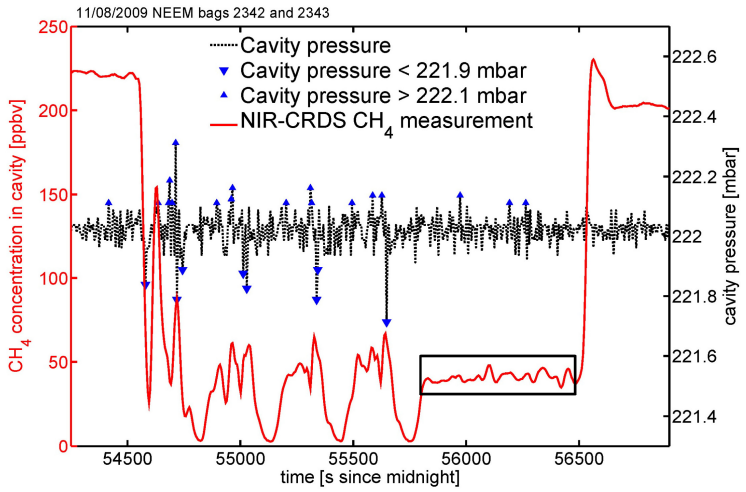

Figure 6.3: *CH_4 concentration (red) and cavity pressure measurements (black) during CFA run 2342/2343*[1]*. Before and after the run the spectrometer measures a mixture of ambient air and helium. The high CH_4 concentration of ambient air helps identify the start and end of a CFA run. During the first two-thirds of the run the measurements of the NIR-CRDS are influenced by four cycles of the measurement routine of the GC which cause strong fluctuations in both CH_4 concentration and cavity pressure measurements. The black frame marks the part of the NIR-CRDS measurements that is not influenced by GC measurements and is used to calculate the CH_4 concentration of the sample.*

Secondly, the 6-port valve switches two times during each GC routine and causes short but significant pressure fluctuations in the cavity as indicated by the blue triangles in Fig. 6.3. The highly pressure sensitive CH_4 concentration measurement is disturbed by these pressure fluctuations. Therefore, strong fluctuations of the signal occur even between two GC interruptions.

In summary, it can be concluded that no reliable CH_4 concentration measurements with the NIR-CRDS are possible during the first two-thirds of a CFA run. Therefore, data analysis is restricted to the last third where the spectrometer was able to measure without interruptions and pressure fluctuations for approximately 10 minutes. Data analysis and results are presented in the following section.

6.3 Data analysis of field experiments

In this section the analysis of measurements from the 2009 NEEM field season is presented. In order to test the performance of the CRDS system in combination with the University of Bern CFA system, 12.1 m of ice core from the early Holocene period were measured (bag number: 2334 to 2355; depth: 1283.7 – 1295.8 m from surface).

[1]Nomenclature: During CFA run X/Y the 55 cm long ice cores from bag numbers X and Y are melted and measured in succession.

In the following, the procedure for data analysis is demonstrated by presenting a detailed walk-through of the data analysis of CFA run 2342/2343. Presentation of data analysis is restricted to this typical CFA run since the procedure for data analysis is exemplary for other CFA runs. The MATLAB script of this analysis can be found in Appendix E. A summary and discussion of the results can be found in Section 6.4.

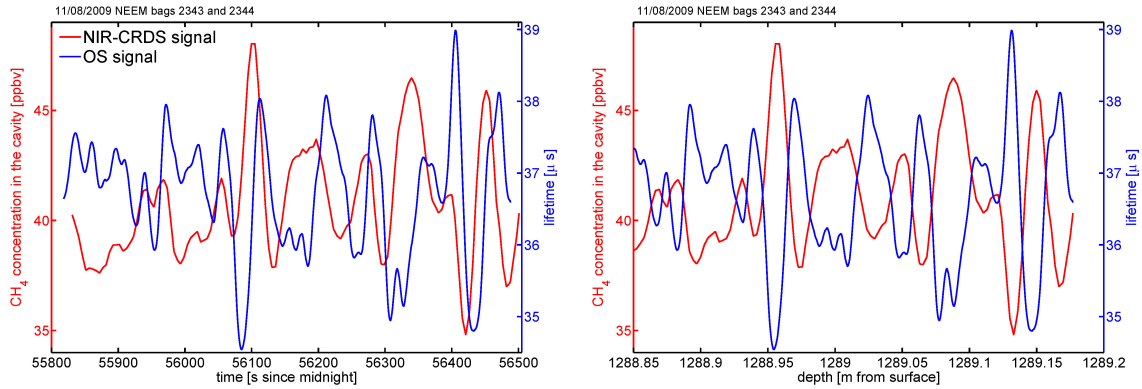

Figure 6.4: *Analysis of the uninterrupted part of CFA run 2342/2343. Left: The raw signals of NIR-CRDS and OS. The NIR-CRDS measures the number of molecules in the cavity in ppbv, whereas the OS measures the lifetime of O_2-quenched fluorescence in µs. The NIR-CRDS signal lags ca. 10 s behind the OS signal. Right: Both signals have been synchronized and are plotted on an approximate depth scale.*

The left plot in Fig. 6.4 shows the uninterrupted part of measurements from CFA run 2342/2343. The NIR-CRDS measures the concentration of the CH_4 in the cavity, whereas the OS measures the lifetime of fluorescence in μs. Both signals are unmodified and plotted on a time scale for data analysis given in seconds since midnight. As a consequence of the different positions of the two instruments in the experimental setup the signal of the spectrometer lags approximately 10 s behind the OS signal.

The synchronized signals are shown on the right plot of Fig. 6.4 on a approximate depth scale. The depth scale is simply calculated from bag number and bag length. Cuts of the ice cores which usually take place during CFA sample preparation at top and bottom of each bag and around breaks in the core are neglected. If needed this information can be retrieved from the cutting sheets of the CFA system and an accurate depth scale can be determined.

Before the signals can be used to determine the CH_4 concentration of the extracted air, they need to be converted to a common value. In order to convert the lifetime measurement by the OS to partial pressure of O_2 (p_{O_2}) the calibration of the OS is used (cf. Section 4.2.1). The signal of the NIR-CRDS, on the other hand, can be converted to partial pressure of CH_4 by

$$p_{CH_4} = p_{\text{cavity}} \cdot [CH_4]_{\text{measured}} \cdot 10^{-9}, \tag{6.1}$$

where p_{cavity} is the cavity pressure of 222 mbar and $[CH_4]_{\text{measured}}$ is the concentration of CH_4 in the cavity as measured by the spectrometer. In principle, the concentration of CH_4

in the sample can now be calculated by

$$[CH_4] = \frac{p_{CH_4}}{p_{O_2}/0.2095} \cdot 10^9, \tag{6.2}$$

where p_{CH_4} is the partial pressure of CH_4. The factor $1/0.2095$ converts partial pressure of O_2 to partial pressure of air. However, a calculation of the concentration of CH_4 at this stage would be very imprecise. For results of high precision the OS signal needs to be convoluted with a smoothing function in order to smooth the signal (cf. Eq. (5.4)). More details about the necessity for the convolution and the smoothing function can be found in Section 5.4.2 and in Appendix A, respectively. The smoothing function has two parameters, a smoothing constant and a length, which are optimized for the analysis of each CFA run. The smoothing function with optimized parameters is then used to convolute the signal from the OS.

In summary, the initial signal from the OS has so far been converted to partial pressure, synchronized with the NIR-CRDS signal and convoluted with the optimized smoothing function. The initial signal from the NIR-CRDS has been converted to partial pressure. These two modified signals are shown in the left plot of Fig. 6.5, again, on an approximate depth scale. The two signals are now well correlated and ready to be used for determination of the CH_4 concentration with the use of Eq. (6.2).

The result is shown in the right plot of Fig. 6.5. It has a high autocorrelation and we cannot calculate a standard deviation in order to estimate the uncertainty of the measurement since the values do clearly not follow a Gaussian distribution. They all lie between 225 and 207 ppbv. The melt rate of 35 mm/min in combination with the average sampling frequency of the spectrometer of 2.6 Hz yields one measurement every 1.5 mm of ice core.

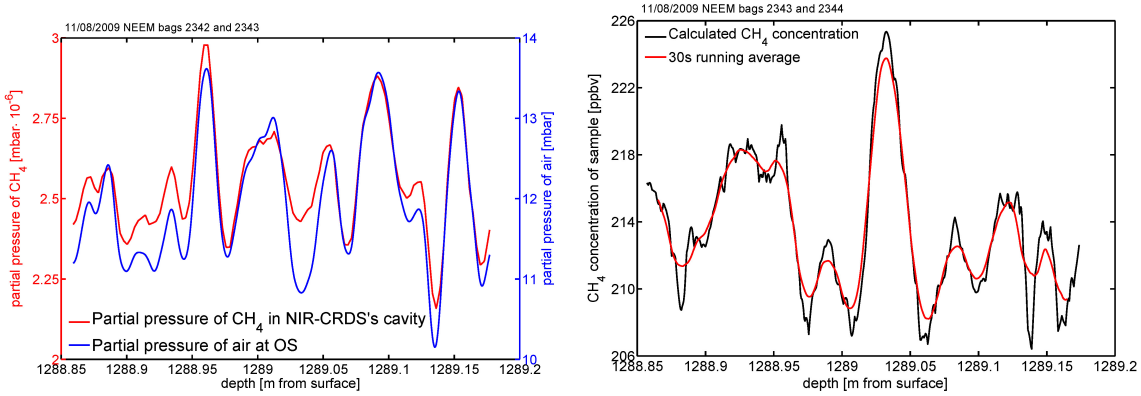

Figure 6.5: *Analysis of the uninterrupted part of CFA run 2342/2343. Left: NIR-CRDS and OS signal after conversion to partial pressure of CH_4 and O_2, respectively. Additionally, the OS signal has been smoothed by convolution with an optimized smoothing function. Right: The result of the calculation of the CH_4 concentration of the sample from the two signals shown on the left. The solid red line shows the result after a 30-seconds running-average has been applied.*

However, this is not the true resolution of our method. Dispersion in the sample transfer lines and especially in the large volume of cavity of the NIR-CRDS decrease the resolution

of the method. In Appendix B the resolution of the method is estimated by studying the response of the system to a step function. These estimations imply that one can not distinguish any signal from the noise of the measurement which has a wavelength shorter than approximately 19 mm. In other words, the CRDS method cannot, in spite of the high sampling frequency, resolve more details than a method with a sampling frequency of 0.15 Hz. Nevertheless, this is still a higher resolution compared to all discrete and semi-continuous methods which were introduced in Section 1.3.

Since the resolution of the method is 19 mm we apply a 30-seconds running-average to the results (19 mm melt in 30 seconds). Thus, the averaged result shows the "real" signal without measurement noise that creates wiggles below the resolution limit. The average is shown as a solid red line in the right plot of Fig. 6.5.

The averaged results shows fluctuations as large as 6 ppbv over only 4–5 cm of ice core. The approximate annual layer thickness at a depth of 1300 m at NEEM is ca. 6.3 cm (Sigfus J. Johnsen, personal communication 2010). Thus, 4–5 cm of ice core correspond to less than one year and the fluctuations cannot be a real atmospheric signal. Diffusive processes in the firn completely damp changes in the atmospheric CH_4 concentration which occur within one year. Thus, the fluctuations in the results are attributed to uncertainties in the CRDS system.

The synchronization of both measurements and smoothing of the OS signal yields a correlation of 0.9584 between the NIR-CRDS signal and the smoothed OS signal (> 0.95 for all CFA runs). The good correlation between parts of the two signals can also be seen in the left plot of Fig. 6.5. Even though the two signals are well correlated, one can observe some discrepancies. An obvious example is the peak in CH_4 concentration at a depth of ca. 1289.03 m where the differences between NIR-CRDS and OS signal are large.

This alternation of well-correlated parts and parts that show discrepancies points to uncertainties in one or both of the two measurements. The smoothing function can only smooth the OS signal but cannot correct for measurement uncertainties. These uncertainties can be caused by fluctuations in one of the signals that are not related to changes in CH_4 and O_2 but to flow, pressure or temperature changes.

The NIR-CRDS operates at the default cavity pressure and within the appropriate flow range of the valves. The cavity pressure and temperature are stable throughout the measurements. Therefore, the CH_4 concentration measurements are reliable and of a high precision and accuracy. Moreover, the calibration of the NIR-CRDS is straight forward due to the linear relation between the ring-down time and the number of CH_4 molecules in the cavity.

The situation of the OS, on the other hand, is more complicated.

- The exact pressure at the probe of the OS is unknown since it is installed upstream from the cavity where pressure measurements take place. A filter between OS and cavity acts as a flow restriction which implies that the pressures at OS and in the cavity are slightly different.

- Calibration of the OS is complicated (cf. Section 4.2.1) and cannot be conducted frequently in the field. The calibration of the OS has been conducted in September,

but measurements already took place in August. Additionally, the calibration was imprecise as the error calculation in Appendix C shows.

- Furthermore, the measurements of the OS can be inaccurate since the fluorescence of the sol-gel complex of the probe is known to wear off with time and a drift in the measurement is expected. Unfortunately the relation between lifetime and partial pressure of O_2 cannot be described by a simple function which makes a belated correction for a potential drift of the OS signal difficult.

In summary, it can be concluded that the observed fluctuations in the results are not an atmospheric signal and must be related to uncertainties in one of the two measurements. The NIR-CRDS can be excluded as the origin of these fluctuations. The signal of the OS, on the other hand, is known to drift and its calibration is problematic. Hence, the fluctuations in the results can be attributed to uncertainties and inaccuracy of the signal of the OS.

Finally, the CFA calibration described in Section 6.2 is applied to the results in order to correct for losses of CH_4 during the melting and gas extraction processes as well as for leaks in the system. The calibration run is treated like a normal CFA melt run during data analysis. The NIR-CRDS and OS signals of the calibration run are shown in the left plot of Fig. 6.6. Eq. (6.2) is used to calculate the CH_4 concentration of the sample stream. The results and a 30-seconds average are shown in the right plot of Fig. 6.6.

The mean value of the non-averaged results of the CFA calibration run (266.4 ppbv) is used to generate a calibration curve which is shown in the right plot of Fig. 6.7. This curve is used to correct the non-averaged calculated CH_4 concentration values of each CFA melt run. The result of this correction and a 30-seconds average for run 2342/2343 are shown on the left plot of Fig. 6.7.

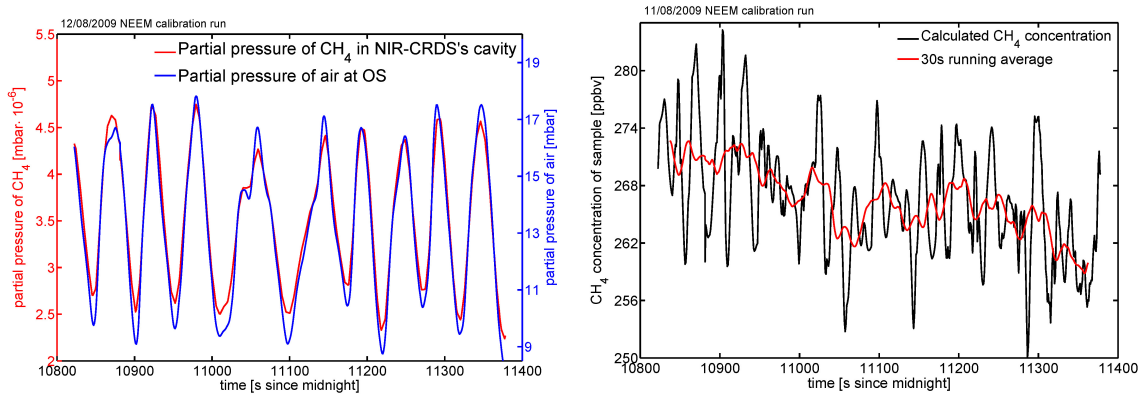

Figure 6.6: *CFA calibration run. Left: NIR-CRDS and OS signal from the uninterrupted part of the calibration run. Both signals are synchronized and the OS signal is convoluted with an optimized smoothing function. Right: The result of the CH_4 concentration calculation (black) from the two signal from the left and the 30-seconds average (red).*

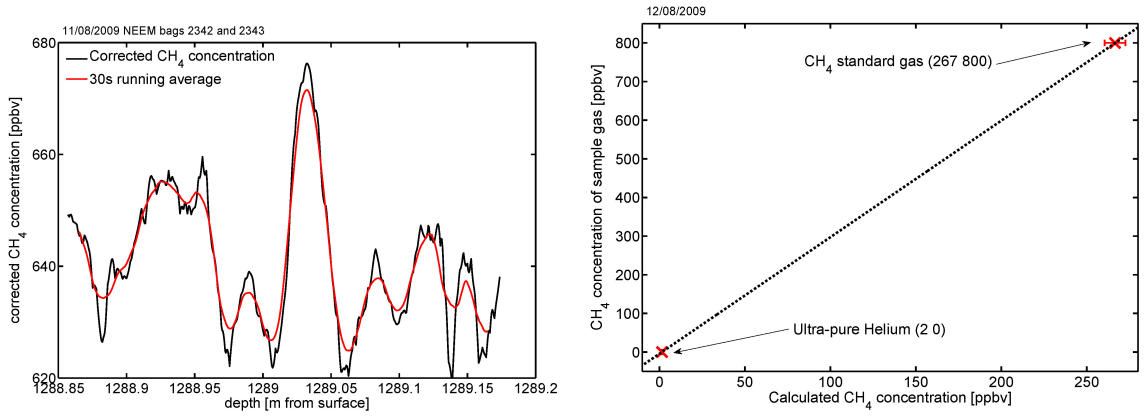

Figure 6.7: *Analysis of the uninterrupted part of CFA run 2342/2343. Left: The results of the CH_4 concentration of run 2342/2343 calculation have been corrected by using the CFA calibration. Right: The CFA calibration curve used for correction.*

6.4 A summary of the 2009 NEEM field experiments

This section presents the complete data set from the 2009 NEEM field season measured by the CRDS system and discusses the quality of these results. Fig. 6.8 shows the complete data set from the 2009 NEEM field season. The calculated CH_4 concentrations (black) is shown before (upper plot) and after (lower plot) the CFA calibration has been applied. The results are also shown after a 30-seconds running-average has been applied (red). Data from CFA run 2346/2347 cannot be used for any gas analysis due to technical problems at the gas extraction unit.

Bag number 2334–2345:
All results from bags 2334–2345 are fragmentary due to interruptions of the sample flow by the GC system during the first two thirds of each run as described in Section 6.2. This means for the CRDS system, that only the last third of each run can be analyzed. Thus, results for those CFA runs exist only for parts of the second ice core bag of each run (two bags of ice are melted during each CFA run).

The results of all runs are highly autocorrelated which prevents an estimating the precision of the method by giving a standard deviation and a mean value. As discussed before these fluctuations are attributed to imprecise and inaccurate measurements of the OS. It can be stated that all calculated past atmospheric CH_4 concentrations, after calibration correction, lie between 600 and 650 ppbv with the exception of run 2340/2341 where values go up to almost 700 ppbv.

The temporal resolution is estimated to be approximately 19 mm based on studies of the response of the system to a step function as presented in Appendix B.

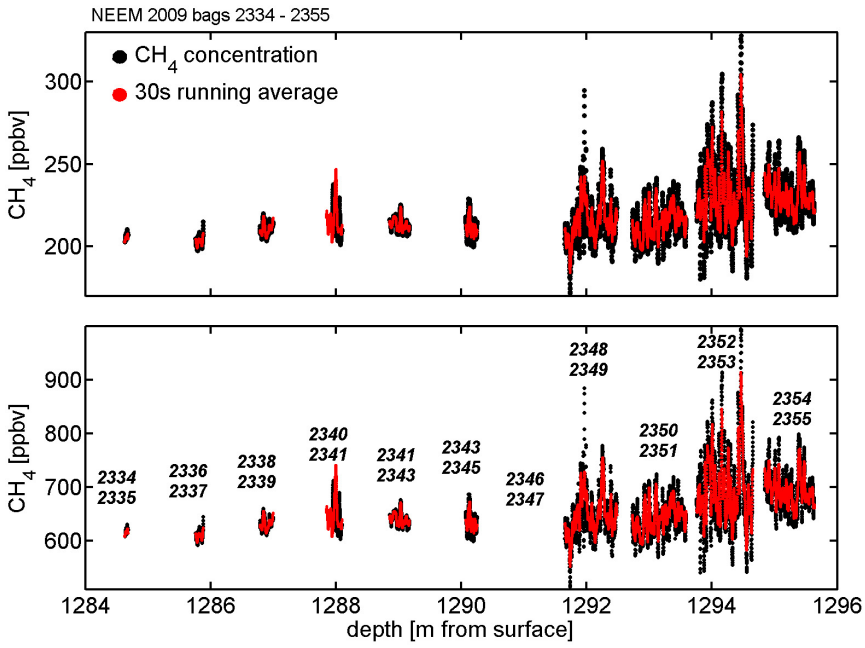

Figure 6.8: *Calculated CH_4 concentration of air from all ice cores measured during the 2009 NEEM field season with the CRDS system for on-line CH_4 concentration measurements. Top: The unmodified CH_4 concentrations (black) and after a 30-seconds running-average has been applied (red) are plotted on an approximate depth scale. Bottom: CH_4 concentrations after calibration correction.*

Bag number 2348–2355:

Ice cores from bags 2348–2355 were measured without interruptions because no measurements of the GC system took place during these CFA runs. The reason was a broken Nafion dryer that had to be bypassed. Since the GC, including the LN_2 trap, cannot operate at high humidity levels, the measurement routine of the GC was interrupted and sample constantly directed towards the NIR-CRDS. Again, the results are highly autocorrelated and show the same pattern as the runs described above. However, fluctuation in these results are even stronger and values vary between 500 and 1000 ppbv. Estimated temporal resolution is again 19 mm.

Thus, the advantage of a continuous record over eight bags of ice core is overshadowed by the occurrence of even stronger fluctuations in the calculated CH_4 concentration compared to CFA runs that included the Nafion dryer. This influence can clearly be seen in Fig. 6.8 where the calculated CH_4 concentration from the last four runs shows larger fluctuations than earlier runs.

The only changes applied between run 2344/2345 and run 2348/2349 was the removal of the Nafion dryer and the 6-port valve. The Nafion dryer has two effects on the gas stream: (1) The dryer acts as a flow restriction (ID = 356 μm) and thereby changes the downstream gas pressure. (2) The dryer removes water vapor from the humid gas stream that comes from the CFA gas extraction unit. In the following paragraphs a potential

influence of these effects on the CH_4 concentration measurements is analyzed (the removal of the 6-port valve should not have any effect on the quality of the measurements).

1. Since the Nafion dryer acts as a flow restriction in the gas stream the absence of the dryer could potentially have an effect on the cavity pressure. Since pressure in the cavity is constantly recorded this hypothesis can easily be checked. It can be concluded that the cavity pressure is not influenced by the absence of the Nafion dryer as illustrated in the left plot of Fig. 6.9 where no unusually strong pressure fluctuations can be observed. Moreover, the few pressure fluctuations we can observe are normal and not at all correlated with the CH_4 signal. Hence, pressure fluctuations in the cavity, as seen for instance during GC measurements, can be excluded as a reason for the high fluctuations of our results.

2. Another effect of the missing Nafion dryer that could influence the measurements is the high humidity of the gas stream. Measurements are disturbed whenever an absorption line of H_2O interferes with the absorption feature of CH_4. The higher the humidity level is, the broader the absorption lines of H_2O become and the easier they can interfere with other lines.

   The absorption feature of CH_4 (green) that is used for concentration measurements by the NIR-CRDS is shown in the right plot of Fig. 6.9. The plot also shows the very close neighboring line of H_2O (red). The details shown in the insert of the figure reveal that the two lines overlap. The absorption line of H_2O is shown for a concentration of 20,000 ppm which was the H_2O concentration measured by the NIR-CRDS during the wet CFA runs. However, the detector for H_2O measurements was saturated and the real humidity level was even higher. Without the dryer the gas stream should be almost saturated with H_2O vapor and the H_2O absorption line was stronger than shown in Fig. 6.9.

   It can be concluded that the high humidity levels had an influence on the CH_4 concentration measurements.

In summary, it can be said that the absence of the Nafion dryer has no influence on the cavity pressure but it surely does have an influence on the CH_4 concentration measurements since the absorption lines of CH_4 and H_2O overlap. The removal of the Nafion dryer is the only change in the setup between CFA run 2344/2345 and run 2348/2349. Thus, the stronger fluctuations of the results for the latter can be attributed to the high humidity levels.

Final conclusions of the 2009 NEEM field measurements:
To get an idea of the accuracy of the method, results are compared to measurements from another ice core. For this purpose the depth scale is converted to a preliminary age scale by using a model ice age scale for the NEEM site (Dorthe Dahl-Jensen, Susanne L. Buchard and Bo M. Vinther, personal communication 2010). The ice age is converted to gas age

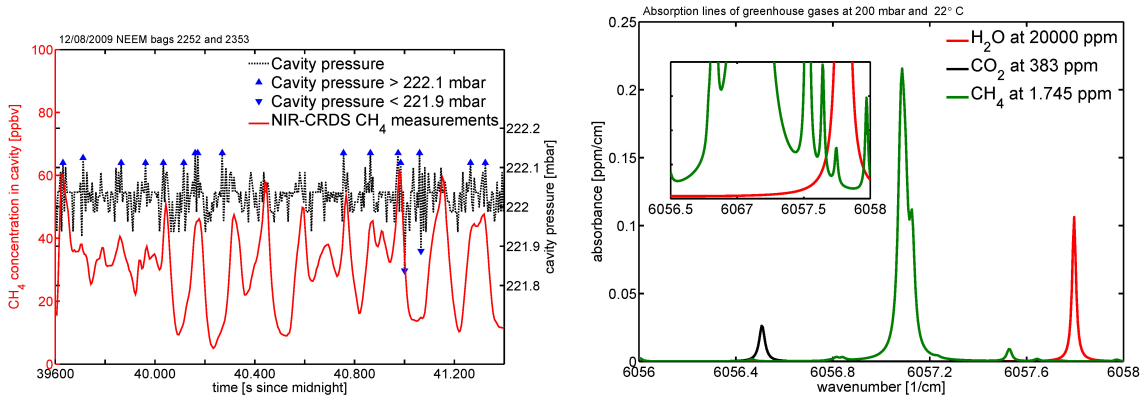

Figure 6.9: *Left: The cavity pressure (black) and the CH_4 concentration measurements (red) during CFA run 2352/2353. The blue triangles mark incidents with cavity pressures above 222.1 mbar and below 221.9 mbar, respectively. No unusual pressure fluctuations occur in the absence of the Nafion dryer. Right: The Doppler profile of CH_4 used by the spectrometer for concentration measurements (green) and neighboring profiles of H_2O (red) and CO_2 (black) at 200 mbar cavity pressure and 45°C. The profile of H_2O is given for a high humidity level of 20000 ppm. The insert shows that the lines of CH_4 and H_2O overlap, which proofs that the high humidity of the sample gas in the absence of the Nafion dryer has an influence on the CH_4 measurements. Data from the HITRAN database plotted with the help of David Balslev-Clausen.*

with the use of a preliminary estimate of the Δ age for the NEEM site of 175 years which is based on firn studies. Unfortunately, no CH_4 concentration data for the gas age of our measurements (9025 - 9225 yr b2k) exist. The two closest CH_4 concentration data points (9018.24 and 9313.19 yr b2k) are from the GRIP core [3] and are plotted together with the NEEM results in Fig. 6.10.

It can be concluded that the more reliable results which are measured during the dry CFA runs (including the Nafion dryer) are slightly lower than the GRIP results. The strong fluctuations of the results from the wet CFA runs prevent an estimation of their accuracy. Even though the GRIP and NEEM measurements are not exactly at the same depth it is unlikely that the NEEM measurements are very accurate. If they were, atmospheric CH_4 concentration would make a jump of ca. 75 ppbv within only ca. 25 years (between the first NEEM measurement and the earlier datum from the GRIP core). When looking at GRIP measurements of younger and older ice, no such jumps can be observed (not shown). This makes the existence of rapid jumps in atmospheric CH_4 concentration during that period very unlikely and points to inaccuracies in the NEEM measurements.

In Appendix C the uncertainties of the NEEM results are determined. Due to large uncertainties in the calibration of the OS, the final uncertainties of the results are of the order of $\pm$ 100 ppbv. This means that the NEEM results agree with the GRIP measurements within their uncertainties. However, this frame is too large and the calibration of the OS has to be improved in order to obtain more accurate measurements.

The comparison to CH_4 concentration measurements from the GRIP core shows how coarse the data set from discrete measurements is. If the problems of precision and accuracy

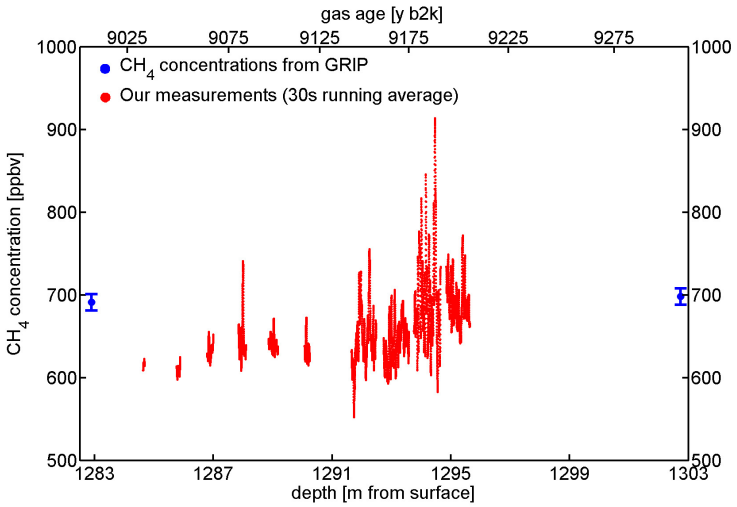

Figure 6.10: *The averaged CH_4 concentration measurements from the CRDS system are plotted together with CH_4 concentration measurements from the GRIP core on a preliminary depth and age scale.*

of the CRDS method could be solved, the resolution of CH_4 concentration measurements from ice cores will be improved significantly.

The quality of the NEEM results depends strongly the presence of a Nafion dryer. For the dry CFA runs the calculated CH_4 concentrations do not fluctuate more than 25 ppbv. To get a good estimate of the precision the problem of autocorrelated results has to be solved. Improvements should focus on the total air content measurement since the measurements from the OS seem to be afflicted with high uncertainties. With an improved system one could aim for more CH_4 concentration measurements from dry, uninterrupted CFA runs.

Even though results from the CRDS system for continuous on-line CH_4 concentration measurements cannot yet compete with the precision of established discrete and semi-continuous measurements, the experiences from the first field experiments are valuable. From these experiments it became clear where the system needs improvement in order to deal with the special conditions found for continuous gas measurements couple to a CFA system. In the following chapter future plans for the CRDS system are described in detail.

Chapter 7

Conclusion and outlook

Section 7.1 provides a summary of the work that has been presented in this thesis. During this work it turned out that the main challenge of continuous CH_4 concentration measurements in combination with a CFA system is limited sample size. This problem is described in Section 7.2. Then, future prospects of how to improve the system are summarized in Section 7.3.

7.1 Summary

7.1.1 Preparations for the 2009 field season

Preparative test of the CRDS system for the 2009 field season are presented in Chapter 5. Here, the main objective is to find a reliable and practical instrument for measurements of total air content which is necessary due to the dilution of sample with helium in the field setup (cf. Section 5.2). In the field the sample gas is extracted from the melt water stream in a way that matches the requirements of another system for CH_4 concentration measurements. Since the measurements of this GC-based system cannot be disturbed the CRDS system has no influence on the extraction process.

Two instruments, an OS and a TCD are tested for measurements of total air content. These tests yield a precision of the CH_4 concentration measurements of $\pm$ 10 ppbv for the combination of NIR-CRDS and TCD and $\pm$ 20 ppbv for the combination of NIR-CRDS and OS, respectively. However, the results of the NIR-CRDS/OS system are expected to improve under field conditions where a more stable pressure in the sample stream should improve the precision of the pressure-sensitive measurements of the OS.

The OS has some practical advantages compared to the TCD which make it well-suited for field measurements, for instance its small size and the fact that it does not require an additional reference gas. Thus, the OS is used for field measurements in spite of its slightly worse precision.

7.1.2 The 2009 field season

In the field the combined system of NIR-CRDS and OS is connected to the CFA system from the University of Bern as described in Chapter 6. From their gas extraction line the NIR-CRDS system receives a dry sample/helium mixture (ca. 1.5 ml/min sample diluted with 20 ml/min of helium). However, this stream is interrupted every fourth minute due to measurements of the GC-based system. As a consequence of these interruptions only the measurements of the last third of each CFA run can be used for CH_4 concentration determination. During the last third of a run the GC does not measure at all.

Atmospheric CH_4 concentrations are measured along 12.1 m of ice core. The results are shown in Fig. 6.8. When the sample/helium mixture is dry the fluctuations in the results are below 25 ppbv. The temporal resolution of the system is estimated to be ca. 2 cm as shown in Appendix B.

The results from the 2009 field season are compared to measurements from the GRIP core in Fig. 6.10 which shows that CH_4 concentration measurements from the GRIP core are 50–100 ppbv higher than the NEEM measurements from the CRDS system. The reason for the inaccurate results from the CRDS system is the imprecise and inaccurate calibration of the OS as described in Section 6.4.

With hindsight after the field experiments it can be concluded that the decision for the OS, and against the TCD, was a mistake since both precision and accuracy of the method are significantly downgraded by the OS. The hope that the quality of the measurements from the OS would improve under field conditions was not fulfilled. The TCD, on the other hand, showed better results in the preparative tests. These results should remain better than the results from the OS even under field conditions. Moreover, the calibration of the OS first took place after the field season and the significant uncertainty introduced by the calibration was not predicted beforehand (cf. Appendix C).

7.2 The trade-off between temporal resolution and precision

Continuous measurements of CH_4 concentrations from ice cores in combination with a CFA system have one major problem, namely limited amount of sample. The given melt speed of the CFA system of the University of Bern (35 mm/min) results in a sample air stream of only 1.5 ml/min. The semi-continuous GC system presented in Section 1.2 solves this problem by accumulating the sample over one minute in a LN_2-trap. Then, the amount is sufficient for one GC measurement. However, in order to improve the temporal resolution continuous measurements are necessary and one has to find a way to handle the limited sample size.

In principle, the NIR-CRDS can measure a flow of 1.5 ml/min with its standard accuracy and precision[1]. In this case precision and accuracy are excellent but the problem are

[1]This has now been tested in combination with the CFA from the Center for Ice and Climate including a novel gas extraction line. Only minor modifications on the gas tubing of the NIR-CRDS had to be

large dispersive effects in the CRDS system. These effects are caused be dispersion of the sample in the system, especially in the large volume of the cavity of the NIR-CRDS, and the temporal resolution of the method decreases significantly. How dispersion influences the temporal resolution is described in Appendix B.

To improve the temporal resolution the sample can be mixed with a carrier gas like helium. Thereby, the flow of the sample/helium mixture increases, the cavity is flushed faster and the memory effect of the system decreases. This is the approach that has been used for the experiments described in this thesis since the sample stream is mixed with helium (ca. 20 ml/min) during gas extraction in the field setup as shown in Chapter 6. Even though the helium helps to flush the cavity of the NIR-CRDS, the intention of this dilution is different. In the gas extraction line of the CFA system of the University of Bern helium is used to flush sample away from the hydrophobic membrane which extracts the gases from the melt water stream as shown in Fig. 5.1. As a consequence, we have no influence on the amount of helium that is mixed into the sample stream.

When measuring such a sample/helium mixture one achieves a good temporal resolution but encounters another problem. The information about the air content of the sample/helium mixture is unknown and one needs a measurement of total air content in order to determine the CH_4 concentration in the sample part of the sample/helium mixture. This is explained in detail in Section 5.2. For this purpose, the NIR-CRDS was equipped with a OS which measures the partial pressure of O_2 in the sample/helium mixture.

As the results from the 2009 field season show the precision of the method is downgraded significantly when the CH_4 concentration is determined with the help of the measurements from the OS. This is the consequence of the difficult calibration of the OS as well as of a gradual degradation of the OS's coating as discussed in Section 6.4.

In the following section we elaborate on the usefulness of high-resolution measurements. Then, we propose improvements that can solve the dilemma of not having a system for CH_4 concentration measurements with both high precision and high temporal resolution in Section 7.3.

7.3 Future prospects

There are two different approaches for measuring CH_4 concentrations from ice cores with a CRDS system. One is to measure the pure air sample stream that is extracted from the melt water stream of the CFA system. This approach yields precise and accurate results but faces problems in terms of dispersion and low temporal resolution. The second approach is to dilute the sample with a carrier gas like helium and include an instrument for measurements of total air content into the system. In our case. this approach offers a good temporal resolution but less precise and less accurate results due to the problematic air content measurement of the OS. In the following we present suggestions that can improve either of these approaches.

conducted. For reasons of time this has not been included in this thesis.

7.3.1 Pure-sample approach

Measurements of pure sample are only possible with an improved gas extraction line. Recently, an new hydrophobic membrane unit has been tested successfully which allows the extraction of gases under low-pressure (0.5 x 1 Micromodule, Membrana GmbH). In that way, more of the gases that are dissolved in the melt water can be extracted. The material of the new membrane unit is still hydrophobic polypropylene (Section 6.2). However, the new unit consist of a bundle of these membranes which multiplies the area of gas exchange. Moreover, the module itself is vacuum-sealed which makes operation at low-pressure possible.

This new gas extraction module enables us to omit the mixing of the sample with helium which has been used so far to flush the hydrophobic membrane. Now the sample air is sucked away from the gas extraction module by the pump of the NIR-CRDS.

When measuring pure sample it is necessary to decrease the dispersion in the system in order to improve the temporal resolution of CH_4 concentration measurements. Even though some advancement can be achieved by minimizing the size and surface of tubing, valves etc., the gain in resolution from these improvements is limited. The cavity of the spectrometer with its large volume of ca. 33 cm^3 is the main contributor to the sample's dispersion and resolution-improving attempts have to be applied here.

- The **volume of the cavity** can be reduced by improving the machining of the cavity body. A sketch of the cavity is shown in Fig. 4.2 where the complete NIR-CRDS is depicted. When machining the cavity from one piece of stainless steel the volume should be kept as small as possible so that the walls are very close to the laser beam. Room for improvement exists on all sides of the cavity as well as in the middle of the laser path. This triangular area should be filled with stainless steel. In this case, the beam would be sent through a "tunnel" that is machined into the cavity body.

- The **positions of the gas inlet and outlet** can be improved too. Both inlets are located at the top of the cavity and are indicated as dashed gray circles in Fig. 4.2. They are located rather far from the mirrors and, as a consequence, the volumes between mirrors and gas inlet/outlet are not sufficiently flushed when sample flow is low. Here, sample accumulates and increases the memory effect of the cavity. Ideally, the gas would be injected and sucked out, respectively, directly in front of the mirrors in order to flush the complete volume of the cavity. If positioning close to the mirrors is not possible (issues of space since the inlet and outlet of the laser beam are located here) the gas could be injected in an angle in order to "spray" the gas into the vicinity of the mirror.

- The standard **cavity pressure** of the NIR-CRDS is 222 mbar. However, the pressure can be freely adjusted by changing the opening of the inlet and outlet valves. A lower cavity pressure reduces the effective volume of cavity and dispersion becomes less. The absorption feature of CH_4 is pressure dependent and will become narrower when the cavity pressure is reduced as explained in Section 3.1. This implies that the

fitting procedure which determines the area under the absorption feature has to be adjusted to the lower pressure conditions.

7.3.2 Diluted-sample approach

The dilution-approach that was used for the all experiments described in this thesis can be improved too. As mentioned before the OS introduces large uncertainties to the determination of the atmospheric CH_4 concentration and is responsible for the unsatisfying precision and accuracy of the dilution approach.

There are other instruments that can be used for measurements of total air content, e.g. a TCD. The preparative test with the TCD yielded better results than the OS, but the practical advantages of the OS led us decide in favor of the OS for field measurements. However, the TCD is easier to calibrate (total air content linearly related to applied voltage) and does not show a significant drift over time. These advantages make it worthwhile to test a NIR-CRDS/TCD system in combination with the CFA.

Appendices

Appendix A

The smoothing function

This appendix describes the use of a smoothing function which improves the results from data analyses of measurements described in the Chapters 5 and 6. For reasons of clarity the following descriptions are restricted to the OS. However, all descriptions apply to the TCD as well.

When the sample of atmospheric air is diluted with helium or another carrier gas one needs at least two measurements in order to determine the concentration of CH_4 in atmospheric air:

1. A measurement of the partial pressure of air in the air/helium mixture. The OS measures partial pressure of O_2 which can be converted to the partial pressure of air by assuming a constant atmospheric O_2 concentration of 20.95%.

2. A measurement of the partial pressure of CH_4 in the air/helium mixture. The NIR-CRDS measures the concentration of CH_4 in its sample cavity in ppbv. Since the pressure in the cavity is known ($p_{\text{cavity}} = 222$ mbar), the measurements can be converted to partial pressure of CH_4 by

$$p_{\text{CH}_4} = [CH_4]_{\text{measured}} \cdot p_{\text{cavity}} \cdot 10^{-9}, \tag{A.1}$$

   where $[CH_4]_{\text{measured}}$ is the concentration of CH_4 measured by the NIR-CRDS and p_{CH_4} is the partial pressure of CH_4.

With both the partial pressures of air and the partial pressure of CH_4 known, the atmospheric concentration of CH_4 can be calculated by

$$[CH_4] = \frac{p_{\text{CH}_4}}{p_{\text{air}}} \cdot 10^9, \tag{A.2}$$

where p_{air} is the partial pressure of air and $[CH_4]$ is the CH_4 concentration of the sampel given in ppbv.

However, this calculation is problematic. The combination of a low sample flow and a large volume of the cavity of the NIR-CRDS creates dispersive effects in the cavity.

This dispersion affects only the measurements of the NIR-CRDS since the OS is installed upstream from the cavity where dispersive effects are minimal (cf. Chapter 5). Thus, the response of the NIR-CRDS to a change in the sample-to-helium ratio differs significantly from the response of the OS. Examples are shown in Fig. A.1. This differences result in a very imprecise calculation of the CH_4 concentration of the sample with the use of Eq. (A.2).

.

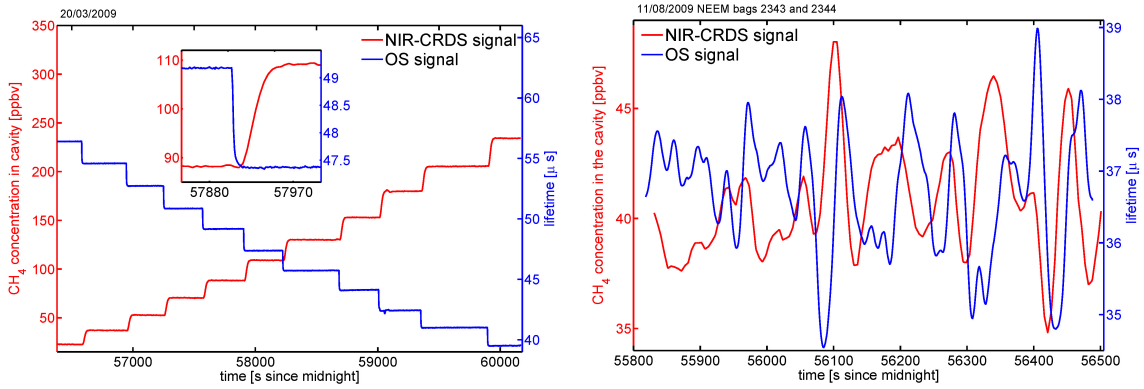

Figure A.1: *Dispersion of the sample in the cavity of the NIR-CRDS leads to differences between the OS signal (blue) and the NIR-CRDS signal (red). Left: Measurements during the performance test of the OS (cf. Chapter 5). Right: Measurements during the NEEM CFA run 2342/2343 (cf. Chapter 6). In both experiments the measurement from the OS is less smoothed than the measurement from the NIR-CRDS.*

One way to solve this problem is to actively smooth the OS measurement so that it resembles the measurement of the NIR-CRDS. This can be achieved by calculating the convolution of the OS measurement with a discrete smoothing function $s(t)$ which is given by

$$s(t) = a \cdot e^{-\frac{t}{\tau_s}} \quad \text{with} \quad a = \left[\sum_{t=t_1}^{t_2} e^{-\frac{t}{\tau_s}} \right]^{-1}, \tag{A.3}$$

where t is a discrete variable and τ_s is a "smoothing constant". The function $s(t)$ is normalized by a. The time constant τ_s and the length of the smoothing function (the number of data points t covered by the function) characterize the dispersive effects. The measurement of the OS is convoluted with the smoothing function to actively smooth the measurement:

$$f(t)_{\text{smoothed}} = s(t) * f(t), \tag{A.4}$$

where $f(t)$ and $f(t)_{\text{smoothed}}$ is the original and the smoothed measurement of the OS, repsectively. The effect of this convolution is shown for measurements of the OS and for theoretical functions in Figs. A.2 and A.3, respectively.

The precision of the calculated atmospheric CH_4 concentration (Eq. (A.2)) improves when the measurement of the OS is convoluted with the smoothing function beforehand. The reason being the improved correlation between the two measurements.

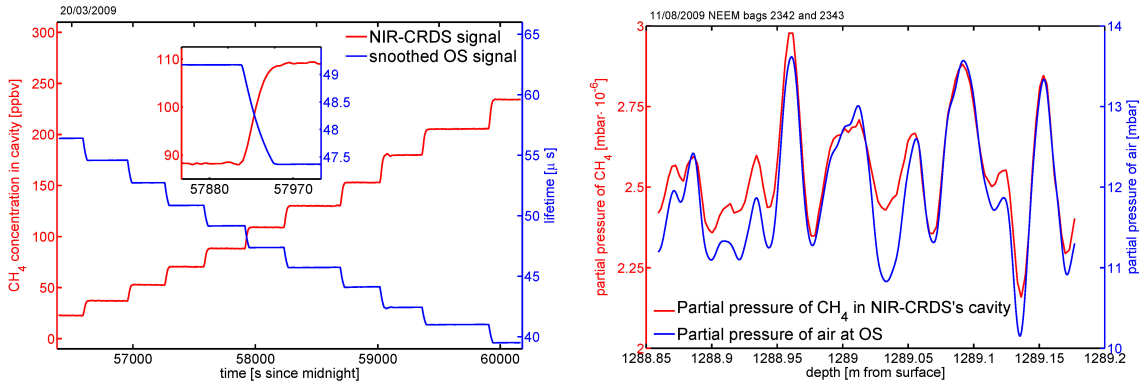

Figure A.2: *The effect of the convolution of the measurement of the OS with the smoothing function. The correlation between the convoluted OS signal (blue) and the NIR-CRDS signal (red) improves. Left: Measurements during the performance tests of the OS (cf. Chapter 5). Right: Measurements during the NEEM CFA run 2342/2343 (cf. Chapter 6)*

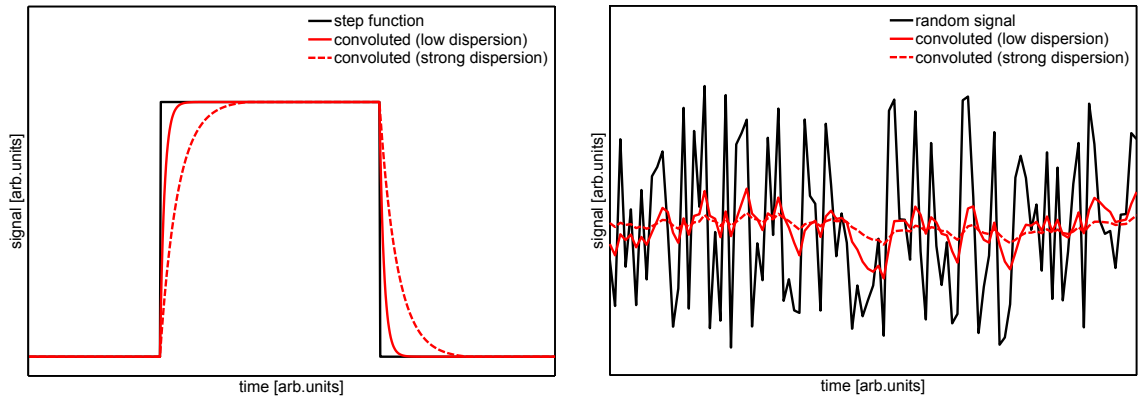

Figure A.3: *The effect of the convolution of a theoretical function with the smoothing function. Strong dispersion is simulated with a high mixing constant τ_s and vice versa. Left: A step function before (black) and after convolution with the smoothing function (red). Right: A random signal before (black) and after convolution with the smoothing function (red).*

The choice of an exponential smoothing function function has a theoretical background. In the following the smoothing function is derived with the use of the very general step function. The generality comes from the fact that every signal can be described by a series of $n \to \infty$ step functions with infinitesimal small step size.

Let's assume a flow of gas through a volume V which is perfectly mixed and an upstream step-wise change in gas concentration from concentration $c_1 + c_2$ to concentration c_1. Let's further assume that the flow of gas in and out of a volume is constant and denoted with Φ given in ml/s. A differential equation that describes the change in concentration inside the volume is given by

$$\frac{dc}{dt} = \frac{1}{V} \cdot (\Phi \cdot c_1 - \Phi \cdot c(t)) \,, \tag{A.5}$$

where $c(t)$ is the concentration in the volume as a function of time. A solution to this differential equation is

$$c(t) = c_1 + c_2 \cdot e^{-\frac{\Phi}{V} \cdot t}. \tag{A.6}$$

The term Φ/V is a constant and is given in 1/s. The reciprocal of this constant term can be called smoothing constant τ_s and Eq. (A.6) becomes

$$c(t) = c_1 + c_2 \cdot e^{-\frac{t}{\tau_s}}. \tag{A.7}$$

This means that an initial step-wise change in concentration will have an exponential shape after passing a volume of finite size. The shape depends on the time constant τ_s which represents the degree of dispersion caused by a combination of sample flow and volume.

Appendix B

Estimation of resolution

This appendix describes how the resolution of the CRDS system can be estimated by studying the response of the NIR-CRDS and the OS to a step function. From these studies the dispersive (smoothing) effects of the system on periodic signals with different wavelengths can be estimated.

The combination of a CRDS and a CFA system has the potential for high-resolution measurements of CH_4 concentrations from air extracted from ice cores. Ice cores are climate archives of high resolution, and the continuous melt and gas extraction process of the CFA system allows for continuous measurements. The NIR-CRDS can measure CH_4 concentrations from the continuous gas stream with a high sampling rate (ca. 2.6 Hz).

The melt rate of the CFA system is 35 mm/min. With a sampling rate of 2.6 Hz the NIR-CRDS conducts one measurement for every 1.5 mm of ice core. However, this is not the actual resolution of our system. Dispersion of the sample occurs when it is transported through the tubing of the system and especially in the large volumes of the debubbler, the gas extraction unit and the cavity of the NIR-CRDS. As a consequence of this dispersion, the resolution of the measurements of the CRDS system decreases. Of special interest for these measurements is the dispersion that takes place in the cavity. This volume ($7cm^3$) is by far the largest volume in the system and has the potential to decrease the maximal resolution of the CRDS system significantly.

In the following a technique for the estimation of the dispersive effect of the cavity of the NIR-CRDS is presented. It is based on work by Vasileios Gkinis (personal communication, 2010).

The preparative performance test of the OS, described in Chapter 5.5, provides an ideal data set for the resolution estimation due to its simple experimental setup (cf. Fig. 5.9). The setup consists only of two gas bottles (air and helium), some tubing and valves, a pressure regulator, the OS and the NIR-CRDS. This simplicity keeps the dispersive effects before the cavity of the spectrometer very low. During this performance test air and helium are mixed in a tee piece and the mixture is send directly to the NIR-CRDS. The OS is installed upstream from the NIR-CRDS. During the experiment the air-to-helium ratio is changed step-wise by adjusting the gas stream pressure with the pressure regulator.

The focus of the following analysis is on one representative step in air-to-helium ratio

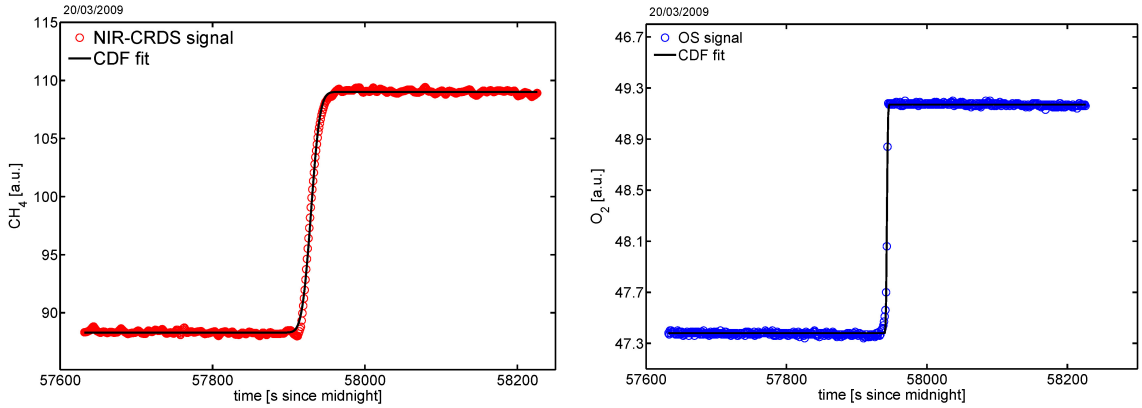

Figure B.1: *The measurements from the NIR-CRDS and the OS during the performance test of the OS (cf. Chapter 5). Left: Measurements from the NIR-CRDS (red circles) and a fit to the data with a CDF (solid black line). Right: Measurements from the OS (blue circles) and a fit to the data with a CDF (solid black line).*

from this experiment (the results from analyses of three steps are in good agreement but not shown here). The responses of the two instruments to this step are shown in Fig. B.1. The response of the NIR-CRDS (red) is less sharp than the response of the OS (blue) which is a consequence of the dispersion of the sample gas in the cavity of the NIR-CRDS.

Assuming the ideal case of zero dispersion the change in air-to-helium ratio can be described by a scaled and shifted version of the Heaviside unit step function as:

$$G(t) = \begin{cases} b & t < 0 \\ a \cdot H(t) + b & t \geq 0 \end{cases} . \tag{B.1}$$

Smoothing of the step function due to dispersion in the system is expressed by the convolution of $G(t)$ with a smoothing function $s(t)$ as

$$g(t) = [G * s](t), \tag{B.2}$$

where $g(t)$ is the measured response to $G(t)$. Differentiating Eq. (B.2) and using Eq. (B.1) for $t \geq 0$ yields

$$\frac{dg}{dt} = \frac{dG}{dt} * s(t) = a \cdot \frac{dH}{dt} * s(t). \tag{B.3}$$

The derivative of the Heaviside step function is the δ_{Dirac} and Eq. (B.3) becomes

$$\frac{dg}{dt} = a \cdot \delta_{\text{Dirac}} * s(t). \tag{B.4}$$

Thus, the response of the system to a δ_{Dirac} can be estimated by the derivative of the response of the instruments to a step function. In Fig. B.2 the responses of the NIR-CRDS and the OS to a δ_{Dirac} is shown as red and blue circles, respectively.

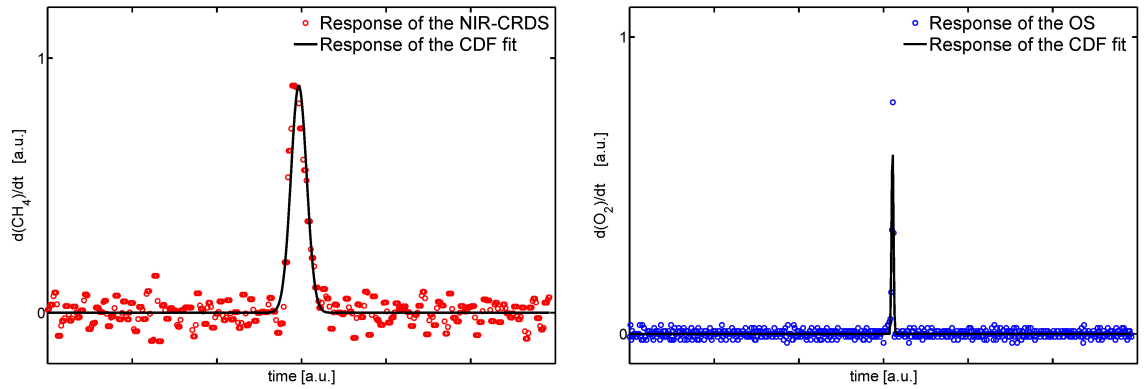

Figure B.2: *The responses of NIR-CRDS (left) and OS (right) to a Dirac delta function. The solid black line shows a CDF fitted to the data series.*

From the convolution theorem it follows:

$$\mathcal{F}\left(\delta_{\text{Dirac}} * s\right) = \mathcal{F}\left(\delta_{\text{Dirac}}\right) \cdot \mathcal{F}\left(s\right). \tag{B.5}$$

where $\mathcal{F}$ denotes the Fourier transform operator. Thus, Eq. (B.4) becomes

$$\mathcal{F}\left(\frac{dg}{dt}\right) = a \cdot \mathcal{F}(\delta_{\text{Dirac}}) \cdot \mathcal{F}(s), \tag{B.6}$$

with $\mathcal{F}(\delta_{\text{Dirac}}) = 1$. Thus, the transfer function is given by the Fourier transform of the derivative of the measured response $g(t)$. The transfer function can be used to obtain estimates of the smoothing effects on input signals with different frequencies. These estimates help to asses the resolution of the system. For the data series of the NIR-CRDS and the OS which are shown in Fig. B.1 the Fourier transforms of the transfer functions are calculated. They are shown in Fig. B.3.

From Fig. B.3 it can be estimated how much a periodic signal of a certain frequency has been damped when it is measured by the OS and the NIR-CRDS, respectively. The amplitude A_0 of a periodic signal of frequency 0.02 Hz, for instance, is damped to $0.5A_0$ when measured by the NIR-CRDS. When the same periodic signal is measured by the upstream installed OS its amplitude is still $0.98A_0$.

In order to compare to noise free data, the two data series are fitted with a scaled version of the cumulative distribution function (hereafter CDF) of a normal distribution as

$$\Phi(t) = \frac{K_1}{2}\left[1 + \text{erf}\left(\frac{t - t_0}{\sigma\sqrt{2}}\right)\right] + K_2, \tag{B.7}$$

where the constants $\text{K}_1, \text{K}_2, \text{t}_0$ and σ are optimized by a least square method. The modelfits to the two data series are shown in Fig. B.1 as black solid lines. Based on these model fits the responses to a step function (Fig. B.2) and the transfer functions (Fig. B.3) can be calculated.

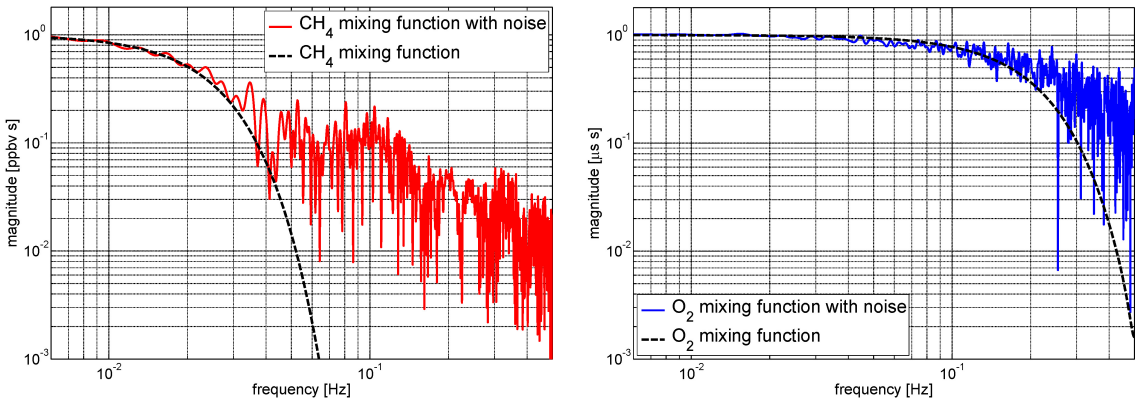

Figure B.3: *Mixing functions f for NIR-CRDS (left, red solid line) and OS (right, blue solid line). The dashed black lines show Mixing functions of the CDF fits to the data series of NIR-CRDS and OS, respectively.*

By comparing the transfer functions which are based on real data series with the ones based on the model fits in Fig. B.3, one can estimate the highest frequency which can still be distinguished from the noise of the data series after smoothing. This frequency is estimated to be 0.03 Hz for the NIR-CRDS and 0.15 Hz for the OS, respectively. This corresponds to a period of measurements of 33 s for the NIR-CRDS and 7 s for the OS, respectively.

Now, the depth resolution of the CRDS system during the 2009 NEEM field season can be estimated (cf. Chapter 6). In the CFA system in the field ice cores are melted at a rate of ca. 35mm/min. The resolution of the CRDS system is set by the NIR-CRDS which is the "weakest link in the chain" in terms of resolution. Therefore, one cannot distinguish any signal from the noise of the measurement which has a wavelength shorter than ca. 19 mm.

The exact depth resolution is most likely a bit lower since the resolution estimation is based on the very simple experimental setup of the performance test of the OS. In the field setup the melt head, the debubbler and the gas extraction unit introduce dispersion and contribute to the smoothing of the signal. However, the cavity is the largest contributor to the smoothing of the signal due to its large volume and the depth resolution of 19 mm is a good estimate.

Appendix C

Error calculation

This appendix describes how the uncertainties of the results from the measurements of the 2009 NEEM field season are calculated (cf. Chapter 6).

The starting points for the calculation of uncertainties are the instrumental uncertainties of the NIR-CRDS and the OS. It was decided to check the manufacturers' specifications for the uncertainties of the instruments which are stated as 0.5 ppbv of CH_4 (1σ) for the NIR-CRDS and 0.005% (for one atmosphere) for the O_2 concentration measurements of the OS. The uncertainty of the measurements of the OS is given in 0.005% at one atmosphere which correponds to 0.051 mbar.

The uncertainties of the instruments are tested with the performance test of the OS (cf. Chapter 5). This experiment was developed to test the performance of the OS in combination with the NIR-CRDS over a wide range of concentrations which makes this experiment ideal for testing the uncertainties of the measurements of the instruments as well. Table C.1 shows the mean values and standard deviations from each concentration step that has been measured during this experiment. The experiment is shown in Fig. 5.4.

The average value of the all standard deviations is 0.1498 ppbv for the NIR-CRDS measurements and 0.0129 μs for the OS, respectively. When comparing these results to the manufacturers' specifications one finds for the NIR-CRDS that the measurements are more precise than the specification of 0.5 ppbv. For further error calculations an instrumental uncertainty of $\sigma_{CH_4} = 0.15$ ppbv is used for the measurements of the NIR-CRDS. For the measurements of the OS it can be confirmed that the relative errors become smaller with decreasing oxygen concentration (inversely proportional to measured lifetime). For further error calculations the average uncertainty of $\sigma_{O_2} = 0.013$ μs is used for the measurements of the OS.

The uncertainty of the final result, the atmospheric concentration of CH_4, is determined with the use of the error propagation equation given by

$$\sigma_x^2 = \sigma_u^2 \left(\frac{\partial x}{\partial u}\right)^2 + \sigma_v^2 \left(\frac{\partial x}{\partial v}\right)^2 + \ldots + 2\sigma_{uv}^2 \left(\frac{\partial x}{\partial u}\right)\left(\frac{\partial x}{\partial v}\right) + \ldots, \tag{C.1}$$

where σ_x is the uncertainty of a function $x = f(u, v, \ldots)$. This function depends on several measured quantities each of them with an individual uncertainty σ_u, σ_v etc. If two

NIR-CRDS		OS		
mean	std	mean	std	relative
20.1398	0.0998	48.2196	0.0111	0.023
37.8924	0.1596	42.8531	0.0137	0.032
45.0506	0.1297	41.0312	0.0092	0.022
52.2093	0.1490	39.5005	0.0165	0.042
59.1529	0.1223	37.9891	0.0138	0.036
68.8324	0.1931	36.2563	0.0180	0.050
92.5556	0.1580	32.5689	0.0091	0.028
96.2775	0.1731	32.1041	0.0183	0.057
122.3499	0.2154	29.1238	0.0144	0.049
144.9909	0.1211	27.0278	0.0137	0.051
171.1236	0.0753	25.0218	0.0153	0.061
185.5850	0.1500	24.1246	0.0119	0.082
196.3410	0.1360	23.4334	0.0149	0.064
228.2762	0.1430	21.7598	0.0128	0.059
420.3711	0.2227	15.6671	0.0075	0.048

Table C.1: *Mean values (mean) and standard deviations (std) from the NIR-CRDS and OS measurements during the performance test of the OS. Mean and std from the NIR-CRDS measurements are given in ppbv. Mean and std from the OS measurements are given in μs. The last column shows the relative uncertainties of the OS given in %.*

quantities are independent the mixed term is equal to zero.

The NIR-CRDS measures CH_4 concentrations and the OS measures the lifetime of fluorescence at the tip of its probe. The first propagating error in the analysis occurs when the CH_4 concentration measurement is converted to partial pressure by

$$p_{CH_4} = p_{\text{cavity}} \cdot [CH_4]_{\text{measured}} \cdot 10^{-9}, \tag{C.2}$$

where p_{cavity} is the cavity pressure and $[CH_4]_{\text{measured}}$ is the concentration of CH_4 in the cavity as measured by the spectrometer. The cavity pressure is recorded with an uncertainty of $\sigma_p = 0.067 mbar$ and with the use of Eq. (C.1) one obtains

$$\begin{aligned}\sigma^2_{p_{CH4}} = & \\ & \sigma^2_{CH_4} \left(p_{cavity} \cdot 10^{-9}\right)^2 + \\ & \sigma^2_p \left([CH_4]_{measured} \cdot 10^{-9}\right)^2 + \\ & 2\sigma_{CH_4}\sigma_p \left(p_{cavity} \cdot 10^{-9}\right)\left([CH_4]_{measured} \cdot 10^{-9}\right),\end{aligned} \tag{C.3}$$

where $\sigma_{p_{CH4}}$ is the uncertainty of the calculated partial pressure of CH_4. The measurements

of cavity pressure and CH_4 concentration are correlated and the mixed term in Eq. (C.1) has to be taken into account.

A second propagating error needs to be determined when the CH_4 concentration of the sample gas is calculated with

$$[CH_4]_{\text{sample}} = \frac{p_{CH_4}}{p_{\text{air}}} \cdot 10^9, \tag{C.4}$$

where p_{air} is the partial pressure of air. The uncertainty of p_{air} has been estimated in Section 4.2.1 to be $\sigma_{p_{\text{air}}} = 4.8$ mbar and with Eq. (C.1) one obtains the uncertainty of the CH_4 concentration of the sample as

$$\begin{aligned}\sigma^2_{[CH_4]_{\text{sample}}} = & \\ & \sigma^2_{p_{CH4}} \left(\frac{10^9}{p_{\text{air}}}\right)^2 + \\ & \sigma^2_{p_{\text{air}}} \left(-\frac{p_{CH_4}}{p^2_{\text{air}}} \cdot 10^9\right)^2 + \\ & 2\sigma_{p_{CH4}} \sigma p_{\text{air}} \left(\frac{10^9}{p_{\text{air}}}\right) \left(-\frac{p_{CH_4}}{p^2_{\text{air}}} \cdot 10^9\right).\end{aligned} \tag{C.5}$$

Finally, the calculations of $[CH_4]_{\text{sample}}$ have to corrected with the CFA calibration which is described in Section 6.2. The CFA calibration curve is linear and described by

$$[CH_4]_{\text{atm}} = a \cdot [CH_4]_{\text{sample}} + b, \tag{C.6}$$

with the atmospheric CH_4 concentration $[CH_4]_{\text{atm}}$ and the constants a and b which stem from the CFA calibration curve (these constants also come with a small uncertainty which is neglected). It follows that

$$\sigma_{[CH4]_{\text{atm}}} = a \cdot \sigma_{[CH4]_{\text{sample}}} + b, \tag{C.7}$$

with the uncertainties $\sigma_{[CH4]_{\text{atm}}}$ of the atmospheric CH_4 concentration.

The uncertainties of the results do not differ significantly between the single CFA runs. Therefore, the uncertainties are only shown for CFA run 2343/2344 in Fig. C.1. The left plot shows the partial pressure of CH_4 calculated with Eq. (C.2) (black) and a 30-seconds running average (red). For reasons of clarity uncertainties are only shown for the running average. They have been calculated with the use of Eq. (C.3). The right plot shows the CH_4 concentration of the sample calculated with Eq. (C.4) (black) and a 30-seconds running average (red). The uncertainties have been calculated with Eq. (C.5).

The contributions of the three uncertainties, i.e. Eqs. (C.3), (C.5) and (C.7), to the total uncertainty are very different. The major contribution stems from Eq. (C.5) which involves measurements of partial pressure of air. These measurements have a large uncertainty of $\sigma_{p_{\text{air}}} = \pm 4.8$ mbar.

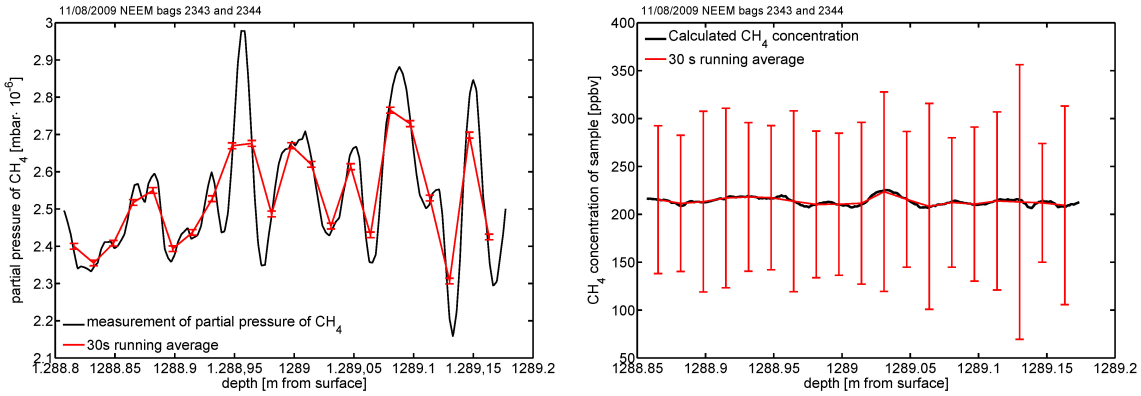

Figure C.1: *The results of CFA run 2343/2344 and the calculated uncertainties. Left: The partial pressure of CH_4 calculated with (C.2) (black) and after a 30-seconds running average has been applied (red). The uncertainties are calculated with the use of (C.3). Right: The unmodified CH_4 concentration (black) and after a 30-seconds running average has been applied (red). The uncertainties are calculated with the use of (C.3) and (C.5).*

The large uncertainty in the measurements of partial pressure of air results in very large uncertainties ($\pm$100 ppbv) in the calculation of the CH_4 concentration of the sample as shown in the right plot of Fig. C.1. However, the uncertainty in the measurements of partial pressure of air is a very pessimistic assumption since it is directly derived from the instrumental uncertainty of the pressure transmitter that was used during the calibration of the OS (cf. Section 4.2.1). As a consequence of numerous measurements during the calibration and the use of a fit through these measurements, the real uncertainty should be smaller. However, an alternative way of how to quantify the uncertainty of the measurement could not be found so far.

Appendix D

MATLAB source code for performance test

```
%-------------------------------------------------------------------------
% Performance test Oxygen Senor and NIR-CRD spectrometer
% Date: 20/03/2009
% Author: Christopher Stowasser
%- - - - - - - - - - - - - - - - - - - - - - - - - - - - - - - - - - - - -
% The methane concentration of dry air (Teknisk luft, Air Liquide Denmark
% A/S, methane oncentration: 2250 ppbv) is calculated from measurements of
% the NIR-CRD spectrometer and the oxygen sensor.
%- - - - - - - - - - - - - - - - - - - - - - - - - - - - - - - - - - - - -
% Abbreviations:
% Methane: CH4
% MA: methane analyzer (NIR-CRDS)
% OS: oxygen sensor
% Filter function for signal smoothing: filter
% Time constant of filter: tau
% Length of filter for OS signal: l_OS
%-------------------------------------------------------------------------

clc
clear all
close all
format long

OSfile = 'TT_03-20-2009_15_12_45_ch1.csv';  % load OS data
DataOSraw = csvread(OSfile,2,1);
OSdata = [DataOSraw(:,1) DataOSraw(:,2)];
% OS data: time [s] lifetime [micro s]

MAfile = fopen('CFADS36-20090320-1512-UserLog.dat');   % load MA data
DataMAraw = textscan(MAfile, '%*s%*s%n%*f%*f%*f%*f%*n%*n%n%*n',...
    'HeaderLines',1);
fclose(MAfile);
[DataMAtime DataMAmethane] = DataMAraw{:};
```

```
MAdata = [DataMAtime DataMAmethane.*1000];
% MA data: time [days since 01/01/2009] CH4 concentration [ppbv]

% Convert the unit of both time measurements to "seconds since midnight"
MAdata(:,1) = (MAdata(:,1)-floor(MAdata(1,1))).*24.*3600;
OSdata(:,1) = OSdata(:,1) + (15*3600)+(12*60)+(47);
% OS file starts at 15:12:47

% Unnecessary data are deleted
OSdata(1:1118,:) = [];
MAdata(2393:length(MAdata),:) = [];
temp = find(OSdata(:,1)>MAdata(length(MAdata),1),1,'first');
OSdata(temp:length(OSdata),:) = [];
temp = find(MAdata(:,1)<OSdata(1,1),1,'last');
MAdata(1:temp,:) =[];

% Every second MA data point is deleted since the MA creates duplicates
MAdata(3:2:length(MAdata),:)=[];

% MA data are interpolated on time scale of OS:
joker_MA = zeros(length(OSdata),1);
for n = 3:length(OSdata)-2
    position = find((MAdata(:,1)>OSdata(n,1)) , 1, 'first');
    weight = (MAdata(position,1)-OSdata(n,1)) / (MAdata(position,1)-...
        MAdata((position-1),1));
    joker_MA(n) = weight*MAdata(position-1,2) + (1-weight)...
        *MAdata(position,2);
end
joker_MA(1:2) = joker_MA(3);
joker_MA(length(OSdata)-2:length(OSdata)) = joker_MA(length(OSdata)-3);
MAdata = [OSdata(:,1) joker_MA];

% Visual matching of steps yields: OS precedes MA by 10 seconds
OSdata(:,1) = OSdata(:,1) + 10;     % Synchronization
cutOS = find(OSdata(:,1)>MAdata(length(MAdata),1),1,'first');
OSdata(cutOS:length(OSdata),:) = [];
cutMA = find(MAdata(:,1)<OSdata(1,1),1,'last');
MAdata(1:cutMA,:) =[];

correlation_original = corr(OSdata(:,2),MAdata(:,2));
% Correlation of the two signals before any smoothing

%-------------------------------------------------------------------------
% A filter function is used to smooth the OS signal. It has two
% parameters which can be tuned: Length l and time constant tau. They are
% optimized in the following loop. As a check for the goodness of each
% smoothed OS signal we use the qualty of a polyinomial fit to the relation
% between smoothed OS signal and NIR-CRDS signal. The norm of the residuals
% reflects the fit quality.
%-------------------------------------------------------------------------
```

```
scan_tau = 400;
scan_l = 40;
fitparam = zeros(4,scan_tau); % 4 parameters of 3rd order polynomial fit
fitnorm = zeros(scan_tau,1); % Norm of the residuals
fit = zeros(length(OSdata)-(500),scan_tau); % The polynomial fit
CH4 = zeros(length(OSdata)-(500),scan_tau); % Calculated CH4 concentration
best_norm = zeros(scan_l,1);
best_tau = zeros(scan_l,1);
for l = 1:scan_l        % Length l of filter
    tau = zeros(scan_tau,1);
    OSdataCONV = zeros(length(OSdata)+l,scan_tau);
% The following loop computes smoothed OS signals with different taus
    for c = 1:scan_tau
        tau(c) = c/10;    % Time cosntant tau of filter
        filter = exp((-1/tau(c))*(0:l))./sum(exp((-1/tau(c))*(0:l)));
        OSdataCONV(:,c) = conv(OSdata(:,2),filter);% Smoothed OS signal
    end
    OSdataCONV(length(OSdataCONV)-(l-1):length(OSdataCONV),:) = [];
    OSdataCONV(1:500,:) = [];
    tempMAdata = MAdata;
    tempMAdata(1:500,:) =[];
% The following loop computes fits, norms of residuals and
    for c = 1:scan_tau
        [temp1 temp2] = polyfit(OSdataCONV(:,c),tempMAdata(:,2),3);
        fitparam(:,c) = temp1;
        fitnorm(c,1) = temp2.normr;
        fit(:,c) = fitparam(1,c).*(OSdataCONV(:,c).^3)+fitparam(2,c).*...
        (OSdataCONV(:,c).^2)+fitparam(3,c).*OSdataCONV(:,c)+fitparam(4,c);
        CH4(:,c) = (tempMAdata(:,2)./fit(:,c)).*2250;
    end
% The best norm of residuals and corresponding time constant:
    [best_norm(l) best_tau(l)] = min(fitnorm);
end
[optimized_norm optimized_length] = min(best_norm);
optimized_tau = best_tau(optimized_length);
% ------------------------------------------------------------------------
% Optimized paramters:  Length filter 33s  Mixing time: 29.8s  Normr: 20.81
% ------------------------------------------------------------------------
```

Appendix E

MATLAB source code for data analysis of CFA run 2342/2343

```
%-------------------------------------------------------------------------
% Data Analysis of CFA run 2342/2343 NEEM
% Date: 11/08/2009
% Author: Christopher Stowasser
%- - - - - - - - - - - - - - - - - - - - - - - - - - - - - - - - - - - - -
% Run 2342/2343 represents a typical CFA run which we choose as an example
% to present the most important steps of data analysis. The first
% two-thirds of the run are interrupted by GC measurements and is
% discarded. The NIR-CRDS nad OS signal of the last third are modified and
% used to calcualte the CH4 concentration of the sample.
%- - - - - - - - - - - - - - - - - - - - - - - - - - - - - - - - - - - - -
% Abbreviations:
% Methane: CH4                                  pCH4: partial pressure CH4
% MA: methane analyzer (NIR-CRDS)               pO2: partial pressure O2
% OS: oxygen sensor                             pAIR: partial pressure air
% Filter function for signal smoothing: filter
% Time constant of filter: tau
% Length of filter for OS signal: l             CONV: convoluted signal
%-------------------------------------------------------------------------
clc
clear all
close all
format long

OSfile = 'TT_03-20-2009_15_12_45_ch1.csv';  % load OS data
DataOSraw = csvread(OSfile,2,1);
OSdata = [DataOSraw(:,1) DataOSraw(:,2)];
% OS data: time [s] lifetime [micro s]

MAfile = fopen('CFADS36-20090320-1512-UserLog.dat');   % load MA data
DataMAraw = texttau(MAfile, '%*s%*s%n%*f%*f%*f%*f%*n%*n%n%*n',...
    'HeaderLines',1);
fclose(MAfile);
```

```
MAdata = [DataMAraw{:,1} DataMAraw{:,2}.*1000];
% MA data: time [days since 01/01/2009] CH4 concentration [ppbv]

fid = fopen('lifetimetopressure.txt');  % load calibration data
CalibrationDataraw = texttau(fid, '%n%n', 'HeaderLines', 0);
fclose(fid);
CalibrationData = [CalibrationDataraw{:,1} CalibrationDataraw{:,2}];
% Calibration data:  [days since 01/01/2009] CH4 concentration [ppbv]

% Convert the unit of both time measurements to "seconds since midnight"
MAdata(:,1) = (MAdata(:,1)-floor(MAdata(1,1))).*24.*3600;
OSdata(:,1) = OSdata(:,1) + (15*3600)+(12*60)+(47);
% OS file starts at 15:12:47

% The CFA run 2342/2343:
MAdata(4746+1:length(MAdata),:) = [];
OSdata(24371+1:length(OSdata),:) = [];
MAdata(1:4360-1,:) = [];
OSdata(1:22418-1,:) = [];

% Every second MA data point is deleted since the MA creates duplicates
MAdata(3:2:length(MAdata),:)=[];

% MA data are interpolated on time scale of OS:
joker_MA = zeros(length(OSdata),1);
for n = 3:length(OSdata)-2
    position = find((MAdata(:,1)>OSdata(n,1)) , 1, 'first');
    weight = (MAdata(position,1)-OSdata(n,1)) / (MAdata(position,1)-...
        MAdata((position-1),1));
    joker_MA(n) = weight*MAdata(position-1,2) + (1-weight)...
        *MAdata(position,2);
end
joker_MA(1:2) = joker_MA(3);
joker_MA(length(OSdata)-2:length(OSdata)) = joker_MA(length(OSdata)-3);
MAdata = [OSdata(:,1) joker_MA];

% Approximate depth scale:
bag = 2342; % bag number, each bag is 0.55 m long
baglength = 1.077;  % bag length [m]
depth = ((bag*.55):((bag*.55+baglength) - ...
    (bag*.55))/(length(MAdata)-1):(bag*.55+baglength))';
MAdata(:,1) = depth; OSdata(:,1) = depth;

% Visual matching of steps yields: OS precedes MA by 12.639 seconds
OSdata(:,1) = OSdata(:,1) + 12.639;     % Preliminary synchronization
cutOS = find(OSdata(:,1)>MAdata(length(MAdata),1),1,'first');
OSdata(cutOS:length(OSdata),:) = [];
cutMA = find(MAdata(:,1)<OSdata(1,1),1,'last');
MAdata(1:cutMA,:) =[];

% The uninterrupted part of the CFA run:
```

```
MAdata(1:1283-1,:) = [];
OSdata(1:1283-1,:) = [];

% The OS calibration converts lifetime to partial pressure of O2:
pO2 = zeros(length(OSdata),1);
for n = 1:length(OSdata)
    [minvalue position] = min(abs(CalibrationData(:,1)-OSdata(n,2)));
    pO2(n) = CalibrationData(position,2);
end
pAIR = (pO2./0.2095); % [mbar]
pCH4 = MAdata(:,2).*1e-009.*((20.*1.3332) + 35.34); % [mbar]
% cavity pressure 20 Torr, pump offset 35.34 mbar
OSdata(:,2) = pAIR;
MAdata(:,2) = pCH4;

%-------------------------------------------------------------------------
% A filter function is used to smooth the OS signal. It has two
% parameters which can be tuned: Length l and time constant tau. They are
% optimized in the following loop. A third loop finds the optimal
% synchronization. The values are optimized by minimizing the standard
% deviation of the result.
%-------------------------------------------------------------------------

tau = 200;  % time constant of filter: loop over 1:tau
lmax = 100;  % length of filter: loop over taumin:taumax
best_std = zeros(lmax,1);
best_tau = zeros(lmax,1);
best_mean = zeros(lmax,1);
best_shift = zeros(lmax,1);
for l =lmin:lmax      % this loop scans over filter length
    timescale = zeros(tau,1);
    OSdataCONV = zeros(length(OSdata)+l,tau);
        for c = 1:tau   % this loop scans over time constants tau
            timescale(c) = c/10;
            filter = exp((-1/timescale(c))*(0:l))...
                /sum(exp((-1/timescale(c))*(0:l)));
            OSdataCONV(:,c) = conv(OSdata(:,2),filter);
        end
    OSdataCONV(length(OSdataCONV(:,c))-(l-1):length(OSdataCONV(:,c)),:)=[];
    OSdataCONV(1:l,:) = [];
    tempMACONV = MAdata;
    tempMACONV(1:l,:) =[];
    tempOSCONV = OSdata(:,1);
    tempOSCONV(1:l) = [];
    shift_std1 = zeros(tau,1);
    shift_std2 = zeros(tau,1);
    shift_shift1 = zeros(tau,1);
    shift_shift2 = zeros(tau,1);
    shift_mean1 = zeros(tau,1);
    shift_mean2 = zeros(tau,1);
        for c = 1:tau       % these two loops synchronize by shifting the
```

```
            shiftmax = 15;  % two signals
            shiftmin = 0;
            shiftCH4mean1 = zeros(shiftmax+1,1);
            shiftCH4std1 = zeros(shiftmax+1,1);
            for shift = shiftmin:shiftmax
                tempOS = OSdataCONV(shift+1:length(OSdataCONV(:,c)),c);
                tempMA = tempMACONV(1:length(tempMACONV)-shift,:);
                tempCH4 = (tempMA(:,2)./tempOS).*1e009;
                shiftCH4mean1(shift+1) = mean(tempCH4);
                shiftCH4std1(shift+1) = std(tempCH4);
            end
            [shift_std1(c) shift_shift1(c)]= min(shiftCH4std1);
            shift_shift1(c) = shift_shift1(c) - 1;
            shift_mean1(c) = shiftCH4mean1(shift_shift1(c)+1);
            shiftmax2 = 15;
            shiftmin2 = 1;
            shiftCH4mean2 = zeros(shiftmax2,1);
            shiftCH4std2 = zeros(shiftmax2,1);
            for shift2 = shiftmin2:shiftmax2
                tempMA = tempMACONV(shift2+1:length(tempMACONV),:);
                tempOS = OSdataCONV(1:length(OSdataCONV(:,c))-(shift2),c);
                tempCH4 = (tempMA(:,2)./tempOS).*1e009;
                shiftCH4mean2(shift2) = mean(tempCH4);
                shiftCH4std2(shift2) = std(tempCH4);
            end
            [shift_std2(c) shift_shift2(c)]= min(shiftCH4std2);
            shift_shift2(c) = shift_shift2(c)*(-1);
            shift_mean2(c) = shiftCH4mean2(shift_shift2(c)*(-1));
        end
    [best_std1 best_tau1] = min(shift_std1);
    [best_std2 best_tau2] = min(shift_std2);
    if best_std1 <= best_std2
        best_std(l) = best_std1;
        best_tau(l) = best_tau1;
        best_mean(l) = shift_mean1(best_tau1);
        best_shift(l) = shift_shift1(best_tau1);
    else
        best_std(l) = best_std2;
        best_tau(l) = best_tau2;
        best_mean(l) = shift_mean2(best_tau2);
        best_shift(l) = shift_shift2(best_tau2);
    end
end
[optimized_std optimized_length] = min(best_std(lmin:lmax));
optimized_length = optimized_length + (lmin-1);
optimized_tau = best_tau(optimized_length);
optimized_mean = best_mean(optimized_length);
optimized_shift = best_shift(optimized_length);
MAdata(1:l,:) = [];
OSdata(1:l,:) = [];
% ------------------------------------------------------------------------
```

```
% Optmized parameters: Length filter = 88s, Tau = 19.1s, Shift = 6s
% Correlation = 0.9584, Standard deviation = 4.1093 ppbv
% ____________________________________________________________________________
```

Bibliography

[1] M. Delmotte, J. Chappellaz, E. Brook, P. Yiou, J.M. Barnola, C. Goujon, D. Raynaud, and V.I. Lipenkov. Atmospheric methane during the last four glacial-interglacial cycles: Rapid changes and their link with Antarctic temperature. *Journal of Geophysical Research*, 109(D12):D12104, 2004.

[2] W.F. Ruddiman. *Earth's Climate: Past and Future*. W. H. Freeman and Company, 2001.

[3] L. Loulergue, A. Schilt, R. Spahni, V. Masson-Delmotte, T. Blunier, B. Lemieux, J.M. Barnola, D. Raynaud, T.F. Stocker, and J. Chappellaz. Orbital and millennial-scale features of atmospheric CH_4 over the past 800,000 years. *Nature*, 453(7193):383–386, 2008.

[4] S. Solomon, D. Qin, M. Manning, M. Marquis, K. Averyt, MMB Tignor, H.L.J. Miller, and Z. Chen. Climate change 2007: the physical science basis; Contribution of Working Group I to the fourth Assessment Report of the Intergovenmental Panel on Climate Change. 2007.

[5] J. Flückiger, T. Blunier, B. Stauffer, J. Chappellaz, R. Spahni, K. Kawamura, J. Schwander, T.F. Stocker, and D. Dahl-Jensen. N_2O and CH_4 variations during the last glacial epoch: Insight into global processes. *Global Biogeochem. Cycles*, 18(1), 2004.

[6] R.P.W. Scott. *Techniques and practice of Chromatography*. CRC Press, 1995.

[7] D. Raynaud, J.Chappellaz, J.M. Barnola, Y.S.Korotkevich, and C.Lorius. Climatic and CH_4 cycle implications of glacial-interglacial CH_4 change in the vostok ice core. *Nature*, 333:655–657, 1988.

[8] J. Chappellaz, T. Blunier, D. Raynaud, J.M. Barnola, J. Schwander, and B. Stauffert. Synchronous changes in atmospheric CH_4 and Greenland climate between 40 and 8 kyr BP. 368:443–445, 1993.

[9] T. Blunier, J. Chappellaz, J. Schwander, J.M. Barnola, T. Desperts, B. Stauffer, and D. Raynaud. Atmospheric methane, record from a Greenland ice core over the last 1000 year. *Geophysical Research Letters*, 20(20), 1993.

[10] J. Chappellaz, T. Blunier, S. Kints, A. Dällenbach, J.M. Barnola, J. Schwander, D. Raynaud, and B. Stauffer. Changes in the atmospheric CH_4 gradient between Greenland and Antarctica during the Holocene. *Journal of Geophysical Research-Atmospheres*, 102(D13), 1997.

[11] R. Spahni, J. Chappellaz, T.F. Stocker, L. Loulergue, G. Hausammann, K. Kawamura, J. Fluckiger, J. Schwander, D. Raynaud, V. Masson-Delmotte, et al. Atmospheric methane and nitrous oxide of the late Pleistocene from Antarctic ice cores. *Science*, 310(5752):1317–1321, 2005.

[12] T. Sowers, E. Brook, D. Etheridge, T. Blunier, A. Fuchs, M. Leuenberger, J. Chappellaz, J.M. Barnola, M. Wahlen, B. Deck, et al. An interlaboratory comparison of techniques for extracting and analyzing trapped gases in ice cores. *Journal of Geophysical Research. C. Oceans*, 102:26, 1997.

[13] D. Lowe, J. White, I. Levin, P. Bergamaschi, M. Wahlen, and J.B. Miller. Isotope measurement techniques for atmsoheric methane. *Stable isotope measurement techniques for atmospheric greenhouse gases*, page 25, 2002.

[14] S. Schüpbach, U. Federer, P.R. Kaufmann, M.A. Hutterli, D. Buiron, T. Blunier, H. Fischer, and T.F. Stocker. A new method for high-resolution methane measurements on polar ice cores using continuous flow analysis. *Environmental science & technology*, 43(14):5371, 2009.

[15] S. L. Buchardt. *Basal melting and Eemian ice along the main ice ridge in northern Greenland*. PhD thesis, University of Copenhagen, 2009.

[16] K.K. Andersen, N. Azuma, J.M. Barnola, M. Bigler, P. Biscaye, N. Caillon, J. Chappellaz, H.B. Clausen, D. Dahl-Jensen, H. Fischer, et al. High-resolution record of Northern Hemisphere climate extending into the last interglacial period. *Nature*, 431(7005):147–151, 2004.

[17] T. Blunier and E.J. Brook. Timing of millennial-scale climate change in Antarctica and Greenland during the last glacial period. *Science*, 291(5501):109–112, 2001.

[18] J.P. Severinghaus, T. Sowers, E.J. Brook, R.B. Alley, and M.L. Bender. Timing of abrupt climate change at the end of the Younger Dryas interval from thermally fractionated gases in polar ice. *Nature*, 391(6663):141–146, 1998.

[19] R.S. Bradley. *Paleoclimatology: Reconstructing Climates of the Quaternary*. Academic Press Limited, 1999.

[20] W.S.B. Paterson. *The physics of glaciers*. Butterworth-Heinemann, 2000.

[21] B.M. Vinther, S.L. Buchardt, H.B. Clausen, D. Dahl-Jensen, S.J. Johnsen, D.A. Fisher, R.M. Koerner, D. Raynaud, V. Lipenkov, K.K. Andersen, et al. Holocene thinning of the Greenland ice sheet. *Nature*, 461(7262):385–388, 2009.

[22] K.K. Andersen, A. Svensson, S.J. Johnsen, S.O. Rasmussen, M. Bigler, R. Röthlisberger, U. Ruth, M.L. Siggaard-Andersen, J. Peder Steffensen, D. Dahl-Jensen, et al. The Greenland Ice Core Chronology 2005, 15–42ka. Part 1: constructing the time scale. *Quaternary Science Reviews*, 25(23-24):3246–3257, 2006.

[23] S.O. Rasmussen, I.K. Seierstad, K.K. Andersen, M. Bigler, D. Dahl-Jensen, and S.J. Johnsen. Synchronization of the NGRIP, GRIP, and GISP2 ice cores across MIS 2 and palaeoclimatic implications. *Quaternary Science Reviews*, 27(1-2):18–28, 2008.

[24] W. Dansgaard, S.J. Johnsen, H.B. Clausen, D. Dahl-Jensen, N.S. Gundestrup, C.U. Hammer, C.S. Hvidberg, J.P. Steffensen, A.E. Sveinbjörnsdottir, J. Jouzel, et al. Evidence for general instability of past climate from a 250-kyr ice-core record. *Nature*, 364(6434):218–220, 1993.

[25] O. Cattani G. Dreyfus S. Falourd G. Hoffmann B. Minster J. Nouet J. M. Barnola J. Chappellaz H. Fischer J. C. Gallet S. Johnsen M. J. Jouzel, V. Masson-Delmotte et al. Orbital and Millennial Antarctic Climate Variability over the Past 800,000 Years. *Science*, 317(5839):793–796, 2007.

[26] J. Schwander, J. Jouzel, C.U. Hammer, J.R. Petit, R. Udisti, and E. Wolff. A tentative chronology for the EPICA Dome Concordia ice core. *Geophysical research letters*, 28(22):4243–4246, 2001.

[27] S.J. Johnsen, W. Dansgaard, and J.W.C. White. The origin of Arctic precipitation under present and glacial conditions. *Tellus B*, 41B(4):452–468, 1989.

[28] W. Dansgaard. Stable isotopes in precipitation. *Tellus*, 16(4):436–468, 1964.

[29] W. Dansgaard, S.J. Johnsen, H.B. Clausen, and N. Gundestrup. Stable isotope glaciology. *Meddelelser om Grønland*, 197(2):1–53, 1973.

[30] B.M. Vinther, H.B. Clausen, S.J. Johnsen, S.O. Rasmussen, K.K. Andersen, S.L. Buchardt, D. Dahl-Jensen, I.K. Seierstad, M.L. Siggaard-Andersen, J.P. Steffensen, et al. A synchronized dating of three Greenland ice cores throughout the Holocene. *Journal of Geophysical Research*, 111:D13102, 2006.

[31] S.J. Johnsen, H.B. Clausen, K.M. Cuffey, G. Hoffmann, J. Schwander, and T. Creyts. Diffusion of stable isotopes in polar firn and ice: the isotope effect in firn diffusion. *Physics of ice core records*, 159:121–140, 2000.

[32] J. Cole-Dai, D. Ferris, A. Lanciki, J. Savarino, M. Baroni, and M.H. Thiemens. Cold Decade (AD 1810–1819) Caused by Tambora (1815) and Another (1809) Stratospheric Volcanic Eruption. *Geophysical Research Letters*, 36:L22703, 2009.

[33] S. Hong, J.P. Candelone, C.C. Patterson, and C.F. Boutron. Greenland ice evidence of hemispheric lead pollution two millennia ago by Greek and Roman civilizations. *Science*, 265(5180):1841, 1994.

[34] A. Svensson, K.K. Andersen, M. Bigler, H.B. Clausen, D. Dahl-Jensen, S.M. Davies, S.J. Johnsen, R. Muscheler, S.O. Rasmussen, R. Röthlisberger, et al. The Greenland Ice Core Chronology 2005, 15–42ka. Part 2: comparison to other records. *Quaternary Science Reviews*, 25(23-24):3258–3267, 2006.

[35] M. Legrand and P. Mayewski. Glaciochemistry of polar ice cores: a review. *Reviews of Geophysics*, 35(3), 1997.

[36] K.C. Taylor, C.U. Hammer, R.B. Alley, H.B. Clausen, D. Dahl-Jensen, A.J. Gow, N.S. Gundestrup, J. Kipfstuhl, J.C. Moore, and E.D. Waddington. Electrical conductivity measurements from the GISP 2 and GRIP Greenland ice cores. *Nature*, 366(6455):549–552, 1993.

[37] E.W. Wolff, W.D. Miners, J.C. Moore, and J.G. Paren. Factors Controlling the Electrical Conductivity of Ice from the Polar Regions–A Summary. *Journal of Physical Chemistry B-Condensed Phase*, 101(32):6090–6094, 1997.

[38] C.U. Hammer, H.B. Clausen, and W. Dansgaard. Greenland ice sheet evidence of post-glacial volcanism and its climatic impact. *Nature*, 288(5788):230–235, 1980.

[39] J. Dai, E. Mosley-Thompson, and L.G. Thompson. Ice core evidence for an explosive tropical volcanic eruption 6 years preceding Tambora. *Journal of Geophysical Research-Atmospheres*, 96(D9), 1991.

[40] C.I. Davidson, J.L. Jaffrezo, B.W. Mosher, J.E. Dibb, R.D. Borys, B.A. Bodhaine, R.A. Rasmussen, C.F. Boutron, U. Gorlach, H. Cachier, et al. Chemical constituents in the air and snow at Dye 3, Greenland. I: Seasonal variations. *Atmospheric environment. Part A, General topics*, 27(17-18):2709–2722, 1993.

[41] A.K. Mortensen, M. Bigler, K. Grönvold, J.P. Steffensen, S.J. Johnsen, et al. Volcanic ash layers from the Last Glacial Termination in the NGRIP ice core. *Journal of Quaternary Science*, 20(3):209–219, 2005.

[42] M.M. Herron and C.C. Langway Jr. Firn densification: an empirical model. *Journal of Glaciology*, 25:373–385, 1980.

[43] L.S. Rothman, D. Jacquemart, A. Barbe, D. Chris Benner, M. Birk, L.R. Brown, M.R. Carleer, C. Chackerian, K. Chance, L.H. Coudert, et al. The HITRAN 2004 molecular spectroscopic database. *Journal of Quantitative Spectroscopy and Radiative Transfer*, 96(2):139–204, 2005.

[44] R.A. Toth. Line strengths (900–3600 cm^{-1}), self-broadened linewidths, and frequency shifts (1800–2360 cm^{-1}) of N_2O. *Applied Optics*, 32:7326–7365, 1993.

[45] H.O. Di Rocco. The exact expression of the Voigt profile function. *J. Quant. Spectrosc. Radiat. Transfer*, 92(2):231–237, 2004.

[46] R.H. Dicke. The effect of collisions upon the Doppler width of spectral lines. *Physical Review*, 89(2):472–473, 1953.

[47] M. Lepère. Line profile study with tunable diode laser spectrometers. *Spectrochimica Acta Part A: Molecular and Biomolecular Spectroscopy*, 60(14):3249–3258, 2004.

[48] Department of Earth Schauble Group and UCLA Space Sciences. Characteristic Vibrations of CH_4 (T_d symmetry). `http://www2.ess.ucla.edu/~schauble/molecular_vibrations.htm` [Online; accessed 16-March-2010].

[49] W. Demtröder. *Experimentalphysik 3: Atome, Moleküle und Festkörper*. Birkhäuser, 2005.

[50] M. Mazurenka, A.J. Orr-Ewing, R. Peverall, and G.A.D. Ritchie. Cavity ring-down and cavity enhanced spectroscopy using diode lasers. *Annu. Rep. Prog. Chem.*, 101:100–142, 2005.

[51] E.R. Crosson. A cavity ring-down analyzer for measuring atmospheric levels of methane, carbon dioxide, and water vapor. *Applied Physics B: Lasers and Optics*, 92(3):403–408, 2008.

[52] R. Paschotta. *Encyclopedia of laser physics and technology*. Vch Pub, 2008.

[53] D. Romanini and K.K. Lehmann. Ring-Down cavity absorption spectroscopy of the very weak HCN overtone bands with six, seven, and eight strechting quanta. *J. Chem. Phys.*, 99:6287–6301, 1993.

[54] R.D. Van Zee, J.T. Hodges, and J.P. Looney. Pulsed, single-mode cavity ringdown spectroscopy. *Appl. Opt*, 38:3951–3960, 1999.

[55] Ocean Optics Inc. *MultiFrequency Phase Fluorometer Installation and Operation Manual*.

[56] Ocean Optics Inc. Fiber Optic Oxygen Sensor Frequently Asked Questions. `http://www.oceanoptics.com/Products/sensorfaqs.asp` [Online; accessed 18-February-2010].

[57] Tandz Grubbs. Fluorescence lifetimes and dynamic quenching. `http://www2.stetson.edu/~wgrubbs/datadriven/quenching/quenchingwtg.html` [Online; accessed 18-February-2010].

[58] Wikipedia. Thermal conductivity detector. `http://en.wikipedia.org/w/index.php?title=Thermal\_conductivity\_detector\&oldid=290916541` [Online; accessed 10-June-2009].

[59] Valco Instruments Co. Inc. Microvolume thermal conductivity detector - Product brochure. `http://www.vici.com/instr/tcd.php` [Online; accessed 18-February-2010].

[60] K.J. Leckrone and J.M. Hayes. Efficiency and temperature dependence of water removal by membrane dryers. *Anal. Chem*, 69(5):911–918, 1997.

Nomenclature

LN_2	Liquid nitrogen
b2k	years before A.D. 2000
CFA	Continuous Flow Analysis
CRD time	cavity ring-down time
CRDS	cavity ring-down spectroscopy
cw	continuous wave
cw-CRDS	continuous-wave cavity ring-down spectroscopy
DAQ	data acquisition system
DAS	Data Acquisition System
DEP	dielectric profiling
DFB laser	Distributed Feedback Laser
ECM	electrical conductivity measurement
EPICA	European Project for Ice Coring in Antarctica
GC	Gas chromatograph
GRIP	Greenland Ice Core Project
HITRAN	high resolution transmission
HWHM	Half Width at Half Maximum
ID	inner diameter
LA	Laser spectrometer
NEA	Noise-Equivalent Absorption

NEEM	North Greenland Eemian Ice Drilling
NIR-CRDS	near-infrared cavity ring-down spectrometer
PD-controlled valve	Proportional-Differential controlled valve
ppbv	parts per billion by volume
ppbv	parts per billion by volume
ppmv	parts per million by volume
PVU	Power Vacuum Unit
PZT	Piezoelectric Transducer
PZT	piezoelectric transducer
SS	stainless steel